UNIVERSITY OF CALIFORNIA, SAN DIEGO

Implications about the Large Scale Properties of the Universe from the Cosmic Microwave Background

A dissertation submitted in partial satisfaction of the
requirements for the degree
Doctor of Philosophy

in

Physics

by

Grigor Aslanyan

Committee in charge:

Professor Aneesh Manohar, Chair
Professor Mark Gross
Professor Elizabeth Jenkins
Professor Justin Roberts
Professor Frank Wuerthwein

2012

The dissertation of Grigor Aslanyan is approved, and it is acceptable in quality and form for publication on microfilm and electronically:

_____

_____

_____

_____

_____

Chair

University of California, San Diego

2012

DEDICATION

To my father Vardan Aslanyan.

EPIGRAPH

"Only two things are infinite: the universe and human stupidity; and I'm not sure about the universe."

—Albert Einstein

TABLE OF CONTENTS

LIST OF FIGURES

LIST OF TABLES

ACKNOWLEDGEMENTS

I would like to thank my advisor Professor Aneesh Manohar for his supervision and support throughout my research. This work would not have been possible without his help.

I would also like to acknowledge Professors Elizabeth Jenkins, Brian Keating, Kim Griest, and Art Wolfe for helpful discussions and for invaluable comments on the draft.

I thank Terrence Martin and Frank Wuerthwein for showing me how to use the DOE OSG cluster.

For constant encouragement and love, I am grateful to my family.

Chapter 2, in full, is a reprint of the material as it appears on JCAP 06 (2012) 003. Aslanyan, Grigor; Manohar, Aneesh V., 2012. The dissertation author was the primary investigator and author of this paper.

Chapter 3, in part is currently being prepared for submission for publication of the material. Aslanyan, Grigor; Manohar, Aneesh, V. The dissertation author was the primary investigator and author of this material.

VITA

2001	Bronze medal in International Mathematics Olympiad (Washington DC, United States)
2001	Honorable mention in International Physics Olympiad (Antalya, Turkey)
2005	B. S. in Physics, Yerevan State University (Armenia)
2005	B. S. in Informatics and Applied Mathematics, Yerevan State University (Armenia)
2004-2005	Junior Engineer, Ponté Solutions Armenia, Physical Design Department (Yerevan, Armenia)
2005-2007	Software Engineer, Ponté Solutions Armenia, Physical Design Department (Yerevan, Armenia)
2004-2007	Research assistant with Yerevan-HERMES group, Yerevan Physics Institute (Armenia)
2007	M. S. in Physics, Yerevan State University (Armenia)
2007	M. S. in Informatics and Applied Mathematics, Yerevan State University (Armenia)
2012	Ph. D. in Physics, University of California, San Diego (United States)

PUBLICATIONS

G. Aslanyan, A. V. Manohar "Constraints on Semiclassical Fluctuations in Primordial Universe from CMB" - in preparation

C. Feng, G. Aslanyan, A. V. Manohar, B. Keating, H. P. Paar, O. Zahn "Measuring Gravitational Lensing of the Cosmic Microwave Background using cross-correlation with large scale structure", arXiv:1207.3326, accepted for publication by Phys. Rev. D

G. Aslanyan, A. V. Manohar "The Topology and Size of the Universe from the Cosmic Microwave Background", JCAP 06 (2012) 003, arXiv:1104.0015

N. Akopov, Z. Akopov, G. Aslanyan, L. Grigoryan "A-dependence of coherent electroproduction of ρ^0 mesons on nuclei in forward direction" arXiv:0707.3530 (2007)

ABSTRACT OF THE DISSERTATION

Implications about the Large Scale Properties of the Universe from the Cosmic Microwave Background

by

Grigor Aslanyan

Doctor of Philosophy in Physics

University of California, San Diego, 2012

Professor Aneesh Manohar, Chair

We analyze the large scale properties of the universe using the seven-year WMAP temperature data. We investigate the global topology of the universe, as well as semiclassical fluctuations of primordial perturbations on large scales.

We study the possibility that the universe is flat, but with one or more space directions compactified. We constrain the size of the compact dimension to be $L/L_0 \geq 1.27, 0.97, 0.57$ at 95% confidence for the case of three, two and one compactified dimension, respectively, where $L_0 = 14.4\,\mathrm{Gpc}$ is the distance to the last scattering surface. We find a statistically significant signal for a compact universe, and the best-fit spacetime is a universe with two compact directions of size $L/L_0 = 1.9$, with the non-compact direction pointing in a direction close to

the velocity of the Local Group.

We consider two possible semiclassical modifications of the primordial power spectrum. For the amplitude of a fluctuation in one Fourier mode we find the 95% bound of $|a_0| \leq 6.45 \times 10^{-4}$. For a semiclassical gaussian fluctuation in space the 95% confidence region for the amplitude is $-5.16 \times 10^{-2} \leq a_0 \leq 5.07 \times 10^{-2}$.

We show that the scenarios we consider are not responsible for the previously suggested possible special direction in space, the so-called "axis of evil".

Chapter 1

Introduction

Questions about the origins and the future of the universe have interested people since ancient times. However, obtaining scientific insights into these questions was practically impossible until very recently because there was no experimental data to support or reject any of the multiple conjectures. Unlike other fields in physics (and other sciences) where experiments can be done (multiple times if needed) to collect data, the only source of data for cosmology is the single universe we live in. In other words, there is only one sample which we cannot even change, all we can do is observe it in its current state. The only way of obtaining information about the past of the universe is to look at the objects very far away from us. The light from these objects takes a finite amount of time to reach us, so we see them as they appeared some time ago.

The simple fact that the universe is expanding was discovered by Edwin Hubble less than hundred years ago. This discovery was very significant since it proved that the universe is not static, it was different in the past and will be different in the future. However, it did not give much information about the history of the universe. The major source of data about the past of the universe was discovered accidentally by Wilson and Penzias in 1964. They discovered electromagnetic radiation in the microwave region coming uniformly from all the directions. It was soon understood that this radiation was a relic of the evolution of the universe in the earliest stages, traveling freely since billions of years ago. The discovery of this radiation, called the **cosmic microwave background (CMB)** radiation,

was a fundamental stepping stone in the development of cosmology, this is when the theory met the experiment, turning the speculations into real science. The importance of the CMB cannot be overestimated, it is literally a snapshot of the universe shortly after its "creation". The CMB has been measured with ever increasing accuracy since then, and new experiments are still being actively designed and implemented.

Firstly, it was noticed that the CMB was very uniform and it followed blackbody radiation spectrum with very high accuracy. This fact was the most important confirmation of the big bang theory and the thermal evolution of the universe. It also confirmed the so-called **cosmological principle** - the fact that the universe (or at least the observable part of it) is homogeneous and isotropic. However, anisotropies of the order of 10^{-5} were predicted and soon confirmed by the measurements of the COBE satellite launched in 1989. This is what made the CMB one of the richest sources of experimental data for cosmology. The WMAP satellite was then launched in 2001 in order to obtain precise measurements of the temperature anisotropies of the CMB. The data obtained from WMAP played an invaluable role in establishing the standard model of cosmology, also called the Λ-CDM model.[1]

The Λ-CDM model is very successful in describing the evolution of the universe from at least the epoch of the synthesis of light elements until now. Observational data has strongly confirmed the predictions of this model. However, there are a few problems that this model fails to explain. The main problems are the so-called **horizon** and **flatness** problems. Points on the **last scattering surface** (the surface from which the currently observed CMB was emitted) that are more than about 1° apart were not (and had never been) in causal contact at the time the CMB was emitted according to the Λ-CDM model. There is no reason then for the CMB to be so uniform across all the sky. This is the horizon problem. There is also no reason why the curvature of the space should be so close to 0, as observed. This is referred to as the flatness problem. The most popular solution to these problems is provided by the concept of **inflation** - a rapid expansion of

[1] Λ refers to the dark energy, and CDM to the cold dark matter. These, according to the model, are currently the dominant constituents of the universe.

the universe very shortly after the "creation".[2] This expansion makes sure that the observable part of the universe was much smaller and in causal contact before inflation started (solution of the horizon problem). Also, the curvature of the space is rapidly driven towards 0 during inflation (solution of the flatness problem). As a bonus, inflationary theories provide a natural way for the generation of the small anisotropies of the CMB. These are seeded by the quantum fluctuations of the field(s) driving inflation. The Λ-CDM model, the problems and their solution by introducing inflation are discussed in more detail in Appendix A.

Although inflation is a very successful addition to the standard cosmological model, it comes with its own problems. We still do not know the correct model of inflation (even the fact that inflation happened has not been confirmed yet), and we know next to nothing about pre-inflationary physics. The state of the universe at the time when inflation started is completely unknown. This information could open a window towards Planck scale physics and bring us closer to understanding how the space-time emerged from the quantum foam. The current experimentally verified fundamental physical theories cannot tell us anything about the global properties of space-time. Therefore, obtaining information about the global structure of the universe from the experimental data is crucial in understanding the fundamental physical laws at Planck scale.

There have been multiple studies in the literature claiming possible deviations from the isotropy of the universe. Some authors suggest that there is a statistically significant signal for a special direction in space, called the "axis of evil". Finite topology of space is one of the ways of breaking the isotropy, and previous studies have shown indications that the experimental data fits the theory with finite topology better than the infinite one. Another possibility is having non-isotropic primordial perturbations generated during inflation. Perhaps inflation started in a non-isotropic state. Detailed studies of these possibilities are in order.

Our goal in this work is to study the properties of the universe on large

[2]The predicted energy density of the universe at the epoch of inflation is close to the GUT scale. Because of this there is no way to check the theory in high energy physics experiments in the laboratory.

scales, and to use the experimental data to put constraints on some of these properties. We study both of the possible scenarios of isotropy breaking mentioned above, how their effects are imprinted on the CMB anisotropies, and how well the observational data fits these theoretical scenarios. We use the most recent seven year temperature data from WMAP for our analysis.

This work is organized as follows. In chapter 2 we consider three finite flat topologies of the universe and their effect on the CMB. We put bounds on the sizes of these topologies using the experimental data. In chapter 3 we analyze two possible modifications of the primordial power spectrum. Again, we obtain limits on these modifications from the experimental data. We summarize our results in chapter 4.

Chapter 2

The Topology and Size of the Universe

2.1 Introduction

General relativity is a local theory and does not predict or constrain the global properties of the spacetime manifold describing our universe, which have to be constrained through observations. Various models for the topology of the universe (for the classification of different possible topologies see, e.g. [2]) have been extensively studied recently and compared to the experimental data. The two most important ones are the Poincaré dodecahedral space and the 3-torus $\mathbb{T}^3$; these models are in best agreement with the experimental data. The Poincaré dodecahedral space arises by slicing the 3-sphere S^3 and thus has positive curvature, while the 3-torus is obtained by slicing infinite Euclidean space $\mathbb{R}^3$ and therefore is flat. Theoretical arguments about quantum creation of the universe favor the flat case. Based on the Wheeler-DeWitt equation, Linde has argued [3] that compact flat universes are much easier to create than other models, and can naturally provide initial conditions for the onset of inflation. Furthermore, Roukema constructed a measure on the set of compact manifolds and showed that non-flat models almost never occur while flat models occur almost certainly [4] (see also [5] for a discussion of the Poincaré dodecahedral space versus the 3-torus). In this

chapter we study the case of a flat universe with non-trivial global topology, i.e. with one or more directions compactified. Details on the Poincaré dodecahedral space and experimental data analysis are given in, e.g. [6, 7, 8, 9].

We analyze three different flat topologies, $\mathscr{M}_0 = \mathbb{T}^3$, $\mathscr{M}_1 = \mathbb{T}^2 \times \mathbb{R}^1$, and $\mathscr{M}_2 = S^1 \times \mathbb{R}^2$, where the subscript denotes the number of non-compact directions. We will generically refer to all three cases as a torus. Usual flat space is $\mathscr{M}_\infty = \mathbb{R}^3$. Note that $\mathscr{M}_{0,1,2}$ are all flat, and with vanishing curvature. Locally, they are indistinguishable from infinite flat space $\mathbb{R}^3$. Globally, of course, there are differences, since signals can propagate around the universe and come back to the starting point. We study the case where the compact directions are of cosmological size, i.e. of order several Gpc.

The 3-torus $\mathbb{T}^3$ can be obtained by identifying the opposite edges of a parallelepiped. We only consider the simplest case of a rectangular parallelepiped with equal side lengths L. This has the highest number of symmetries which helps reduce the computational time. Moreover, it has been argued in [10] that only in well-proportioned spaces is the quadrupole of the CMB temperature-temperature correlation function suppressed compared to the infinite universe. The surprisingly low observed quadrupole is one of the motivations to invoke a compact topology. For our case of the 3-torus, well-proportioned means that all three sides should be approximately equal. The topologies of the spaces $\mathbb{T}^2 \times \mathbb{R}^1$ and $S^1 \times \mathbb{R}^2$ are obtained by compactifying only 2 or 1 dimension respectively. Again, following the argument of [10] and for the sake of simplicity, we consider only the case where the compactified dimensions of $\mathbb{T}^2 \times \mathbb{R}^1$ have the same size. The size of the compact directions will be denoted by L. As $L \to \infty$ all three manifolds reduce to infinite flat space $\mathbb{R}^3$.

Different approaches have been proposed for extracting information about the topology of the universe from the experimental data, the two most important ones being the circles-in-the-sky test and the analysis of the CMB power spectrum. The basic idea of the circles-in-the sky test is that if the global structure of the space is smaller than the distance to the LSS (last scattering surface), then the LSS will self-intersect in circles, producing correlations between circles with different

centers. The detection of such circles can reveal the global properties of space (for detailed description of the method see, e.g. [11, 12, 13]). The main disadvantage of the method is that it cannot be used if the size of the universe is bigger than the observable part of it (the distance to LSS). The one-year WMAP data has been analyzed with this method for signatures of non-trivial spatial topology [14], ruling out the possibility of compact spaces with a length-scale smaller than 24 Gpc. This limit has been extended by about 10% by the authors of [15] who have also ruled out the possibility of Poincaré dodecahedral space. The authors of [16] have analyzed the most recent seven-year WMAP data with this method, putting a lower bound of about 27.9 Gpc on the size of the fundamental domain for a flat universe.

The low-l (i.e. large scale) portion of CMB correlations is sensitive to the topology of space, which gives rise to another method for detecting the topology. The torus preserves the homogeneity of infinite space but breaks rotational invariance. This implies that the power spectrum of CMB temperature-temperature correlations does not contain all the possible information since the off-diagonal elements of the covariance matrix in the spherical harmonics expansion are non-zero in general, while the diagonal elements with equal l and different m values are not all equal to each other (see section 2.3 for more details). Moreover, in [17] it has been argued that the off-diagonal elements contain more information than the diagonal ones if the side length of the torus is less than twice the distance to the last scattering surface. Therefore, to gain all the possible information from the correlations of CMB anisotropies, one has to consider the full covariance matrix rather than just the power spectrum.

The CMB correlation functions have been previously used to analyze COBE [18, 19], one-year WMAP [17, 20] and three-year WMAP [21] data. The lower bound on the side length L of $\mathbb{T}^3$ obtained from COBE data [18] is $L > 4.32h^{-1}$ Gpc at 95% confidence, and $L > 5.88h^{-1}$ Gpc at 68% confidence. For $\mathbb{T}^2 \times \mathbb{R}^1$ and $S^1 \times \mathbb{R}^2$ the lower bound obtained from COBE [19] is $L > 3.0h^{-1}$ Gpc at 95% confidence. The authors of [17] have obtained higher bounds for $\mathbb{T}^3$; $L > 1.2\,L_0$ at 95% confidence and $L > 2.1\,L_0$ at 68% confidence.[1] They have also found that the maximum

[1]We will give lengths in terms of $L_0 = 14.4$ Gpc, the distance to the last scattering surface. The Hubble length is $H_0^{-1} = 2.998/h_0 = 4.266\,(0.703/h_0)$ Gpc.

likelihood occurs for $L = 2.1\,L_0$ (29 Gpc). Several models of tori with different side lengths have been considered in [20] with the conclusions $L > 19.3\,\mathrm{Gpc}$ for $\mathbb{T}^3$ and $L > 14.4\,\mathrm{Gpc}$ for $S^1 \times \mathbb{R}^2$. The main result of [21] is that the 3-torus with volume $\approx 5 \times 10^3\,\mathrm{Gpc}^3$ (which corresponds to side length of 17 Gpc) is well-compatible with the WMAP three-year data. The WMAP seven-year data has been analyzed for detecting signatures of the so-called half-turn space [22] (the only difference of the half-turn space from the 3-torus is that one of the edges is turned by 180° before identifying with the opposite edge) where the case of the 3-torus is also considered. Out of these works, only in [17] and [20] has the full covariance matrix been analyzed. For some earlier results on these topologies see also [23, 24, 25] and references therein.

We analyze the most recent seven-year WMAP data for signatures of the three topologies of flat space mentioned above using the full covariance matrix of temperature-temperature fluctuations. By using the symmetry groups of the spaces we construct efficient algorithms for the theoretical computation of the covariance matrix and the likelihood function using that matrix. These algorithms can be used again as soon as the high precision data from the Planck satellite [26] are released. The computation of the covariance matrix is done using a modified version of the CAMB program [27], as discussed in Sec. 2.3, and that of χ^2 and the likelihood using the available WMAP code [28, 29, 30]. We have used only the TT correlations in our analysis. Including TE, EE, and BB correlations is straightforward, but would quadruple the computer time needed, without much improvement in the results since these other correlations have much larger errors.

There have been speculations in the literature about the detection of a special direction in the CMB map in which the first few multipoles of temperature-temperature correlations seem to be aligned [31, 32, 33]. This is referred to as the "axis of evil" and is given by $b = 60°$, $l = -100°$ in galactic coordinates. The topologies that we consider are not rotationally invariant, in particular $\mathbb{T}^2 \times \mathbb{R}^1$, and $S^1 \times \mathbb{R}^2$ have one special direction (the infinite one in $\mathbb{T}^2 \times \mathbb{R}^1$, and the finite one in $S^1 \times \mathbb{R}^2$), so we analyze the case where this special direction coincides with the axis of evil, to see if the axis of evil can be explained by one of these topologies.

The authors of [34] have analyzed the topology $S^1 \times \mathbb{R}^2$ with the conclusion that it is not the explanation for the multipole alignment.

The chapter is organized as follows. In section 2.2 we present a slight generalization of Linde's argument for the quantum creation of compact universes. We describe the calculation of the covariance matrix and the likelihood in sections 2.3 and 2.4 respectively. We present our numerical results in section 2.5, and discuss the goodness of fit, and maximum likelihood confidence intervals. We have done several checks of our analysis, which are given in section 2.6. The possibility that our results are generated by a random fluctuation are analyzed in section 2.6.1, where we discuss Monte-Carlo skies. The possibility of spurious effects due to a small residual CMB dipole in the data is investigated in section 2.6.2. We summarize in section 2.7. Unless otherwise stated, everywhere in this chapter the side length of the torus is given in units of the distance to the last scattering surface L_0.

2.2 Quantum Creation of Compact Universes

Consider the standard Einstein-Hilbert action of gravity minimally coupled to matter. Here we will be only interested in "quantizing" gravity, so for the matter portion we will just consider energy density V without worrying about where it comes from. Then the action takes the form ($\hbar = c = 1$, $M_{pl} \equiv (8\pi G)^{-1/2} = 1$)

$$S = \frac{1}{2} \int \mathrm{d}^4x \sqrt{-g} \, (R - 2V) \ . \tag{2.1}$$

Following the standard procedure to derive the Wheeler-DeWitt equation we use the ADM form of the spacetime metric [35]

$$\mathrm{d}s^2 = -N^2 \mathrm{d}t^2 + h_{ij}(\mathrm{d}x^i + N^i \mathrm{d}t)(\mathrm{d}x^j + N^j \mathrm{d}t) \, . \tag{2.2}$$

The action can be rewritten in the form

$$S = \int \mathrm{d}^4x \ \mathscr{L} \, , \tag{2.3}$$

with

$$\mathscr{L} = \frac{\sqrt{h}N}{2} \left({}^3R + \frac{1}{N^2}(E_{ij}E^{ij} - E^2) - 2NV \right) \tag{2.4}$$

where ${}^3R$ is the 3-curvature of spatial slices,

$$\begin{aligned} E_{ij} &= \frac{1}{2}(\dot{h}_{ij} - \nabla_i N_j - \nabla_j N_i)\,, \\ E &= E^i_i\,. \end{aligned} \tag{2.5}$$

There are numerous possibilities for the spacetime manifold and it may be described by infinitely many parameters, so to be able to proceed we consider manifolds with finite homogeneous spatial slices which can be characterized by one length scale $a(t)$. In other words, we assume that locally the manifold is characterized by a Friedmann-Robertson-Walker metric while globally it can have any finite topology that is compatible with the metric. So by a suitable choice of coordinates we get in this case

$$N = 1, \quad N_i = 0\,, \tag{2.6}$$

$$h_{ij} = a^2(t) k_{ij}\,, \tag{2.7}$$

where the tensor k_{ij} is constant (it only depends on the choice of the manifold but does not depend on any of the coordinates). Then

$$E_{ij}E^{ij} - E^2 = -6\left(\frac{\dot{a}}{a}\right)^2\,. \tag{2.8}$$

Since we assumed a homogeneous spatial submanifold characterized by single length scale a, by dimensional analysis the volume must be proportional to a^3 and the curvature to a^{-2}. Namely,

$$\int \mathrm{d}^3x\, \sqrt{h} = \alpha a^3\,, \tag{2.9}$$

$${}^3R = \frac{\beta}{a^2}\,, \tag{2.10}$$

where α and β are dimensionless constants that depend only on the choice of the manifold. The Lagrangian then takes the form

$$L = \frac{\alpha}{2}\left(a\beta - 6a\dot{a}^2 - 2a^3 V\right)\,. \tag{2.11}$$

Now we treat a as the dynamical variable describing the geometry. The canonical momentum is then

$$p_a = \frac{\partial L}{\partial \dot{a}} = -6\alpha a\dot{a}\,, \tag{2.12}$$

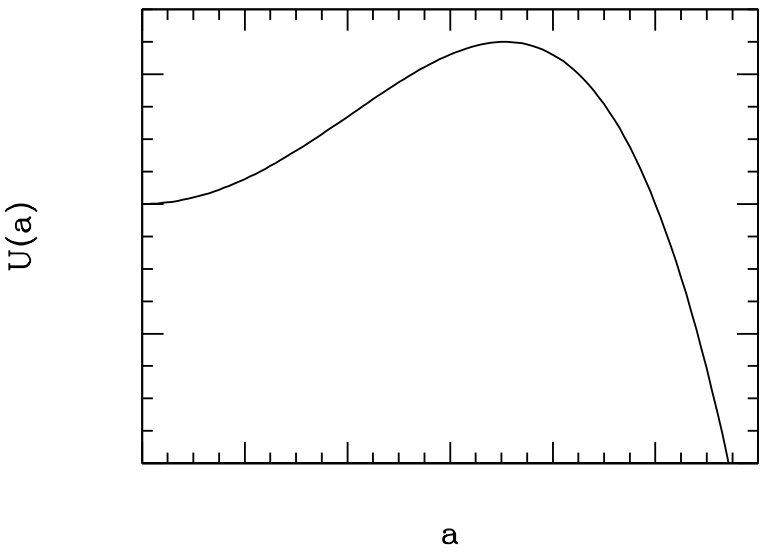

Figure 2.1: Plot of the potential $U(a)$ for a positively curved space ($\beta > 0$). The axes are in arbitrary units.

and the Hamiltonian becomes

$$H = p_a \dot{a} - L = \frac{1}{12\alpha a}\left(-p_a^2 - 6\alpha^2\beta a^2 + 12\alpha^2 a^4 V\right) . \tag{2.13}$$

Finally, we canonically quantize, replacing p_a by the operator $-i(\mathrm{d}/\mathrm{d}a)$ to get for the Hamiltonian

$$H = \frac{1}{12\alpha a}\left(\frac{d^2}{da^2} - 6\alpha^2\beta a^2 + 12\alpha^2 a^4 V\right) . \tag{2.14}$$

Consider now the quantum creation of the universe with zero energy. Then the wavefunction of the universe $\Psi(a)$ satisfies the analog of the Schrödinger equation with Hamiltonian Eq. (2.14), which is called the Wheeler-DeWitt equation. In this case it takes the form

$$\left(\frac{d^2}{da^2} - 6\alpha^2\beta a^2 + 12\alpha^2 a^4 V\right)\Psi(a) = 0\,. \tag{2.15}$$

The effective potential energy is

$$U(a) = 6\alpha^2\beta a^2 - 12\alpha^2 a^4 V\,, \tag{2.16}$$

and is shown in Fig. 2.1 which decreases to $-\infty$ for large a since the second term dominates. However, for small a the first term dominates, so for $\beta > 0$ there is a potential barrier from $a = 0$ to $\sqrt{\beta/2V}$, i.e. the universe has to first undergo tunneling before the expansion can start. This is the reason why the probability of quantum creation of positively curved spaces, which have $\beta > 0$, is thought to be highly suppressed compared to flat and negatively curved spaces. The action for tunneling through the barrier is $S = a_0^3\sqrt{V}/3$, where $a_0 = \sqrt{\beta/(2V)}$ is the size of the created universe. The tunneling probability is $\propto \exp(-S)$, and is greater for smaller universes; $S \to 0, a_0 \to 0$ as $V \to \infty$. For a flat universe, $\beta = 0$, and the barrier vanishes.

2.3 Covariance Matrix Calculation

Now we turn to the calculation of correlations between CMB temperature anisotropies in the flat topologies $\mathbb{T}^3$, $\mathbb{T}^2 \times \mathbb{R}^1$, and $S^1 \times \mathbb{R}^2$. Locally they all look exactly like the infinite flat $\mathbb{R}^3$ so Einstein's equations and therefore the Friedmann equations are unchanged from the infinite case. The calculation for the infinite case is described in standard textbooks (for a detailed derivation see [36]), so let us briefly summarize that calculation and then focus on the differences between the infinite and finite universes. Essentially, one has to take the Einstein's equations that describe the interactions between gravity and all of matter and Boltzmann's equations for interactions between various types of matter (most importantly, electrons and photons) and solve for the distribution of photons today given initial conditions set by inflation. Since the temperature anisotropies in the CMB are about five orders of magnitude smaller than the background, the calculation is done using perturbation theory around the homogeneous background and keeping only first order terms. Then all of the differential equations become linear and can be treated easily in Fourier space. This is where there is a key difference: in an infinite universe the spectrum of the Fourier modes $\mathbf{k}$ is continuous, while for compactified dimensions the spectrum becomes discrete. For a torus with side

lengths L_1, L_2, and L_3 we have $\mathbf{k} = (k_1, k_2, k_3)$,

$$k_1 = \frac{2\pi}{L_1} n_1, \quad k_2 = \frac{2\pi}{L_2} n_2, \quad k_3 = \frac{2\pi}{L_3} n_3 \,, \tag{2.17}$$

where n_1, n_2, n_3 are integers (the torus is essentially a box with periodic boundary conditions). So all of the equations in Fourier space remain unchanged, all we have to worry about is integrations over $\mathbf{k}$ which have to be replaced by sums

$$\int \frac{\mathrm{d}^3 k}{(2\pi)^3} \to \frac{1}{L_1 L_2 L_3} \sum_{\mathbf{k}} , \tag{2.18}$$

over the discrete $\mathbf{k}$ values in Eq. (2.17). The set of points Eq. (2.17) will be referred to as the $\mathbf{k}$ grid.

The three cases studied here can be characterized by different values for L_i. The three-torus $\mathbb{T}^3$ has $L_1 = L_2 = L_3 = L$, $\mathbb{T}^2 \times \mathbb{R}^1$ has $L_1 = L_2 = L$, $L_3 = \infty$, and finally $S^1 \times \mathbb{R}^2$ has $L_1 = L_2 = \infty$, $L_3 = L$. All three cases can be treated in a unified manner by using the integral notation, with the understanding that the integral is to be replaced by a summation if the corresponding L_i is finite.

The first set of summations over $\mathbf{k}$ arises when constructing collision terms in Boltzmann's equations. However, we will not worry about these integrals for the following reason. The Boltzmann's equations are important only before the decoupling epoch, which corresponds to a redshift of about $z \sim 1100$. The co-moving horizon at that time was about 50 times smaller than currently, and the current bounds on the size of the torus are of the order of the size of horizon, so at the epoch of decoupling, the size of the torus was at least about 50 times bigger than the causally connected part. As we will see later in section 2.5, the sums rapidly converge to the corresponding integrals when the topology scale is around 3 times the radius of horizon, which implies that the effects of finiteness can be safely ignored for the epoch of decoupling (and before), and $\mathbf{k}$ can be treated as a continuous variable. All the equations are solved in Fourier space, exactly as for the infinite case.

There is a summation over $\mathbf{k}$ when the final answer for the temperature fluctuations has to be converted from Fourier space back to real space. So let us pick up from that point in the calculation. The temperature anisotropies $\Theta(\hat{\mathbf{n}}, \mathbf{x})$

in direction $\hat{\mathbf{n}}$ at a given point $\mathbf{x}$ (chosen to be our location $\mathbf{x}_0$) are decomposed into spherical harmonics

$$\Theta(\hat{\mathbf{n}}, \mathbf{x}) = \sum_{lm} a_{lm}(\mathbf{x}) Y_{lm}(\hat{\mathbf{n}}) \,, \tag{2.19}$$

where the position space a_{lm} coefficients are given in terms of the Fourier space temperature fluctuations $\Theta(\hat{\mathbf{n}}, \mathbf{k})$ by

$$a_{lm}(\mathbf{x}) = \int \frac{\mathrm{d}^3 k}{(2\pi)^3} e^{i\mathbf{k}\cdot\mathbf{x}} \int \mathrm{d}\Omega \; Y^*_{lm}(\hat{\mathbf{n}}) \Theta(\hat{\mathbf{n}}, \mathbf{k}) \,. \tag{2.20}$$

The observed CMB fluctuations are given by the correlations between the different a_{lm}'s,

$$M_{lml'm'} \equiv \langle a_{lm}(\mathbf{x}_0) a^*_{l'm'}(\mathbf{x}_0) \rangle \;. \tag{2.21}$$

The correlations between temperature anisotropies in k-space are related to the initial power spectrum of gauge invariant curvature perturbations ζ on uniform density hypersurfaces

$$\langle \Theta(\mathbf{k}, \hat{\mathbf{n}}) \Theta^*(\mathbf{k}', \hat{\mathbf{n}}') \rangle \;\; = \;\; (2\pi)^3 \delta^3(\mathbf{k} - \mathbf{k}') P(k) \frac{\Theta(k, \mathbf{k}\cdot\hat{\mathbf{n}})}{\zeta(k)} \frac{\Theta^*(k, \mathbf{k}\cdot\hat{\mathbf{n}}')}{\zeta^*(k)} \,, \tag{2.22}$$

where the curvature perturbations power spectrum is defined by [36]

$$\langle \zeta(\mathbf{k}) \zeta^*(\mathbf{k}') \rangle \equiv (2\pi)^3 \delta^3(\mathbf{k} - \mathbf{k}') P(k) \,. \tag{2.23}$$

The ratios Θ/ζ on the right hand side of Eq. (2.22) do not depend on the initial conditions since the equations are linear. All of the information about initial conditions is now absorbed into $P(k)$. From Eq. (2.20), (2.21), and (2.22) we get

$$M_{lml'm'} = \int \frac{\mathrm{d}^3 k}{(2\pi)^3} P(k) \int \mathrm{d}\Omega \; Y^*_{lm}(\hat{\mathbf{n}}) \frac{\Theta(k, \mathbf{k}\cdot\hat{\mathbf{n}})}{\zeta(k)} \int \mathrm{d}\Omega' \; Y_{l'm'}(\hat{\mathbf{n}}') \frac{\Theta^*(k, \mathbf{k}\cdot\hat{n}')}{\zeta^*(k)} \,. \tag{2.24}$$

Expanding $\Theta(k, \mathbf{k}\cdot\hat{\mathbf{n}})$ into Legendre polynomials

$$\Theta(k, \mathbf{k}\cdot\hat{\mathbf{n}}) = \sum_l (-i)^l (2l+1) P_l(\hat{k}\cdot\hat{\mathbf{n}}) \Theta_l(k) \,, \tag{2.25}$$

and using the identity

$$\int \mathrm{d}\Omega \; P_{l'}(\hat{k}\cdot\hat{\mathbf{n}}) Y_{lm}(\hat{\mathbf{n}}) = \frac{4\pi}{2l+1} \delta_{ll'} Y_{lm}(\hat{k}) \,, \tag{2.26}$$

we finally get

$$M_{lml'm'} = (4\pi)^2(-i)^l i^{l'} \int \frac{\mathrm{d}^3k}{(2\pi)^3} P(k) \frac{\Theta_l(k)}{\zeta(k)} \frac{\Theta^*_{l'}(k)}{\zeta^*(k)} Y^*_{lm}(\hat{\mathbf{k}}) Y_{l'm'}(\hat{\mathbf{k}}) \,. \tag{2.27}$$

The standard result for an infinite universe is a special case of the above analysis. In the infinite case, the angular part of the integral over $\mathbf{k}$ in Eq. (2.27) can be done analytically giving

$$M_{lml'm'} = \delta_{ll'}\delta_{mm'} C_l \,, \tag{2.28}$$

with

$$C_l = \frac{2}{\pi} \int \mathrm{d}k \; k^2 \, P(k) \left| \frac{\Theta_l(k)}{\zeta(k)} \right|^2 \,. \tag{2.29}$$

The derivation remains the same in the finite case except that the $\mathbf{k}$ integral must be replaced by the sum Eq. (2.18), so instead of Eq. (2.27) we get

$$M_{lml'm'} = (4\pi)^2(-i)^l i^{l'} \frac{1}{L_1 L_2 L_3} \sum_{\mathbf{k}} P(k) \frac{\Theta_l(k)}{\zeta(k)} \frac{\Theta^*_{l'}(k)}{\zeta^*(k)} Y^*_{lm}(\hat{\mathbf{k}}) Y_{l'm'}(\hat{\mathbf{k}}) \tag{2.30}$$

Now we have to compute a three-dimensional sum Eq. (2.30) instead of a one-dimensional integral Eq. (2.29) which requires much more computational time. Also, we have to calculate all matrix elements with different l, m, l', m' whereas in the infinite case all $l \neq l'$ or $m \neq m'$ (non-diagonal) elements vanish, while the diagonal ones do not depend on m. The reason for this is clear. In the infinite case, the problem has full rotational invariance, so that angular momentum is conserved. In the cases we consider, rotational invariance is broken. Even though rotational invariance is broken, there is still a large residual discrete symmetry group which can be used to simplify the problem, and reduce the computational time. We will refer to this residual symmetry group as G. For the $\mathbb{T}^2 \times \mathbb{R}^1$ and $S^1 \times \mathbb{R}^2$ cases, G is the symmetry group of a rectangular parallelepiped with two sides equal, the tetragonal group D_{4h} with 16 elements, whereas for $\mathbb{T}^3$, G is the symmetry group of the cube, the octahedral group O_h with 24 elements.

The angular part in the sum in Eq. (2.30) can be separated (this has been suggested earlier in [17])

$$M_{lml'm'} \;=\; \frac{(4\pi)^2(-i)^l i^{l'}}{L_1 L_2 L_3} \sum_k P(k) \frac{\Theta_l(k)}{\zeta(k)} \frac{\Theta^*_{l'}(k)}{\zeta^*(k)} \sum_{|\mathbf{k}|=k} Y^*_{lm}(\hat{\mathbf{k}}) Y_{l'm'}(\hat{\mathbf{k}}) \,, \tag{2.31}$$

where the first sum is over all the allowed spheres in the $\mathbf{k}$ grid while the angular sum is over a fixed sphere and depends only on the choice of that sphere.

We can simplify the computation using the discrete symmetry group G of the manifolds $\mathscr{M}_{0,1,2}$. Consider a fixed sphere of radius k. If the point (θ, ϕ) of the sphere is on the grid, then so are $(\theta, \phi + \pi/2)$, $(\theta, \phi + \pi)$, and $(\theta, \phi + 3\pi/2)$. The angular sum over these four points is proportional to

$$e^{i(m'-m)\phi}\left(1 + e^{i(m'-m)\frac{\pi}{2}} + e^{i(m'-m)\pi} + e^{i(m'-m)\frac{3\pi}{2}}\right) ,$$

which is 0 unless $m' - m$ is divisible by 4, in which case it becomes $4e^{i(m'-m)\phi}$. Consider the points (θ, ϕ) and $(-\theta, \phi)$, which both lie on the sphere. Since

$$Y_{lm}(-\theta, \phi) = (-1)^{l-m} Y_{lm}(\theta, \phi) ,$$

the sum over those two points is 0 unless $l + l' - m - m'$ is even, but $m + m'$ is even if $m' - m$ is divisible by 4, so the extra condition we get is that $l' - l$ has to be even (this also follows from parity). The eight points $(\pm\theta, \phi + n\pi/2)$, $n = 0, 1, 2, 3$ lie in the eight different octants, so the point (θ, ϕ) can be chosen to lie in the first octant. To summarize, the angular sum is nonzero only if $l' - l$ is even and $m' - m$ is divisible by 4, in which case it is equal to 8 times the sum over one octant. Extra care is needed for points on the boundary of the octant to avoid double counting.

Consider the points (θ, ϕ) and $(\theta, \pi/2 - \phi)$ corresponding to swapping n_1 with n_2. Taking into account that $m' - m$ is divisible by 4, we get

$$e^{i(m'-m)\phi} + e^{i(m'-m)(\frac{\pi}{2}-\phi)} = 2\cos\left((m' - m)\,\phi\right) ,$$

which implies that the angular sums are real. Furthermore, $(-i)^l i^{l'}$ is also real for even $l' - l$ and $P(k)$ and $\Theta_l(k)/\zeta(k)$ are real, so the covariance matrix elements $M_{lml'm'}$ are all real implying $M_{lml'm'} = M_{l'm'lm}$. Also, since $Y_{l,-m}(\theta, \phi) = (-1)^m Y^*_{lm}(\theta, \phi)$ and $m' - m$ is divisible by 4, we get $M_{lml'm'} = M_{l,-m,l',-m'}$.

$\mathbb{T}^3$ has more symmetries which can be used to further speed up the calculation for this case. For example, the sums in Eq. (2.31) over the spherical harmonics are the same for all L. Changing L is a rescalling of the allowed momenta by $1/L$. Thus the angular sum for $|\mathbf{k}| = k$ for a $\mathbb{T}^3$ of size L is the same as the angular sum

for $|\mathbf{k}| = \lambda k$ for $\mathbb{T}^3$ of size L/λ. Thus the angular sums can be computed once, and then used for all values of L.

Since the calculation of $\Theta_l(k)/\zeta(k)$ is identical to the case of infinite flat universe, we use the well-known CAMB software [27] (based on CMBFAST [37]) for that part of the calculation. Our code is a simple modification of CAMB, replacing the intergral over $\mathbf{k}$ by a discrete sum. It takes the sides of the torus as extra input parameters and outputs not only C_l but also the complete matrix $M_{lml'm'}$. For large values of l, the discrete sums over $\mathbf{k}$ approach the continuum result, so we only use Eq. (2.31) for $l \leq 30$, and use the continuum result for $l > 30$. The difference between the discrete and continuum values for $M_{lml'm'}$ is less than 0.5% for $l = 30$. As an example, in Fig. 2.2, we have plotted the ratio of the power spectrum C_l for $\mathscr{M}_0$, $\mathscr{M}_1$, and $\mathscr{M}_2$ to that for infinite space $\mathbb{R}^3$, where C_l has been defined as

$$C_l \;=\; \frac{1}{2l+1}\sum_{m=-l}^{l} M_{lmlm}\,. \tag{2.32}$$

The sizes chosen are those that give the best fit to data (see section 2.5). The $l = 2$ power is reduced by 20% for $\mathscr{M}_0$, and the ratio of power spectra oscillates and rapidly approaches unity. The two differ by less than 0.5% at $l = 30$ for all three topologies.

2.4 Likelihood Calculation

The matrix $M_{lml'm'}$ computed as discussed above is compared to the experimental data from the 7-year WMAP survey. Since rotational invariance is broken, we need to vary the orientation of the torus relative to axes fixed in space, to find the best fit. We do this by rotating the data relative to the torus in computing the likelihood function. We specify the orientation by three Euler angles (ϕ, θ, ψ) in the following way. The axes x, y, z are fixed in the coordinate frame of the CMB data, i.e. the observed universe, and the x', y', z' axes are fixed in the torus. Start with the CMB-fixed and torus-fixed axes aligned. Rotate the torus counterclockwise around the z-axis by angle ϕ, then around the *new* x-axis by angle θ, then

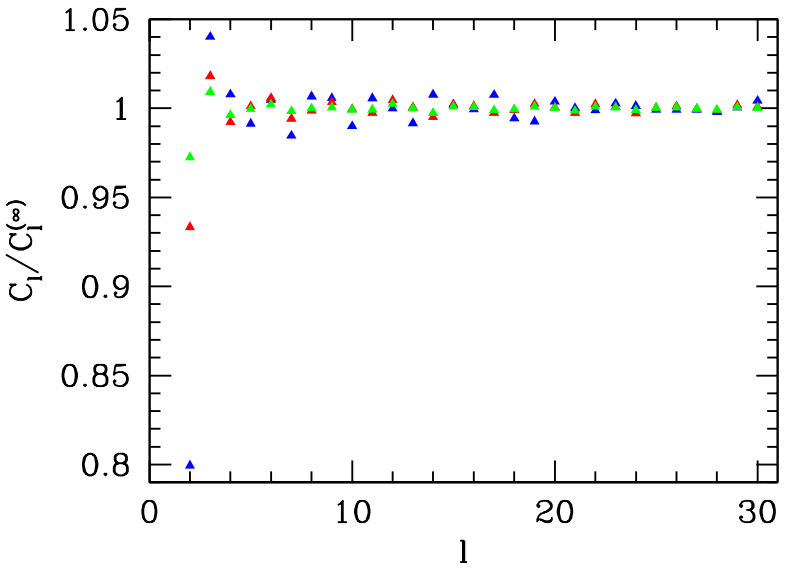

Figure 2.2: Plot of the ratio of C_l for $\mathscr{M}_0 = \mathbb{T}^3$ with $L/L_0 = 1.8$ (blue), $\mathscr{M}_1 = \mathbb{T}^2 \times \mathbb{R}^1$ with $L/L_0 = 1.9$ (red), and $\mathscr{M}_3 = S^1 \times \mathbb{R}^2$ with $L/L_0 = 1.9$ (green), to that for infinite space $\mathbb{R}^3$.

around the *new* z-axis by angle ψ to get the final torus orientation. The angles θ and $\phi - \pi/2$ give the spherical polar angles of the z-axis of the torus while the angle ψ gives the orientation of the torus around its z-axis. We can make use of the symmetries of our topologies to speed up the calculation since various Euler angles can give equivalent orientations of the torus. Two sets of Euler angles (ϕ, θ, ψ) and (ϕ', θ', ψ') are equivalent if $\exists g \in G$ such that

$$R(\phi, \theta, \psi) = R(g)\, R(\phi', \theta', \psi') \tag{2.33}$$

where $R(\phi, \theta, \psi)$ is the coordinate transformation rotation matrix corresponding to (ϕ, θ, ψ) and $R(g)$ is that corresponding to the discrete element g. This defines an equivalence relation on the set of all possible Euler angles. We take a uniform grid on all possible angles, then divide that grid into equivalence classes according to Eq. (2.33) and take one representative from each class. We have scanned over ~ 4000 inequivalent angles.

Different orientations of the torus were considered in the previous analysis of first-year WMAP data for $\mathbb{T}^3$ [17], but they only considered a uniform grid on the range $0 \leq \phi, \theta, \psi \leq \pi/2$. Note that this does not cover all possible orientations

of $\mathbb{T}^3$. The first two angles describe the orientation of the z-axis and by their assumption on the range of ϕ, θ, ψ, the z-axis always lies in the first octant. However taking into account all the symmetries of the cube there are 6 equivalent axes that can play the role of the z-axis, the $\pm x$, $\pm y$, and $\pm z$ axes, while there are 8 octants. In other words, there are possible orientations of the cube for which none of the 6 axes lies in the first octant.

After choosing a torus orientation, we calculate the likelihood in the real space of orientations on the last scattering surface. For N_p pixels the likelihood function is given by[2]

$$\mathscr{L} = \frac{1}{(2\pi)^{N_p/2}(\det C)^{1/2}} \exp\left(-\frac{1}{2}\Delta^T C^{-1}\Delta\right) , \tag{2.34}$$

and the χ^2 function by

$$\chi^2 = \Delta^T C^{-1}\Delta \, , \tag{2.35}$$

where Δ_i is the vector of pixels and C_{ij} is the covariance matrix. The indices i, j label the different pixels, which are in directions $\hat{\mathbf{n}}_{i,j}$ on the sky. The covariance matrix C_{ij} in the WMAP code includes the theoretical covariance matrix, the so-called cosmic variance, as well as an additional noise contribution. We use a modified WMAP code in which the theoretical covariance matrix for the infinite universe has been replaced by that for one of our topologies. The WMAP noise covariance matrix is left unchanged.

We now describe how to convert the matrix $M_{lml'm'}$ to obtain the modified covariance matrix C_{ij}. The temperature fluctuation measured in a pixel i is given by [36]

$$\Theta_i = \int \mathrm{d}\hat{\mathbf{n}} \; \Theta(\hat{\mathbf{n}}) B_i(\hat{\mathbf{n}}) \, , \tag{2.36}$$

where B_i is the beam pattern at the pixel i and is specific to the experiment. Usually the beam patterns have the same shape for every pixel and are axially symmetric around the center of the pixel, as is the case for WMAP, so if we denote the direction to the center of the pixel by $\hat{\mathbf{n}}_i$ then the beam pattern can be

[2]Likelihood is denoted by $\mathscr{L}$ everywhere in this chapter, to distinguish it from the length L.

decomposed into spherical harmonics

$$B_i(\hat{\mathbf{n}}) = \sum_{lm} B_l Y_{lm}(\hat{\mathbf{n}}_i) Y^*_{lm}(\hat{\mathbf{n}}) \,. \tag{2.37}$$

Using Eq. (2.19) to decompose $\Theta(\hat{\mathbf{n}})$ into spherical harmonics, we get for the theoretical covariance matrix

$$C_{ij} \equiv \langle \Theta_i \Theta_j \rangle = \sum_{lml'm'} M_{lml'm'} B_l B_{l'} Y_{lm}(\hat{\mathbf{n}}_i) Y^*_{l'm'}(\hat{\mathbf{n}}_j) \,. \tag{2.38}$$

In computing C_{ij}, we have to vary the orientation of the torus relative to the sky. In implementing the Euler angle rotation, one can compute the $M_{lml'm'}$ matrix in the torus-fixed coordinate system, so that it remains unchanged as the Euler angles are varied. The pixel directions $\mathbf{n}_i$ are changed to $\mathbf{n}_i \to R(\phi,\theta,\psi)\,\mathbf{n}_i$. Equivalently, one can work in the CMB-fixed coordinate system, and rotate the torus, which gives $M_{lml'm'}$ transformed by the angular momentum rotation matrices,

$$M_{lml'm'} \;\; \to \;\; \sum_{n,n'} M_{lnl'n'} D^{(l)*}_{nm}(R) D^{(l')}_{n'm'}(R) \,. \tag{2.39}$$

Note that in the infinite universe case, Eq. (2.28) holds, and the result Eq. (2.38) simplifies to

$$C_{ij} = \sum_l \frac{2l+1}{4\pi} B_l^2 \, C_l \, P_l(\hat{\mathbf{n}}_i \cdot \hat{\mathbf{n}}_j) \,, \tag{2.40}$$

independent of the rotation $R(\phi,\theta,\psi)$, which is the standard expression.

The computation of the covariance matrix using Eq. (2.38) is more involved than the infinite case, Eq. (2.40), so the likelihood calculations require far more computer time than the conventional case. C_{ij} must be recalculated for each set of Euler angles. There are 458403 independent elements in $M_{lml'm'}$ for $2 \le l \le 30$ of which 57840 satisfy the $l \equiv l' \,(\mathrm{mod}\, 2), m \equiv m' \,(\mathrm{mod}\, 4)$ condition, and 2482 values for each of the indices i and j. The slowest step in the computation is evaluating the sums on l, m, l', m' in Eq. (2.38) for all values of $\{i, j\}$.

An Euler angle rotation of the sky maps points on the sphere to rotated points on the sphere. For infinitesimal pixels, this corresponds to a reshuffling of the pixels, i.e. if pixel i at $\mathbf{n}_i$ is mapped by the rotation to $\mathbf{n}_j$, then pixel $i \to$ pixel j. An exact reshuffling of pixels would greatly simplify the computation —

instead of recomputing C_{ij}, one could simply permute the indices on C_{ij} to get the transformed matrix. In particular, $\det C$ would remain invariant under this transformation.

The WMAP pixels have been chosen using the HEALPix grid [38]. The pixels are chosen to lie along lines of constant lattitude, and they have equal solid angles. This implies that the spacing of the pixels varies as a function of lattitude. As a result one cannot treat rotations of the sky as a pixel reshuffling transformation. One can approximate the rotations by a pixel transformation by mapping the rotated pixel to the one closest to it in the HEALPix grid. The likelihood computed using this method differs from the exact result using Eq. (2.38), and is not accurate enough for our purposes. The above approximate relation between rotations and pixel permutations does, however, explain why $\det C$ is approximately independent of the Euler angles.

For a finite universe, one has to use Eq. (2.38) with the value for $M_{lml'm'}$ computed as described in Sec. 2.3. The finiteness of the universe only affects the large-scale anisotropies, so the difference between the infinite and finite cases goes to zero with increasing l. For that reason we will look only at low-l portion of anisotropies, $l \leq 30$, and use the infinite manifold result Eq. (2.40) for $l > 30$. We calculate χ^2 and the likelihood $\mathscr{L}$ using a modification of the likelihood code provided by the WMAP team [28, 29, 30] as a function of the new parameters (L, ϕ, θ, ψ). Since we are interested only in low-l effects we use the low-resolution portion of the likelihood code. We use the experimental data in the exact same form as provided by the WMAP team without any further modifications. The temperature map used is the smoothed and degraded ILC map with the Kp2 mask applied to remove the galactic plane and strong point sources. The map originally has 3072 pixels, but only 2482 are left after the mask. For the reasons discussed in section 2.1, we use only the temperature-temperature correlations for our analysis, so we disregard the portion of the WMAP likelihood code that uses the polarization data.

Ideally, one would have to do a fit to the experimental data varying the four new parameters (L, ϕ, θ, ψ) in addition to all the other cosmological parameters.

The cosmological parameters affect the whole spectrum of anisotropies while only the low-l part of the spectrum is affected by the new parameters, so we fix the other cosmological parameters at their best-fit values as given by the seven-year WMAP data [30] and only vary the new parameters. The values of the cosmological parameters that we use are [30] $100\Omega_b h^2 = 2.227$, $\Omega_c h^2 = 0.1116$, $\Omega_\Lambda = 0.729$, $n_s = 0.966$, $\tau = 0.085$, $\Delta^2_R(0.002\,\mathrm{Mpc}^{-1}) = 2.42 \times 10^{-9}$.

2.5 Results

We have computed the likelihood and χ^2 for the three cases, $\mathscr{M}_0 = \mathbb{T}^3$, $\mathscr{M}_1 = \mathbb{T}^2 \times \mathbb{R}^1$ and $\mathscr{M}_2 = S^1 \times \mathbb{R}^2$, for different values of L/L_0 as a function of the Euler angles. L/L_0 ranges between a minimum value of $0.5 - 1.0$ depending on the manifold, and a maximum value of $L/L_0 = 2.6$, in steps of $L/L_0 = 0.1$. By the time $L/L_0 = 2.6$, the results are almost identical to the flat-space case $\mathscr{M}_\infty = \mathbb{R}^3$. For the statistical analysis discussed later in this section, we have used interpolation to construct a smooth function of L.

The relation between likelihood and χ^2 is

$$-2\ln\mathscr{L} \;=\; \chi^2 + \ln\det C/C_f + \ln\det(2\pi C_f) \tag{2.41}$$

where C_f is a fiducial covariance matrix used by the WMAP collaboration. C_f is independent of L and the Euler angles, and drops out of all likelihood ratios. χ^2 and $-2\ln\mathscr{L}$ differ by $\ln\det C/C_f$ (up to an irrelevant constant). The likelihood for $\mathscr{M}_\infty$, three-dimensional flat space, will be denoted by $\mathscr{L}_\infty$, and is $-2\ln\mathscr{L}_\infty = 3573.4$.[3]

As noted earlier, for fixed L/L_0, $\ln\det C/C_f$ varies weakly with the Euler angles. In Fig. 2.3, we have plotted the variation of $\ln\det C/C_f$ as a function of ψ, for fixed values of the ϕ, θ, at $L/L_0 = 1.8$. The overall variation of $\ln\det C/C_f$ against ψ is less than 1.

$-2\ln\mathscr{L}$ (and hence χ^2) has a strong variation with Euler angles at fixed L/L_0. In Fig. 2.4, we have shown plots of the variation of $2\ln\mathscr{L}_\infty - 2\ln\mathscr{L}$ with

[3] All the likelihood values given in this chapter are calculated using the temperature data only.

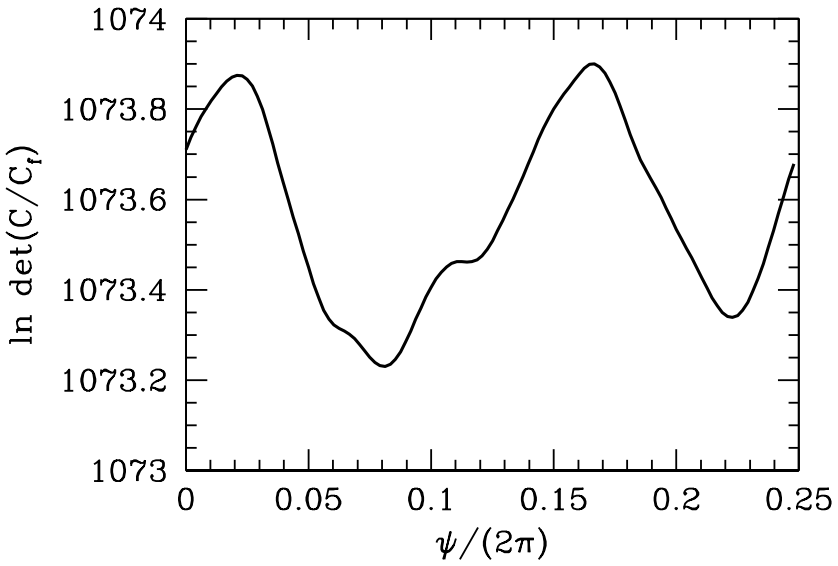

Figure 2.3: Plot of $\ln\det C/C_f$ against the Euler angle ψ for fixed ϕ, θ for the $\mathscr{M}_0$ topology at $L/L_0 = 1.8$,

Euler angle ψ for fixed ϕ, θ for the $\mathscr{M}_0$ topology. $\mathscr{L}_\infty$ is independent of the Euler angles. The solid red curve has been chosen to have $L/L_0 = 1.8$, and ϕ, θ values that maximize the likelihood at this value of L/L_0. There is a large variation of $-2\ln\mathscr{L}$ with the remaining Euler angle ψ, and the global minum of $-2\ln\mathscr{L}$ is $2\ln\mathscr{L}_\infty - 2\ln\mathscr{L} = -17.2$ at $\psi/(2\pi) \approx 0.05$. The strong dependence of $-2\ln\mathscr{L}$ on orientation makes it difficult to find the true global minimum of the $-2\ln\mathscr{L}$ and χ^2 functions. We have done a scan over all Euler angles with a spacing of 0.05π, to identify valleys, followed by a finer scan to find the mininum. By comparing our numerical minimum with the next best point, we can estimate the uncertainty in our minimum $-2\ln\mathscr{L}$ and χ^2 values at less than 0.5. The dashed blue curve in Fig. 2.4 is also for $L/L_0 = 1.8$, but with ϕ, θ fixed at random values, rather than those for which $-2\ln\mathscr{L}$ vs. ψ passes through the global minimum. There is still considerable dependence as one varies the third angle ψ, but the dependence is much weaker than for the solid red curve. The dependence of $-2\ln\mathscr{L}$ drops rapidly with increasing L/L_0. For $L/L_0 = 2.2$, the dotted green curve in the figure, the overall variation is about 6.5.

The plot of χ^2 and $-2\ln\mathscr{L}$ against L/L_0 is given in Fig. 2.5, 2.6, and 2.7 for

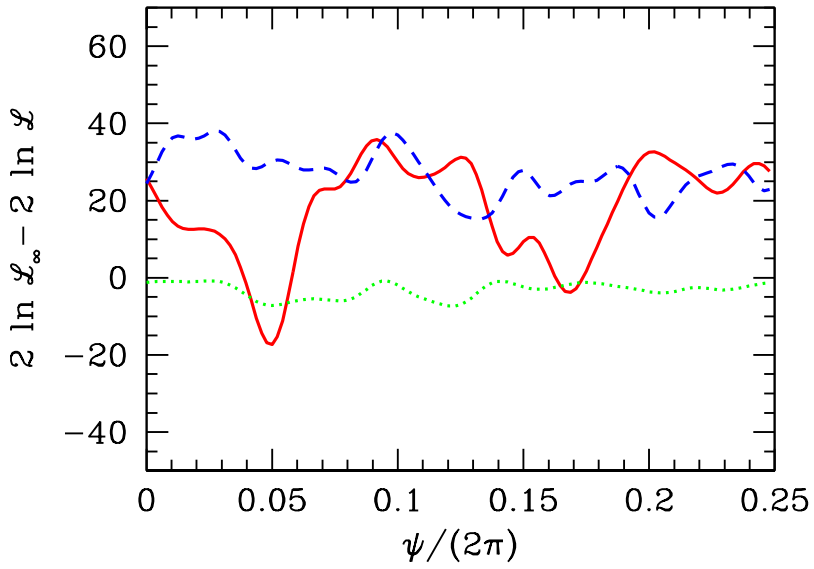

Figure 2.4: Plot of $2\ln\mathscr{L}_\infty - 2\ln\mathscr{L}$ against the Euler angle ψ for fixed ϕ, θ for the $\mathscr{M}_0$ topology. The solid red and dashed blue curves are for two different values of ϕ, θ at $L/L_0 = 1.8$, and the dotted green curve is for $L/L_0 = 2.2$. The solid red curve is for $L/L_0 = 1.8$ with ϕ, θ fixed to be the best fit values, the dashed blue curve is for $L/L_0 = 1.8$ with ϕ, θ fixed in a random direction, and the dotted green curve is for $L/L_0 = 2.2$ with ϕ, θ fixed to be the best fit values.

the three cases, $\mathscr{M}_0 = \mathbb{T}^3$, $\mathscr{M}_1 = \mathbb{T}^2 \times \mathbb{R}^1$ and $\mathscr{M}_2 = S^1 \times \mathbb{R}^2$, respectively. We have plotted the maximum and minimum of χ^2 over all possible orientations of the torus at each value of L. There is a significant variation in χ^2 as a function of orientation, as noted earlier, and some orientations are strongly preferred over others. In each plot, χ^2 ranges between the uppermost and lowermost solid black curves, as one varies the orientation of the manifold by varying the Euler angles (ϕ, θ, ψ). For the smallest values of L/L_0, $\Delta\chi^2$ between the worst and best orientations is 377, 191, and 156 for $\mathscr{M}_{0,1,2}$, respectively. As L/L_0 increases, the effect of a compactified direction decreases. By the time $L/L_0 = 2.6$, the fit results are very close to the case of the infinite manifold $\mathbb{R}^3$, and $\Delta\chi^2 \leq 4$ for the different orientations.

We have been unable to find any pattern to the best-fit orientation ϕ, θ, ψ of the torus as a function of L/L_0. We have examined the possibility that the manifolds we consider are aligned along the axis of evil. To do this, we have chosen the preferred axis of the manifold (the z-axis for $\mathbb{T}^3$, the $\mathbb{R}$ direction for $\mathbb{T}^2 \times \mathbb{R}^1$ and the S^1 direction for $S^1 \times \mathbb{R}^2$) to point along the axis-of-evil direction $b = 60^\circ$, $l = -100^\circ$ in galactic coordinates, and allowed for arbitrary rotations of the manifold around this direction. All the angles are varied with step $\pi/100 = 1.8^\circ$. This gives a subset of all the orientations we have considered, and the χ^2 range has been plotted as the dashed colored curves in the figure. The colored curves lie between the black curves (as they must), but they do not lie towards the best-fit χ^2 line. This shows that there is nothing in our computation that picks out the axis-of-evil as a preferred direction.

2.5.1 Limit on Size of Compact Directions

We use a goodness-of-fit test to see whether we can rule out the hypothesis that the universe has topology $\mathscr{M}_i$ of size L. The minimum χ^2 values are $\chi^2 = 2469,\ 2467,\ 2472$ at $L/L_0 = 2.1,\ 2.1,\ 2.2$ for $\mathscr{M}_{0,1,2}$, respectively. The goodness-of-fit test depends on the overall value of χ^2 (rather than χ^2 differences) to see how well the compact universe hypothesis agrees with the data. We use Pearson's χ^2 test with 2478 degrees of freedom (there are 2482 pixels, 4 free parameters) to put a lower bound on L. Plots of χ^2 as a function of L are shown in Fig. 2.5,

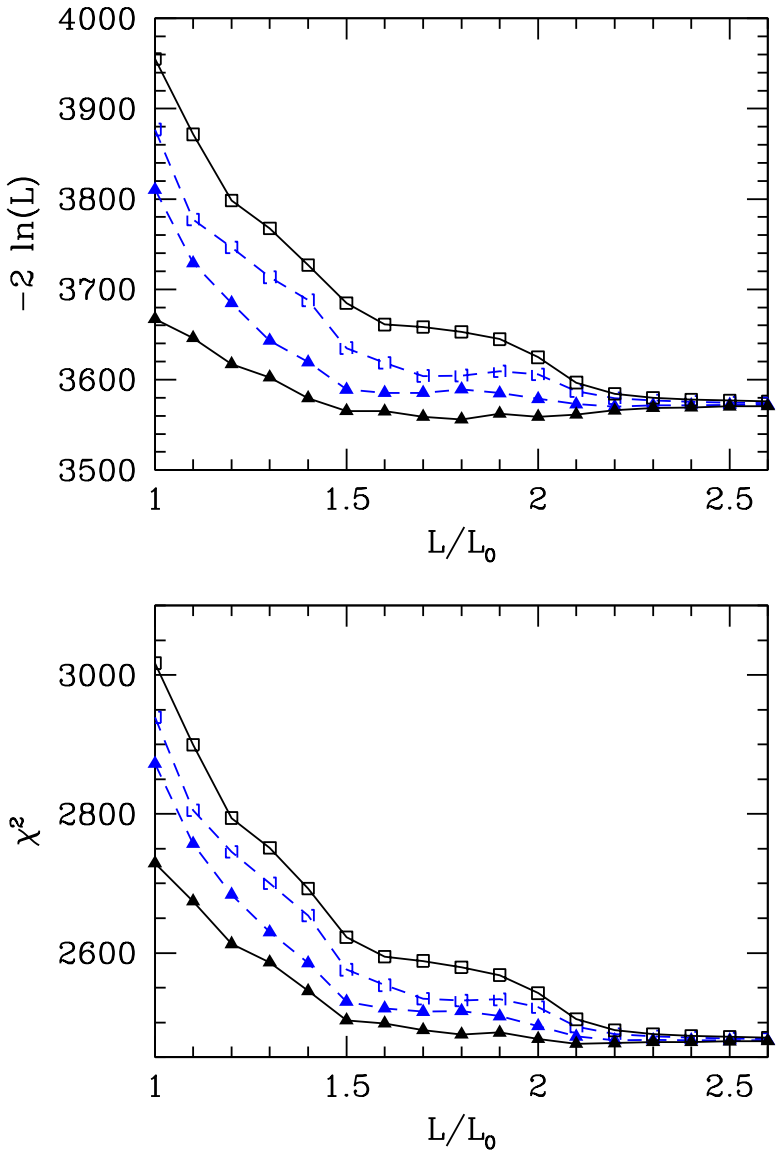

Figure 2.5: Plot of $-2\ln\mathscr{L}$ and χ^2 against L/L_0 for different Euler angles (ϕ,θ,ψ) for the topology $\mathscr{M}_0=\mathbb{T}^3$. The lower solid curve (solid triangles) is the minimum of $-2\ln\mathscr{L}$ or χ^2, and the upper solid curve (open squares) is the maximum of $-2\ln\mathscr{L}$ and χ^2 as the Euler angles are varied for fixed L. The lower dashed colored curve (solid triangles) and upper dashed colored curve (open squares) are the minimum and maximum of $-2\ln\mathscr{L}$ and χ^2 with a symmetry axis of the manifold restricted to point along the axis of evil.

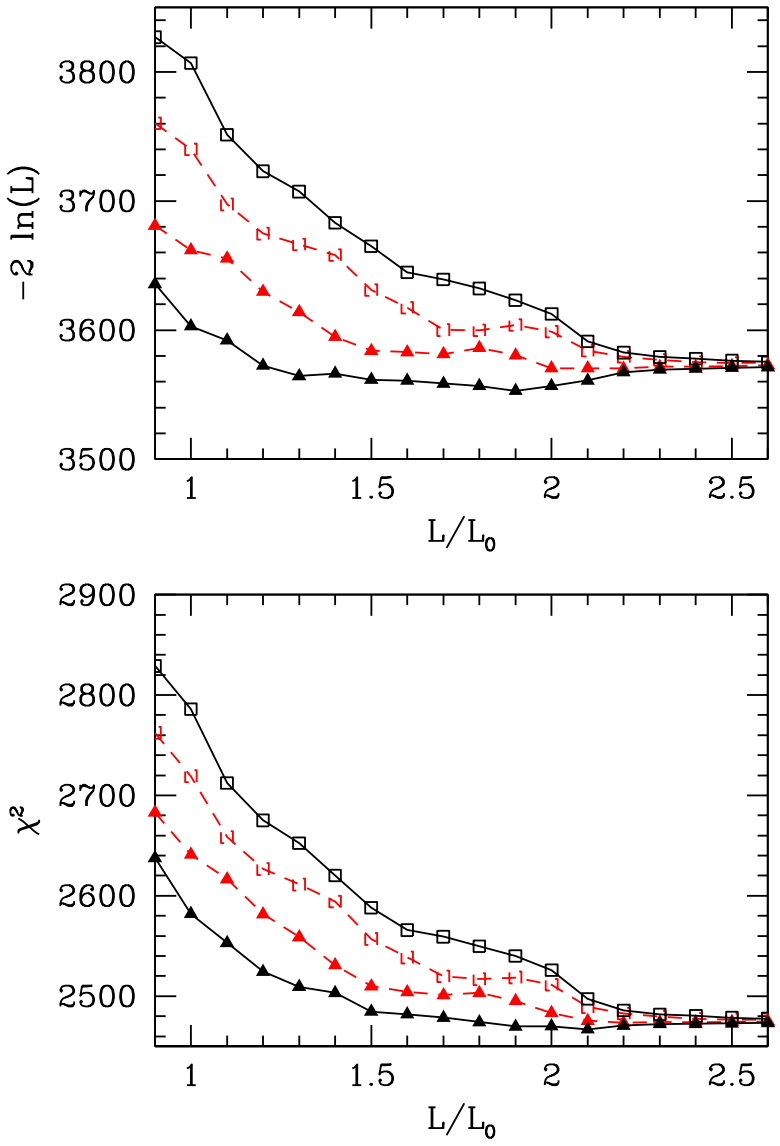

Figure 2.6: Plot of $-2\ln\mathscr{L}$ and χ^2 against L/L_0 for different Euler angles (ϕ, θ, ψ) for the topology $\mathscr{M}_1 = \mathbb{T}^2 \times \mathbb{R}^1$. See the caption of Fig. 2.5 for the explanation of the different curves.

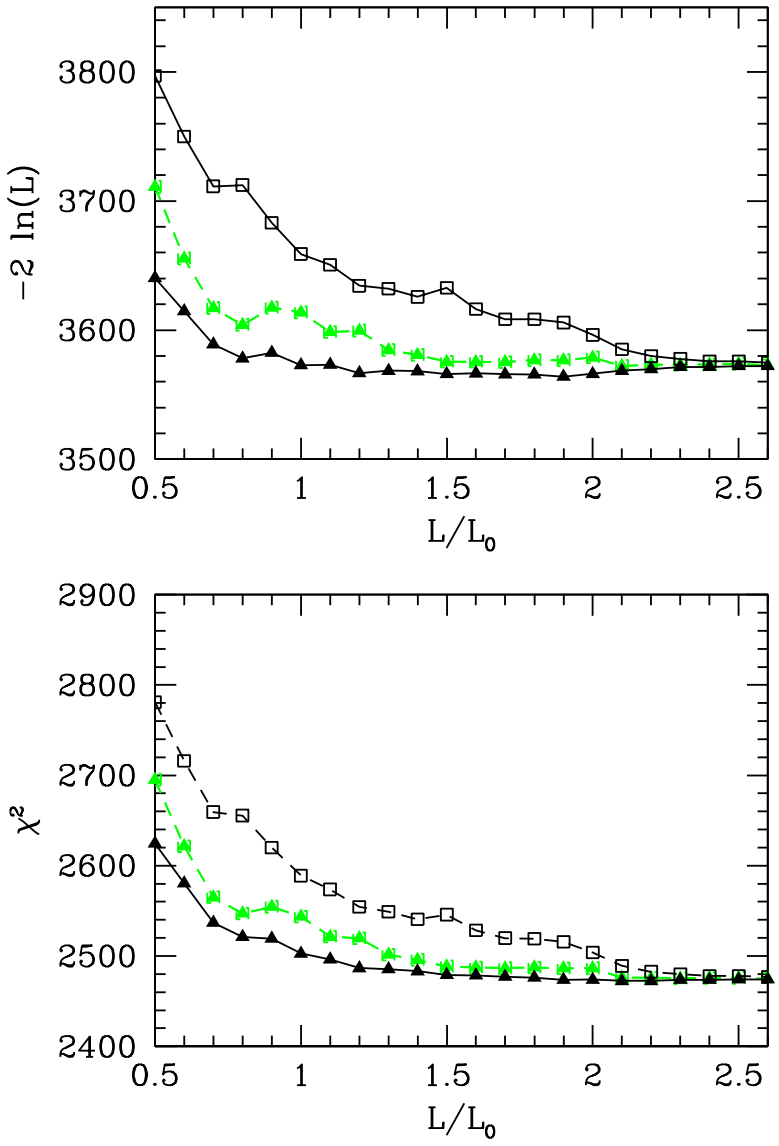

Figure 2.7: Plot of $-2\ln\mathscr{L}$ and χ^2 against L/L_0 for different Euler angles (ϕ, θ, ψ) for the topology $\mathscr{M}_2 = S^1 \times \mathbb{R}^2$. See the caption of Fig. 2.5 for the explanation of the different curves.

Table 2.1: Limits on L/L_0 using the χ^2 goodness-of-fit test. Values of L/L_0 less than those in the table are excluded at the confidence level given in the first column.

C.L.	$\mathscr{M}_0$	$\mathscr{M}_1$	$\mathscr{M}_2$
68%	1.48	1.29	0.96
90%	1.35	1.04	0.62
95%	1.27	0.97	0.57

2.6, and 2.7 for the three cases $\mathscr{M}_{0,1,2}$. Using the computed values of χ^2 we have the limits given in Table 2.1. Values of L/L_0 smaller than those listed in the table are excluded at the confidence levels given. The bounds get weaker from $\mathscr{M}_0 \to \mathscr{M}_1 \to \mathscr{M}_2$, as the number of infinite dimensions increases from zero to one to two.

Phillips and Kogut have also found a best fit value of $L/L_0 \sim 2.1$ for $\mathscr{M}_0$ [17]. We put a slightly stronger constraint at 95% for $\mathscr{M}_0$ than [17] (1.27 vs. 1.2), but our 68% constraint is weaker (1.48 vs. 2.1). This discrepancy may be explained by the fact that they did not consider all the non-equivalent orientations of the torus (as discussed earlier in section 2.4). Also, as we have shown, χ^2 oscillates very rapidly with changing the orientation, and it is important to use a small enough step size to find the minimum of χ^2.

2.5.2 Confidence Intervals

We estimate confidence intervals for L/L_0 using the maximum likelihood method. This depends on likelihood ratios, i.e. on differences of $\ln \mathscr{L}$. A detailed discussion can be found in the Review of Particle Properties [39, §33], and in Refs. [40, 41]. This is a standard method for estimating confidence intervals in high energy physics. Plots of likelihood as a function of L are shown in Fig. 2.5, 2.6, and 2.7. The maximum likelihood value is at $L/L_0 = 1.8, 1.9, 1.9$ for $\mathscr{M}_{0,1,2}$,

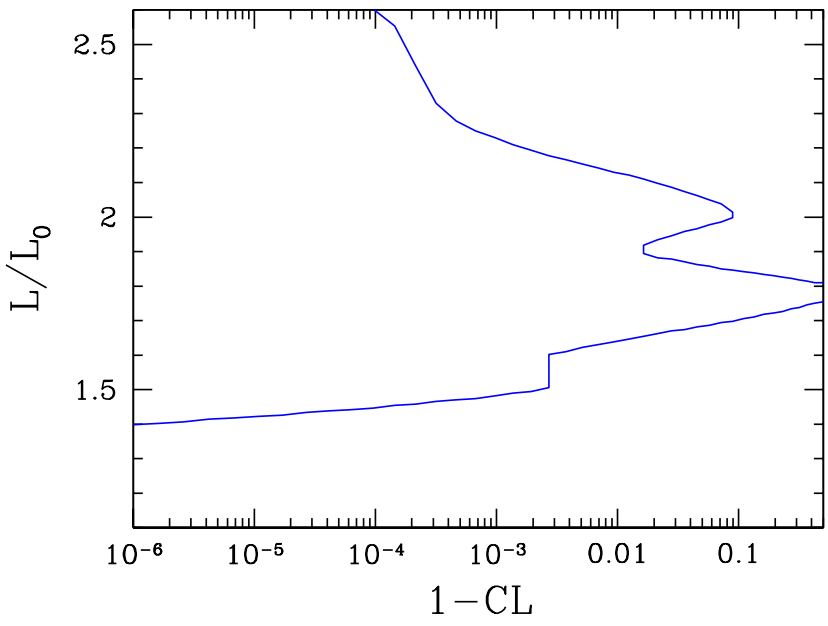

Figure 2.8: Plot of the L/L_0 confidence interval as a function of the confidence level for $\mathscr{M}_0 = \mathbb{T}^3$.

respectively. The confidence intervals for L/L_0 are determined by using $\Delta \ln \mathscr{L}$, the difference of $\ln \mathscr{L}$ from the value that maximizes the likelihood function [40, 41]. Plots of the L/L_0 confidence intervals as a function of $1-\alpha$, where α is the confidence level, are shown in Fig. 2.8, 2.9, and 2.10. The data shows a preference for a finite universe with size $L/L_0 \sim 1.9$ corresponding to $L \sim 27$ Gpc. The allowed L range extends to $L/L_0 \geq 2.6$ at a confidence level $\alpha = 10^{-4}$ for $\mathscr{M}_0$, 2×10^{-5} for $\mathscr{M}_1$ and 4×10^{-3} for $\mathscr{M}_2$. Thus the data show evidence for a finite universe at a confidence level $\alpha = 2 \times 10^{-5}$ for the $\mathbb{T}^2 \times \mathbb{R}^1$ topology. The 95% confidence intervals are $L/L_0 \in [1.7, 2.1]\,,\ [1.8, 2.0]\,,\ [1.2, 2.1]$ for $\mathscr{M}_{0,1,2}$, respectively.

Our best fit value of $L/L_0 \sim 1.9$ is at the edge of the exclusion region obtained using the circles in the sky method [16] (they put a lower bound on L of 27.9 Gpc corresponding to $L/L_0 \approx 1.94$). All our 95% confidence intervals extend into the allowed region. This means that we find no contradiction to that previous result, but one might be able to get better constraints by combining the two methods.

We have scanned over ~ 4000 different orientations for each value of L, with

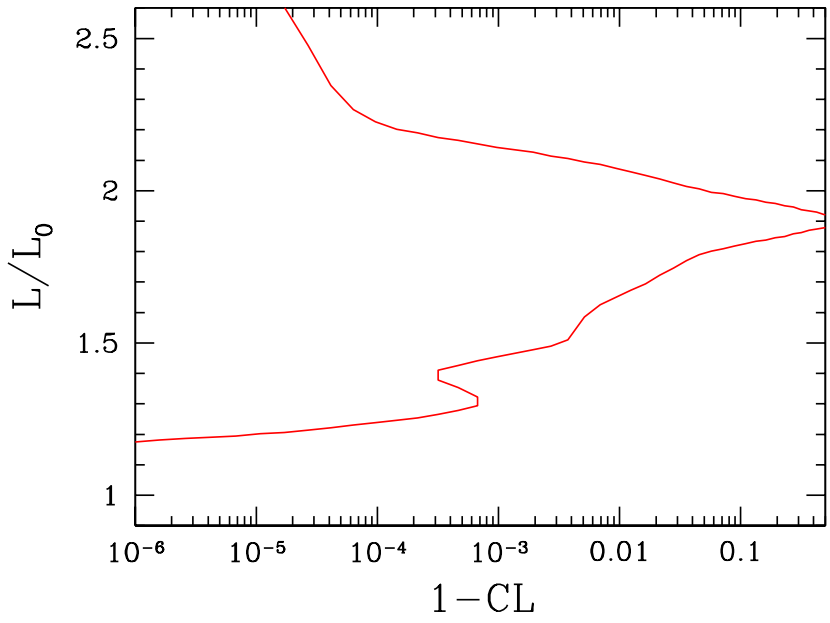

Figure 2.9: Plot of the L/L_0 confidence interval as a function of the confidence level for $\mathscr{M}_1 = \mathbb{T}^2 \times \mathbb{R}^1$.

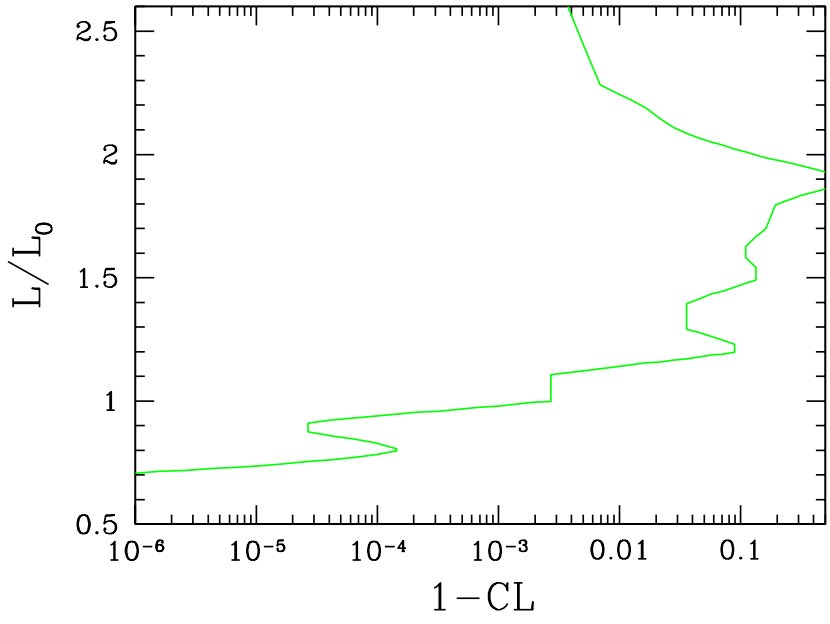

Figure 2.10: Plot of the L/L_0 confidence interval as a function of the confidence level for $\mathscr{M}_2 = S^1 \times \mathbb{R}^2$.

a finer scan near the minima, so that the error in χ^2 and $-2\ln\mathscr{L}$ is ≤ 0.5. The difference in $-2\ln\mathscr{L}$ between its value at $L\to\infty$ and its minimum value (which occurs at $L/L_0 = 1.9$ for $\mathscr{M}_1$) is 20.4, which is well outside possible numerical errors. Note that the main numerical uncertainty is finding the true minimum of $-2\ln\mathscr{L}$ for finite values of L. The minimum value of $-2\ln\mathscr{L}$ has been determined with an accuracy ≤ 0.5. The actual difference in likelihoods between finite and infinite L can only be greater than what we have found. There is an indication that a finite universe fits the data better than an infinite one. However, the "standard" 5σ-criterion for a discovery, corresponding to a confidence level $\alpha = 5.7\times 10^{-7}$, includes the value $L=\infty$.

The Euler angles for the best fit case $\mathscr{M}_1$ with $L/L_0 = 1.9$ are $(\phi = 21^\circ \pm 2^\circ, \theta = 53^\circ \pm 2^\circ, \psi = 61^\circ \pm 2^\circ)$ which corresponds, for the infinite direction, to $(b = 37^\circ \pm 2^\circ, l = 291^\circ \pm 2^\circ)$ in galactic coordinates and $(\alpha = 182^\circ \pm 2^\circ, \delta = -25^\circ \pm 2^\circ)$ in J2000 equatorial coordinates. This is close to the direction $(b = 30^\circ \pm 2^\circ, l = 276^\circ \pm 3^\circ)$ of the velocity of the Local Group inferred from the CMB dipole [42]. We discuss the possibility that our signal is due to a dipole contamination in Sec. 2.6.2.

For the topology $\mathscr{M}_0$ the best fit size is $L/L_0 = 1.8$ and the Euler angles are $(\phi = 117^\circ \pm 2^\circ, \theta = 162^\circ \pm 2^\circ, \psi = 18^\circ \pm 2^\circ)$ which corresponds, for the three axes, to $(b = 5^\circ \pm 2^\circ, l = 100^\circ \pm 2^\circ)$, $(b = 17^\circ \pm 2^\circ, l = 8^\circ \pm 2^\circ)$, and $(b = -72^\circ \pm 2^\circ, l = 27^\circ \pm 2^\circ)$ in galactic coordinates. The improvement in $-2\ln\mathscr{L}$ is 17.2. For the topology $\mathscr{M}_2$ the best fit size is $L/L_0 = 1.9$ and the Euler angles are $(\phi = 9^\circ \pm 2^\circ, \theta = 27^\circ \pm 2^\circ)$[4] which corresponds, for the finite direction, to $(b = 63^\circ \pm 2^\circ, l = -81^\circ \pm 2^\circ)$ in galactic coordinates. The improvement in $-2\ln\mathscr{L}$ is 9.6. We can see that the best fit directions for the three topologies are all very different from each other, which means that the improvement in likelihood for one of the topologies is not simply mimicking the improvement for another topology.

[4]For $\mathscr{M}_2$ the likelihood has no dependence on the angle ψ because of the rotational symmetry around the finite axis of $\mathscr{M}_2$.

2.5.3 Fisher Information

The Fisher information can be used to compute the variance V of the length L determined using the maximum likelihood method. The Fisher information is given by

$$\begin{aligned} V^{-1} &= \frac{1}{2}\left\langle \left(\frac{\partial h}{\partial L}\right)^2 \right\rangle = \mathrm{Tr}\, C\frac{\partial C^{-1}}{\partial L}C\frac{\partial C^{-1}}{\partial L} \\ &= \mathrm{Tr}\, C^{-1}\frac{\partial C}{\partial L}C^{-1}\frac{\partial C}{\partial L}\,. \end{aligned} \tag{2.42}$$

Using the covariance matrix C for the $\mathscr{M}_1$ topology with $L/L_0 = 1.9$ gives

$$V^{-1} = 3.3 \times 10^3 \tag{2.43}$$

so that the error estimate for L/L_0 is $\sqrt{V} = 0.017$. The Fisher information error Eq. (2.43) corresponds to using a quadratic approximation to the likelihood function about its minimum to determine the error, and gives a smaller error than that obtained earlier using the exact likelihood function.

2.6 Checks

We have been unable to find a simple explanation for the better fit due to a finite topology. However, there are some possibilities which we can test.

The measured cosmic microwave background anisotropy has a smaller value for the quadrupole power C_2 than the theoretical expectation value. There is a large cosmic variance in C_2, so this is not a discrepancy between theory and experiment. Fig. 2.2 shows that the predicted value of C_2 for a finite universe is reduced from the infinite universe value. The greater likelihood for a finite universe is not due to lowering the value of C_2. We have checked this by determining the likelihood using $M_{lml'm'}$ for the finite case, but with the $l = l' = 2$ values replaced by their values for the infinite universe. For $\mathscr{M}_1$ with $L/L_0 = 1.9$, $-2\ln\mathscr{L}$ increases by 0.43, which is much less than the 20.4 difference in $-2\ln\mathscr{L}$ from the infinite universe.

As another test, we have computed the likelihood for all three topologies for their best fit sizes ($L/L_0 = 1.8$ for $\mathscr{M}_0$, $L/L_0 = 1.9$ for $\mathscr{M}_1$ and $\mathscr{M}_2$) by using a

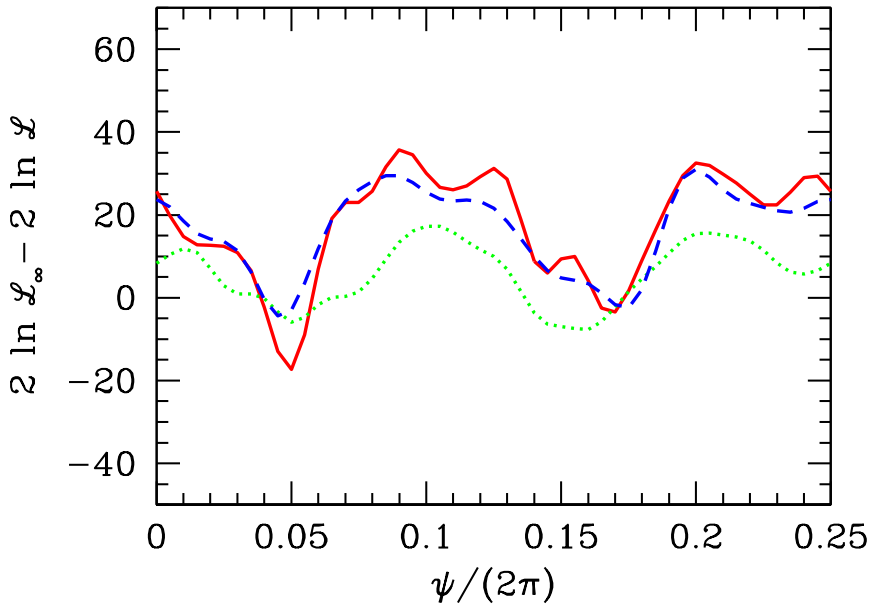

Figure 2.11: Plot of $2\ln\mathscr{L}_\infty - 2\ln\mathscr{L}$ against the Euler angle ψ for fixed ϕ, θ for the $\mathscr{M}_0$ topology for $L/L_0 = 1.8$. The solid red curve uses the full matrix $M_{lml'm'}$, the dashed blue curve uses the matrix truncated to $5 \le l, l' \le 20$, and the dotted green curve uses the matrix $M_{lml'm'}\delta_{ll'}$, retaining only the part diagonal in l.

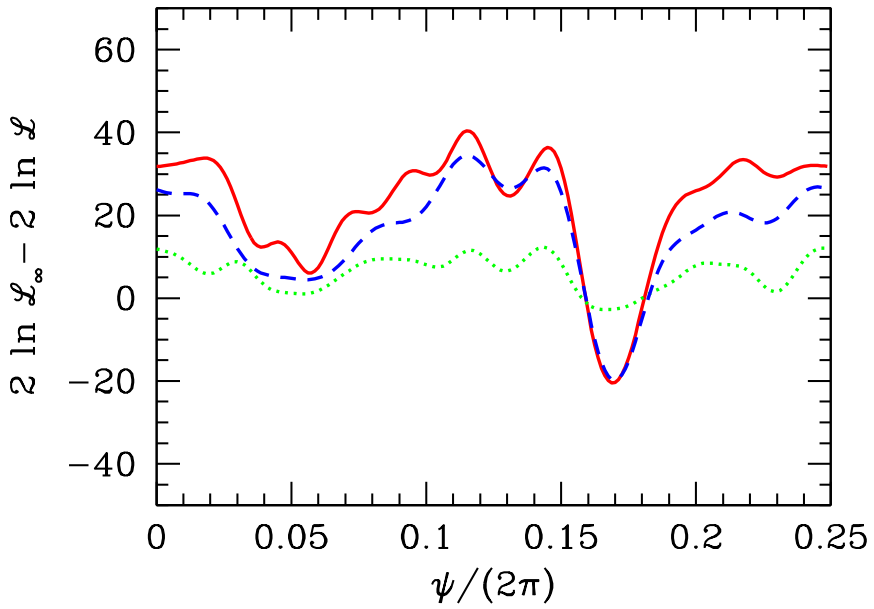

Figure 2.12: Plot of $2\ln\mathscr{L}_\infty - 2\ln\mathscr{L}$ against the Euler angle ψ for fixed ϕ, θ for the $\mathscr{M}_1$ topology for $L/L_0 = 1.9$. See the caption of Fig. 2.11 for the explanation of the different curves.

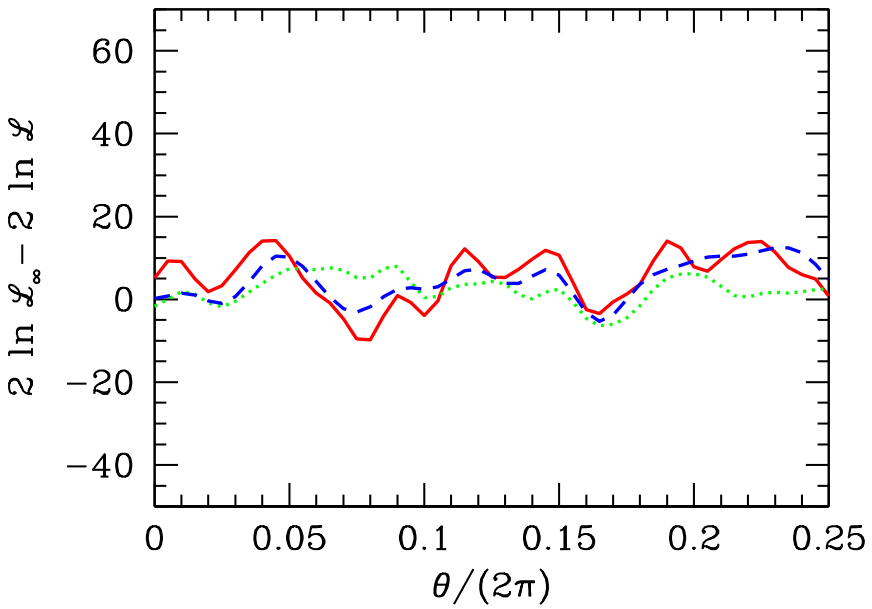

Figure 2.13: Plot of $2\ln\mathscr{L}_\infty - 2\ln\mathscr{L}$ against the Euler angle θ for fixed ϕ, ψ for the $\mathscr{M}_2$ topology for $L/L_0 = 1.9$. The $\mathscr{M}_2$ plot uses θ, since the likelihood does not depend on ψ. See the caption of Fig. 2.11 for the explanation of the different curves.

truncated $M_{lml'm'}$ matrix. The truncated matrix is constructed by using $M_{lml'm'}$ for the finite topology for $5 \leq l, l' \leq 20$, and using $M_{lml'm'}$ for the infinite universe, i.e. $M_{lml'm'} = C_l \delta_{ll'} \delta_{mm'}$, for l and or l' outside this range. A plot of the likelihood as a function of the Euler angle ψ for the topologies $\mathscr{M}_0$ and $\mathscr{M}_1$, and as a function of the Euler angle θ for the topology ${\mathscr{M}_2}^4$ for this truncated $M_{lml'm'}$ is plotted as the dashed blue curves in Fig. 2.11, 2.12, and 2.13, respectively. This can be compared with the likelihood curves using the full $M_{lml'm'}$ for the finite topology, shown as the solid red curves. The dip in the likelihood difference to -20.4 (for $\mathscr{M}_1$ which gives the best fit) is the signal that the finite topology is a better fit than the infinite universe. The plot for the truncated matrix is similar to that for the full matrix, except that the small-angle fluctuations have been smoothed out, as is to be expected since higher l terms have been dropped. Note that the dip in $2\ln\mathscr{L}_\infty - 2\ln\mathscr{L}$ is very similar in both cases, and the minimum of $2\ln\mathscr{L}_\infty - 2\ln\mathscr{L}$ is nearly the same. This shows that the effect we find is not due to the low-l modes (quadrupole, octupole), and is also not an edge effect as a result of only using $l \leq 30$

in the computation. For $5 \leq l, l' \leq 20$, $M_{lml'm'}$ has 86736 elements of which 11056 satisfy the $l \equiv l' \,(\mathrm{mod}\, 2), m \equiv m' \,(\mathrm{mod}\, 4)$ condition and are non-zero.

The off-diagonal elements in $M_{lml'm'}$ are important for the calculations. We have also computed the likelihood by retaining only the elements which are diagonal in l, i.e. using $M_{lml'm'}\delta_{ll'}$. This drops the elements in $M_{lml'm'}\delta_{ll'}$ which are off-diagonal in l, while retaining the elements which are off-diagonal in m for a given l. The likelihood with this matrix is the dashed green curves in Fig. 2.11, 2.12, and 2.13. With this matrix, the likelihood deviates much less from the infinite universe, and the dip near $\psi/(2\pi) \approx 0.17$ (for $\mathscr{M}_1$) is much less pronounced.

2.6.1 Monte-Carlo Skies

The results of the previous section were obtained using a likelihood analysis of the WMAP7 data. One can study whether the better fit of a finite topology is due to a statistical fluctuation. Since the big-bang is not a repeatable experiment, this must be done by generating random Monte-Carlo data for the pixels Δ_i, and redoing the analysis for this Monte-Carlo data. To actually do this numerically is beyond the computing power we have available. Luckily, for the problem at hand, we can analyze the Monte-Carlo problem analytically, since the entire analysis pipeline is linear.

Assume that the pixels Δ_i are generated by the covariance matrix C_∞ for an infinite universe, so that the probability distribution is

$$p(\Delta) \;=\; \frac{1}{\sqrt{\det(2\pi C_\infty)}} \exp\left(-\frac{1}{2}\Delta^T C_\infty^{-1}\Delta\right) . \tag{2.44}$$

The likelihood function computed using Δ_i and covariance matrix C (of a finite universe) is

$$-2\log\mathscr{L} \;=\; \Delta^T C^{-1}\Delta + \ln\det(2\pi C)\,, \tag{2.45}$$

and the likelihood constructed using the covariance matrix C_∞ of the infinite universe is

$$-2\log\mathscr{L}_\infty \;=\; \Delta^T C_\infty^{-1}\Delta + \ln\det(2\pi C_\infty)\,. \tag{2.46}$$

Let

$$h \equiv (-2\log\mathscr{L}_\infty) - (-2\log\mathscr{L}) \,, \tag{2.47}$$

be the difference of the two log-likelihoods. In our analysis, we found $h = 20.4 > 0$, so that the finite universe was more likely than the infinite universe. The average value of h over Monte-Carlo data can be computed using Eq. (2.44) and Eq. (2.47). The two-point function is

$$\langle \Delta_i \Delta_j \rangle = (C_\infty)_{ij} \,, \tag{2.48}$$

so that

$$\langle h \rangle = N - \mathrm{Tr}\, C^{-1} C_\infty + \ln\det(C_\infty) - \ln\det(C) \,. \tag{2.49}$$

It is convenient to define the symmetric matrix

$$S = C_\infty^{1/2} C^{-1} C_\infty^{1/2} \,, \tag{2.50}$$

which is a positive matrix since C and C_∞ are positive matrices, and has eigenvalues $s_i > 0$. In terms of S,

$$\langle h \rangle = N - \mathrm{Tr}\, S + \ln\det S = \sum_i \left[1 - s_i + \ln s_i\right] \,. \tag{2.51}$$

The function $1 - s + \ln s \leq 0$ with its maximum at 0 when $s = 1$. Thus

$$\langle h \rangle \leq 0 \tag{2.52}$$

and $\langle h \rangle = 0$ only if $S = \mathbf{1}$, i.e. $C = C_\infty$. This gives the intuitively obvious result that the best fit for data generated with covariance matrix C_∞ is, on average, given by fitting using the same covariance matrix C_∞. Any other covariance matrix C used for fitting, on average, gives a lower likelihood.

If instead of Eq. (2.47) we had used the difference of χ^2,

$$h_\chi \equiv \chi^2_\infty - \chi^2, \tag{2.53}$$

then

$$\langle h_\chi \rangle = N - \mathrm{Tr}\, C^{-1} C_\infty = N - \mathrm{Tr}\, S = \sum_i \left[1 - s_i\right] \,, \tag{2.54}$$

and $\langle h_\chi \rangle$ could have either sign, since $s_i > 0$, but need not be smaller than 1. For example, a simple rescaling, $C = \lambda C_\infty$, with $\lambda \to \infty$ can always make $\chi^2 \to 0$, its minimum poissible value. This option is eliminated for likelihood because of the $\det(2\pi C)$ term.

Using C for the best-fit topology $\mathscr{M}_1$ with $L/L_0 = 1.9$, we find the numerical values

$$\begin{aligned} N &= 2482\,, \\ \ln\det(C_\infty/C_f) &= 1097.8\,, \\ \ln\det(C/C_f) &= 1082.73\,, \\ \mathrm{Tr}\, C^{-1}C_\infty &= \mathrm{Tr}\, S = 2516.6\,, \end{aligned} \tag{2.55}$$

so that

$$\langle h \rangle = -19.5\,. \tag{2.56}$$

This differs from the value we find of $h = +20.4$ by $\Delta h = h - \langle h \rangle = 39.9$. The probability that Δh is a statistical fluctuation can be determined by computing the variance of h using the four-point function

$$\langle \Delta_i \Delta_j \Delta_k \Delta_l \rangle = (C_\infty)_{ij} (C_\infty)_{kl} + (C_\infty)_{ik} (C_\infty)_{jl} + (C_\infty)_{il} (C_\infty)_{jk}\,, \tag{2.57}$$

to obtain

$$\begin{aligned} \left\langle (\Delta h)^2 \right\rangle &= 2N + 2\,\mathrm{Tr}\, C^{-1}C_\infty C^{-1}C_\infty - 4\left(\mathrm{Tr}\, C^{-1}C_\infty\right) \\ &= 2\,\mathrm{Tr}\,\left(1 - C^{-1}C_\infty\right)^2 = 2\,\mathrm{Tr}\,\left(1 - S\right)^2\,. \end{aligned} \tag{2.58}$$

In our case,

$$\mathrm{Tr}\, C^{-1}C_\infty C^{-1}C_\infty = 2610.0\,, \tag{2.59}$$

so that

$$\left\langle (\Delta h)^2 \right\rangle = 117.6 = (10.8)^2\,. \tag{2.60}$$

Our observed value of $\Delta h = 39.9$ is $3.7\,\sigma$ away from the mean, so the probability that a fluctuation gives h larger than or equal to our observed value is 1.1×10^{-4}, assuming a normal distribution.

While the distribution of the data Δ_i is Gaussian, the distribution of the likelihood difference h is no longer Gaussian. We can also compute higher order connected correlation functions of h,

$$\left\langle (\Delta h)^r \right\rangle_c \;=\; 2^r\;(r-1)!\;\mathrm{Tr}\;\left(1-C^{-1}C_\infty\right)^r = 2^r\;(r-1)!\;\mathrm{Tr}\;(1-S)^r\;, \tag{2.61}$$

from the generating function

$$\begin{aligned}\log\left\langle e^{\lambda\Delta h}\right\rangle &= -\lambda\mathrm{Tr}\,(1-C^{-1}C_\infty) - \frac{1}{2}\mathrm{Tr}\,\ln\left[1-2\lambda(1-C^{-1}C_\infty)\right] \\ &= -\lambda\mathrm{Tr}\,(1-S) - \frac{1}{2}\mathrm{Tr}\,\ln\left[1-2\lambda(1-S)\right]\,,\end{aligned} \tag{2.62}$$

so that

$$\begin{aligned}\left\langle (\Delta h)^3\right\rangle &= 8\;\mathrm{Tr}\;\left(1-C^{-1}C_\infty\right)^3 \\ \left\langle (\Delta h)^4\right\rangle_c &= 48\;\mathrm{Tr}\;\left(1-C^{-1}C_\infty\right)^4\,,\end{aligned} \tag{2.63}$$

where the fourth-order correlation is

$$\left\langle (\Delta h)^4\right\rangle \;=\; \left\langle (\Delta h)^4\right\rangle_c + 3\left\langle (\Delta h)^2\right\rangle^2\,, \tag{2.64}$$

in terms of the connected correlation. The mean value $\langle h\rangle$, and all the connected correlation functions $\langle(\Delta h)^r\rangle_c$ are of order N, the number of data points. Thus the relative correlation $\langle(\Delta h)^r\rangle\,/\,\langle h\rangle^r$ is of order N^{1-r}.

The numerical values for our case are

$$\begin{aligned}\left\langle (\Delta h)^3\right\rangle &= -489.0\,, \\ \left\langle (\Delta h)^4\right\rangle_c &= 4303.7\,.\end{aligned} \tag{2.65}$$

We can get a better estimate of the probability that $h = 20.4$ is due to a statistical fluctuation by using these higher order moments. We have fit $\langle h\rangle$ and $\langle(\Delta h)^r\rangle$, $r = 2, 3, 4$ to a probability distribution

$$p(h) \;=\; p_0\exp[-(h-h_0)^2 - c_2(h-h_0)^2 - c_3(h-h_0)^3 - c_4(h-h_0)^4]\,, \tag{2.66}$$

and found using this distribution that the probability that $h - \langle h\rangle \geq 39.9$ is 10^{-6}, which is smaller than the value obtained earlier using a normal distribution for h.

2.6.2 Dipole Contamination

The symmetry axis of $\mathscr{M}_1$ points in the direction ($b = 37° \pm 2°, l = 291° \pm 2°$), which is close to the direction of the velocity of the Local Group ($b = 30° \pm 2°, l = 276° \pm 3°$) [42]. The CMB has a large dipole asymmetry of $3.358 \pm 0.001 \pm 0.023\,\mathrm{mK}$ in the direction ($b = 48.05° \pm 0.11°, l = 264.31° \pm 0.2°$) [42]. Suppose that the data is contaminated by a dipole contribution that has not been properly subtracted out.[5] Could a residual dipole explain the results we have found?

To study the effect of a residual dipole, assume that the observed pixels are

$$\Delta_i^{\rm obs} \;=\; \Delta_i + \mathbf{p}\cdot\hat{\mathbf{n}}_i = \Delta_i + d_i, \qquad d_i = \mathbf{p}\cdot\hat{\mathbf{n}}_i \tag{2.67}$$

where Δ_i are the true fluctuations given by the distribution Eq. (2.44), $\mathbf{p}$ is the residual dipole contamination in the data, and $\hat{\mathbf{n}}_i$ are the directions of the pixels. Then Eq. (2.45,2.46) are replaced by

$$\begin{aligned} -2\log\mathscr{L} &= (\Delta+d)^T C^{-1}(\Delta+d) + \ln\det(2\pi C)\,, \\ -2\log\mathscr{L}_\infty &= (\Delta+d)^T C_\infty^{-1}(\Delta+d) + \ln\det(2\pi C_\infty)\,. \end{aligned} \tag{2.68}$$

From these, we find

$$\begin{aligned} \langle h\rangle &= N - \mathrm{Tr}\, C^{-1}C_\infty + \ln\det(C_\infty) - \ln\det(C) \\ &\quad +(d^T C_\infty^{-1} d) - (d^T C^{-1} d)\,, \\ \left\langle \Delta h^2\right\rangle &= 2N - 8 d^T C^{-1} d + 4 d^T C_\infty^{-1} d + 4 d^T C^{-1} C_\infty C^{-1} d \\ &\quad +2\mathrm{Tr}\, C^{-1}C_\infty C^{-1}C_\infty - 4\left(\mathrm{Tr}\, C^{-1}C_\infty\right)\,. \end{aligned} \tag{2.69}$$

Dipole contamination produces a systematic shift in h from its value in Eq. (2.49) given by the $(d^T C_\infty^{-1} d) - (d^T C^{-1} d)$ terms, which can be written as

$$(d^T C_\infty^{-1} d) - (d^T C^{-1} d) \;=\; p_\alpha p_\beta D_{\alpha\beta} \tag{2.70}$$

in term of the components $p_\alpha = (p_x, p_y, p_z)$ of the dipole.

$$D_{\alpha\beta} = ((\hat{\mathbf{n}}_i)_\alpha^T C_\infty^{-1}(\hat{\mathbf{n}}_i)_\alpha) - ((\hat{\mathbf{n}}_i)_\alpha^T C^{-1}(\hat{\mathbf{n}}_i)_\alpha) \tag{2.71}$$

[5] This possibility was suggested to us by B. Keating.

Using the covariance matrices for the infinite universe C_∞ and our best fit case C, and the directions of the pixels $\hat{\mathbf{n}}_i$ in cartesian coordinates we find

$$D = \begin{bmatrix} -1.22 & -0.004 & -0.114 \\ -0.004 & -0.0281 & -0.003 \\ -0.114 & -0.003 & -0.0127 \end{bmatrix} \mathrm{mK}^{-2} \tag{2.72}$$

The largest eigenvalue is $-1.23\,\mathrm{mK}^{-2}$. To get a shift in $-2\ln\mathscr{L}$ of 20.4 requires a dipole contamination $|\mathbf{p}|$ of around 4 mK. This is larger than the observed dipole, and several hundred times the quoted uncertainty in the CMB dipole [42]. Thus any allowed dipole contamination (which must be much smaller than 4 mK) only has a negligible effect on the likelihood, and does not explain our results.

2.7 Conclusions

We have analyzed the possibility that the universe has compact topologies $\mathscr{M}_0 = \mathbb{T}^3$, $\mathscr{M}_1 = \mathbb{T}^2 \times \mathbb{R}^1$ and $\mathscr{M}_2 = S^1 \times \mathbb{R}^2$ using WMAP7 data. The analysis used a simple modification of the available CAMB and WMAP 7-year likelihood codes. The only changes to the standard code were to replace the integral over $\mathbf{k}$ by a discrete sum in computing the theoretical covariance matrix (cosmic variance). The Pearson goodness-of-fit test gives 95% bounds of $L/L_0 \geq 1.27, 0.97, 0.57$ for the three cases, respectively.

Surprisingly, we find a statistically significant signal of $\Delta(-2\ln\mathscr{L}) = -20.4$ for a universe with compact spatial dimensions, and the best fit topology is $\mathscr{M}_1$. The best fit results for $\mathscr{M}_1$ have symmetry axis which is near ($\sim 10^\circ$) the direction of the Local Group velocity. An infinite universe is compatible with the data at a confidence level of 2×10^{-5} (i.e. $4.3\,\sigma$). The maximum likelihood 95% confidence intervals are $1.7 \leq L/L_0 \leq 2.1$, $1.8 \leq L/L_0 \leq 2.0$, $1.2 \leq L/L_0 \leq 2.1$ for the three cases, respectively. We find that the most probable universe has the compact topology $\mathscr{M}_1$. We find no evidence of a preference for the axis-of-evil direction. The improved fit for a finite universe is not due to the lowered prediction for the quadrupole anisotropy; this accounts for only a small fraction of the increase in likelihood.

We have done several checks to investigate the reason for our results. We find that the signal is predominantly due to off-diagonal elements in the covariance matrix $M_{lml'm'}$ for $5 \leq l \leq 20$. It would be useful to investigate whether any systematic effects in the WMAP data introduce effects with cubic symmetry that can mimic the effects of a torus topology. The best fit results do not pick out any special orientation for the torus, such as a torus with symmetry axis perpendicular to the galactic plane, that might lead to systematic effects that lead to a fake signal. Pixelization of the data using the HEALPix grid also should not introduce cubic symmetry terms along an axis not aligned with the galactic pole.

Chapter 2, in full, is a reprint of the material as it appears on JCAP 06 (2012) 003. Aslanyan, Grigor; Manohar, Aneesh V., 2012. The dissertation author was the primary investigator and author of this paper.

Chapter 3

Constraints on Semiclassical Fluctuations in Primordial Universe

3.1 Introduction

The standard model of cosmology assumes a homogeneous and isotropic universe, and this assumption is in good agreement with the observational data from the CMB (cosmic microwave background) radiation and galaxy surveys. However, recent studies have shown possible deviations from this. One popular possibility that has been discussed in the literature is the existence of the "axis of evil" - a special direction in which the first few multipoles of CMB anisotropies seem to be aligned [31, 32, 33]. The direction of the axis of evil is $b = 60°$, $l = -100°$ in galactic coordinates.

A possible deviation from standard cosmology that has been extensively studied in the literature is the non-trivial topology of the universe. In chapter 2 we showed that the trivial $\mathbb{R}^3$ topology is compatible with the seven-year WMAP data only at 4.3σ level, unless there is some strong systematic error in the data or some other yet undiscovered effect which mimics a non-trivial topology.

The fluctuations in CMB radiation are directly generated from the quantum

perturbations during inflation, so it is possible that the observed anisotropy of the universe comes directly from the inflationary perturbations. The possibility of a linearly modulated primordial power spectrum was discussed in [43], where an improvement in χ^2 of about 9 was found for 3 extra parameters, using the three-year WMAP data. They found the direction of the modulation to be $b = 34^{+17+36+65}_{-17-35-51}$, $l = 63^{+28+59+105}_{-26-58-213}$ with 68%, 95%, and 99.7% confidence respectively.

In this chapter we consider two other scenarios that might explain the possible anomalies on large scales mentioned above. Firstly, we consider a semiclassical fluctuation in one of the Fourier modes of primordial perturbations. Since each Fourier mode is periodic in space, this scenario may generate effects similar to that of a non-trivial topology. We want to understand if a fluctuation in one mode can give an alternative explanation for the results obtained in chapter 2.[1] Since this scenario brakes the isotropy of space by introducing a special direction, it might also give an explanation to the axis of evil.

The second scenario we consider is a semiclassical gaussian fluctuation somewhere in space. This possibility might be a result of inflation not starting in the Bunch-Davies vacuum state. Again, the isotropy of space is broken (unless the fluctuation is centered directly at our position) so we check if the axis of evil could be a result of such a fluctuation. We test these hypotheses using the most recent seven-year temperature data from WMAP.

This chapter is organized as follows. In section 3.2 we describe the likelihood calculation for CMB data, in section 3.3 we present our results, we discuss some checks we have performed in section 3.4, and we conclude in section 3.5.

3.2 Likelihood Calculation

In order to test our hypotheses we calculate the likelihood of WMAP data under the assumption of having a perturbation in one Fourier mode or a gaussian perturbation. The likelihood calculation for standard cosmology is discussed in some standard textbooks (see, e.g. [36]), here we will briefly summarize that

[1] This possibility was suggested to us by Lawrence Krauss.

calculation and show how it needs to be modified for our case.

3.2.1 Standard Cosmology

The temperature anisotropies $\Theta(\hat{\mathbf{n}}, \mathbf{x})$ are decomposed into spherical harmonics

$$\Theta(\hat{\mathbf{n}}, \mathbf{x}) = \sum_{lm} a_{lm}(\mathbf{x}) Y_{lm}(\hat{\mathbf{n}}) \tag{3.1}$$

where $\hat{\mathbf{n}}$ is the direction of observation, $\mathbf{x}$ is the location of observation, i.e. our position in space. The coefficients $a_{lm}(\mathbf{x})$ are further transformed to Fourier space

$$a_{lm}(\mathbf{x}) = \int \frac{\mathrm{d}^3 k}{(2\pi)^3} e^{i\mathbf{k}\cdot\mathbf{x}} \int \mathrm{d}\Omega \; Y^*_{lm}(\hat{\mathbf{n}}) \Theta(\hat{\mathbf{n}}, \mathbf{k}) \tag{3.2}$$

Assuming gaussian perturbations, we have

$$\langle a_{lm}(\mathbf{x}) \rangle = 0 \tag{3.3}$$

and all the information is in the two-point function

$$M_{lml'm'} \equiv \langle a_{lm}(\mathbf{x}) a^*_{l'm'}(\mathbf{x}) \rangle \tag{3.4}$$

The temperature anisotropies $\Theta(\mathbf{k}, \hat{\mathbf{n}})$ can be expressed in terms of initial gauge invariant curvature perturbations $\zeta(\mathbf{k})$ on uniform density hypersurfaces

$$\Theta(\mathbf{k}, \hat{\mathbf{n}}) = \zeta(\mathbf{k}) \frac{\Theta(k, \mathbf{k}\cdot\hat{\mathbf{n}})}{\zeta(k)} \tag{3.5}$$

where the ratio $\Theta(k, \mathbf{k}\cdot\hat{\mathbf{n}})/\zeta(k)$ does not depend on the initial curvature perturbations. It is determined from the evolution of Θ and ζ, and only depends on the magnitude of $\mathbf{k}$ and the direction of $\hat{\mathbf{n}}$ relative to $\mathbf{k}$ [36].

For homogeneous and isotropic gaussian perturbations the initial curvature perturbations are completely described by the power spectrum

$$\langle \zeta(\mathbf{k}) \zeta^*(\mathbf{k}') \rangle \equiv (2\pi)^3 \delta^3(\mathbf{k} - \mathbf{k}') P(k) \tag{3.6}$$

Expanding $\Theta(k, \mathbf{k}\cdot\hat{\mathbf{n}})$ into Legendre polynomials

$$\Theta(k, \mathbf{k}\cdot\hat{\mathbf{n}}) = \sum_l (-i)^l (2l+1) P_l(\hat{k}\cdot\hat{\mathbf{n}})\Theta_l(k) \tag{3.7}$$

the covariance matrix (3.4) takes the form

$$M_{lml'm'} = \delta_{ll'}\delta_{mm'}C_l \tag{3.8}$$

with

$$C_l = \frac{2}{\pi}\int \mathrm{d}k\ k^2\, P(k) \left|\frac{\Theta_l(k)}{\zeta(k)}\right|^2 . \tag{3.9}$$

Likelihood is calculated in real space. For N_p pixels the likelihood function has the form

$$\mathscr{L} = \frac{1}{(2\pi)^{N_p/2}(\det C)^{1/2}} \exp\left(-\frac{1}{2}\Delta^T C^{-1}\Delta\right) \tag{3.10}$$

where Δ_i is the vector of pixels of temperature anisotropies and C_{ij} is the covariance matrix, including noise. This covariance matrix is obtained by transforming $M_{lml'm'}$ into real space. This way the likelihood function becomes a function of the cosmological parameters since the covariance matrix depends on them.

3.2.2 Semiclassical Fluctuation in One Fourier Mode

Now suppose that in addition to the standard fluctuations (3.6) there is a fixed periodic fluctuation with momentum $\mathbf{k_0}$:

$$\zeta(\mathbf{x}) = \zeta_{st}(\mathbf{x}) + a_0 \cos(\mathbf{k_0}\cdot\mathbf{x}) \tag{3.11}$$

where $\zeta_{st}(\mathbf{x})$ are the standard fluctuations. Then

$$\zeta(\mathbf{k}) = \zeta_{st}(\mathbf{k}) + (2\pi)^3 a_0 \frac{\delta^3(\mathbf{k}-\mathbf{k_0}) + \delta^3(\mathbf{k}+\mathbf{k_0})}{2} \tag{3.12}$$

which results in

$$a_{lm}(\mathbf{x}) = a^{st}_{lm}(\mathbf{x}) + a^{lp}_{lm}(\mathbf{x}) \tag{3.13}$$

$$a^{lp}_{lm}(\mathbf{x}) = 2\pi a_0 (-i)^l \frac{\Theta_l(k_0)}{\zeta(k_0)} Y^*_{lm}(\hat{k}_0)\left(e^{i\alpha} + (-1)^l e^{-i\alpha}\right) \tag{3.14}$$

where a_{lm}^{st} is the standard part, $a_{lm}^{lp}(\mathbf{x})$ is the extra term from the large perturbation, α is a phase depending on our position $\mathbf{x}$ relative to the fluctuation:

$$\alpha = \mathbf{k_0} \cdot \mathbf{x} \tag{3.15}$$

The covariance matrix takes the form

$$\begin{aligned} M_{lml'm'} &= \delta_{ll'}\delta_{mm'}C_l + (4\pi)^2(-i)^l i^{l'} a_0^2 \frac{\Theta_l(k_0)}{\zeta(k_0)} \frac{\Theta_{l'}^*(k_0)}{\zeta(k_0)} Y_{lm}^*(\hat{k_0}) Y_{l'm'}(\hat{k_0}) \\ &\quad \times \frac{1 + (-1)^{l+l'} + (-1)^{l'} e^{2i\alpha} + (-1)^l e^{-2i\alpha}}{4} \end{aligned} \tag{3.16}$$

The large perturbation is described by 5 parameters - the magnitude a_0, the wavelength $\lambda = 2\pi/k_0$, the direction $\hat{k}_0$ (2 parameters), and the phase α. In order to find the maximum likelihood we need to use this new covariance matrix (3.16) in likelihood (3.10), and maximize it as a function of all the cosmological parameters plus our newly introduced 5 parameters. However, this is very time consuming, mainly because the covariance matrix now has non-diagonal terms as well. We will take a slightly different approach.

As we mentioned before, one of the main reasons of considering a large perturbation is to try to give an alternative explanation for the observed signal of non-trivial topology in chapter 2. Since the size of possible non-trivial topology found in chapter 2 and other works is comparable to the size of the observable universe, we will assume that the large perturbation wavelength is also of the same order as the size of the observable universe. This means that our modification will affect only the low-l part of the covariance matrix. Since the standard cosmological parameters are determined from the whole spectrum of l, we fix their values at their best-fit values as given by the seven-year WMAP data [30] and only vary the new parameters.[2] So the covariance matrix for the gaussian part of perturbations is fixed, and we can calculate the likelihood using (3.10) with the standard gaussian covariance matrix, but replacing Δ_i by $\Delta_i - \Delta_i^{lp}$ with

$$\Delta_i^{lp} = \int \mathrm{d}\hat{\mathbf{n}}\, \Theta^{lp}(\hat{\mathbf{n}}) B_i(\hat{\mathbf{n}}) \tag{3.17}$$

[2]The values of the cosmological parameters that we use are $100\Omega_b h^2 = 2.227$, $\Omega_c h^2 = 0.1116$, $\Omega_\Lambda = 0.729$, $n_s = 0.966$, $\tau = 0.085$, $\Delta_R^2(0.002\,\mathrm{Mpc}^{-1}) = 2.42 \times 10^{-9}$.

where $B_i(\hat{\mathbf{n}})$ is the beam pattern of pixel i and

$$\Theta^{lp}(\hat{\mathbf{n}}, \mathbf{x}) = \sum_{lm} a^{lp}_{lm}(\mathbf{x}) Y_{lm}(\hat{\mathbf{n}}) \tag{3.18}$$

is the additional large perturbation term to the temperature fluctuations in real space.

The beam pattern is specific to the experiment. Usually the beam patterns have the same shape for every pixel and are axially symmetric around the center of the pixel, as is the case for WMAP, so if we denote the direction to the center of the pixel by $\hat{\mathbf{n}}_i$ then the beam pattern can be decomposed into spherical harmonics

$$B_i(\hat{\mathbf{n}}) = \sum_{lm} B_l Y_{lm}(\hat{\mathbf{n}}_i) Y^*_{lm}(\hat{\mathbf{n}})\,. \tag{3.19}$$

Then (3.17) takes the form

$$\begin{aligned}
\Delta^{lp}_i &= \sum_{lml'm'} \int \mathrm{d}\hat{\mathbf{n}}\, a^{lp}_{lm}(\mathbf{x}) Y_{lm}(\hat{\mathbf{n}}) B_{l'} Y_{l'm'}(\hat{\mathbf{n}}_i) Y^*_{l'm'}(\hat{\mathbf{n}}) \\
&= \sum_{lm} a^{lp}_{lm}(\mathbf{x}) B_l Y_{lm}(\hat{\mathbf{n}}_i) \\
&= 2\pi a_0 \sum_{lm} B_l Y_{lm}(\hat{\mathbf{n}}_i)(-i)^l \frac{\Theta_l(k_0)}{\zeta(k_0)} Y^*_{lm}(\hat{k}_0) \left(e^{i\alpha} + (-1)^l e^{-i\alpha}\right)
\end{aligned}$$

$$\Delta^{lp}_i = \frac{a_0}{2} \sum_l (2l+1)(-i)^l B_l P_l(\hat{\mathbf{n}}_i \cdot \hat{k}_0) \left(e^{i\alpha} + (-1)^l e^{-i\alpha}\right) \frac{\Theta_l(k_0)}{\zeta(k_0)} \tag{3.20}$$

Now likelihood becomes a function of only our 5 parameters, with a fixed covariance matrix. Since the normalization constant for likelihood is now fixed, all we need to worry about is χ^2

$$\chi^2 = \Delta^T C^{-1} \Delta \tag{3.21}$$

3.2.3 Semiclassical Gaussian Fluctuation in Space

Let us now consider the second scenario, namely a semiclassical gaussian "bump" somewhere in space in addition to (3.6):

$$\zeta(\mathbf{x}) = \zeta_{st}(\mathbf{x}) + a_0 e^{-(\mathbf{x}-\mathbf{x}_c)^2/w^2} \tag{3.22}$$

$$\zeta(\mathbf{k}) = \zeta_{st}(\mathbf{k}) + a_0 w^3 \pi^{3/2} e^{-\mathbf{k}^2 w^2/4} e^{-i\mathbf{k}\cdot\mathbf{x}_c} \tag{3.23}$$

$$a_{lm}(\mathbf{x}) = a^{st}_{lm}(\mathbf{x}) + a^{g}_{lm}(\mathbf{x}) \tag{3.24}$$

where a^g_{lm} is the extra term from the gaussian bump

$$\begin{aligned} a^g_{lm}(\mathbf{x}) &= \sum_{LM} 4\pi(-i)^L a_0 w^3 \pi^{3/2} \int \frac{\mathrm{d}^3k}{(2\pi)^3}\, e^{i\mathbf{k}\cdot\mathbf{x}} \\ &\quad \times \int \mathrm{d}\hat{\mathbf{n}}\, Y^*_{lm}(\hat{\mathbf{n}}) Y^*_{LM}(\hat{\mathbf{k}}) Y_{LM}(\hat{\mathbf{n}}) \frac{\theta_L(k)}{\zeta(k)} e^{-\mathbf{k}^2 w^2/4} e^{-i\mathbf{k}\cdot\mathbf{x}_c} \end{aligned}$$

Denoting

$$\mathbf{r} = \mathbf{x}_c - \mathbf{x} \tag{3.25}$$

and using the Rayleigh expansion

$$e^{i\mathbf{k}\cdot\mathbf{r}} = 4\pi \sum_{l_1 m_1} i^{l_1} j_{l_1}(kr) Y^*_{l_1 m_1}(\hat{\mathbf{k}}) Y_{l_1 m_1}(\hat{\mathbf{r}}) \tag{3.26}$$

we get

$$\begin{aligned} a^g_{lm}(\mathbf{x}) &= (4\pi)^2 a_0 w^3 \pi^{3/2} \sum_{LM l_1 m_1} (-i)^{L+l_1} \int \frac{\mathrm{d}^3k}{(2\pi)^3} \\ &\quad \times \int \mathrm{d}\hat{\mathbf{n}}\, Y^*_{lm}(\hat{\mathbf{n}}) Y^*_{LM}(\hat{\mathbf{k}}) Y_{LM}(\hat{\mathbf{n}}) \frac{\theta_L(k)}{\zeta(k)} e^{-\mathbf{k}^2 w^2/4} j_{l_1}(kr) Y_{l_1 m_1}(\hat{\mathbf{k}}) Y^*_{l_1 m_1}(\hat{\mathbf{r}}) \\ &= \frac{2}{\pi} a_0 w^3 \pi^{3/2} \sum_{LM l_1 m_1} (-i)^{L+l_1} \int k^2 \mathrm{d}k\, \frac{\theta_L(k)}{\zeta(k)} e^{-k^2 w^2/4} j_{l_1}(kr) Y^*_{l_1 m_1}(\hat{\mathbf{r}}) \\ &\quad \times \delta_{L l_1} \delta_{M m_1} \delta_{L l} \delta_{M m} \end{aligned}$$

$$a^g_{lm}(\mathbf{x}) = \frac{2}{\pi} a_0 w^3 \pi^{3/2} (-1)^l \int k^2 \mathrm{d}k\, e^{-k^2 w^2/4} \frac{\theta_l(k)}{\zeta(k)} j_l(kr) Y^*_{lm}(\hat{\mathbf{r}}) \tag{3.27}$$

The corrections to temperature fluctuations in real space from this gaussian bump take the form

$$\Delta^g_i = \int \mathrm{d}\hat{\mathbf{n}}\, \Theta^g(\hat{\mathbf{n}}) B_i(\hat{\mathbf{n}}) \tag{3.28}$$

where

$$\Theta^g(\hat{\mathbf{n}}, \mathbf{x}) = \sum_{lm} a^g_{lm}(\mathbf{x}) Y_{lm}(\hat{\mathbf{n}}) \tag{3.29}$$

so

$$\Delta^g_i = \sum_{l m l' m'} \int \mathrm{d}\hat{\mathbf{n}}\, a^g_{lm}(\mathbf{x}) Y_{lm}(\hat{\mathbf{n}}) B_{l'} Y_{l'm'}(\hat{\mathbf{n}}_i) Y^*_{l'm'}(\hat{\mathbf{n}})$$

$$
\begin{aligned}
&= \sum_{lm} a^g_{lm}(\mathbf{x}) B_l Y_{lm}(\hat{\mathbf{n}}_i) \\
&= \sum_{lm} B_l Y_{lm}(\hat{\mathbf{n}}_i) \frac{2}{\pi} a_0 w^3 \pi^{3/2} (-1)^l \int k^2 \mathrm{d}k \, e^{-k^2 w^2/4} \frac{\theta_l(k)}{\zeta(k)} j_l(kr) Y^*_{lm}(\hat{\mathbf{r}}) \\
&= \frac{1}{2\pi^2} a_0 w^3 \pi^{3/2} \sum_l (-1)^l (2l+1) B_l P_l(\hat{\mathbf{n}}_i \cdot \hat{\mathbf{r}}) \int k^2 \mathrm{d}k \, e^{-k^2 w^2/4} \frac{\theta_l(k)}{\zeta(k)} j_l(kr)
\end{aligned}
$$

$$
\Delta^g_i = \frac{1}{2\sqrt{\pi}} a_0 \sum_l (-1)^l (2l+1) B_l P_l(\hat{\mathbf{n}}_i \cdot \hat{\mathbf{r}}) F_l(r, w) \tag{3.30}
$$

where

$$
\begin{aligned}
F_l(r, w) &= w^3 \int k^2 \mathrm{d}k \, e^{-k^2 w^2/4} \frac{\theta_l(k)}{\zeta(k)} j_l(kr) \\
&= \int k^2 \mathrm{d}k \, e^{-k^2/4} \frac{\theta_l(k/w)}{\zeta(k/w)} j_l(kr/w)
\end{aligned} \tag{3.31}
$$

does not depend on the direction $\hat{\mathbf{r}}$ or the amplitude a_0.

In this case we again have 5 new parameters - the amplitude a_0, the distance of the center of the bump from us r, the radius of the bump w, and the direction $\hat{\mathbf{r}}$ (2 parameters). We consider only fluctuations on large scales (i.e. big w) so that only the low-l portion of the spectrum is affected. As for the perturbation in one Fourier mode, we fix the standard cosmological parameters to their best fit values[2] and use a fixed covariance matrix. We simply replace Δ_i by $\Delta_i - \Delta^g_i$ before calculating χ^2 (3.21).

We use the publicly available CAMB code [27] for calculating the standard covariance matrix and $\Theta_l(k)/\zeta(k)$, and a modification of the likelihood code provided by WMAP [28, 29, 30] for calculating χ^2. Since our modification affects only the low-l part of the spectrum, we use the low-resolution part of the likelihood code. The sky map used in this code is the smoothed and degraded ILC map with Kp2 mask. This map is in HEALPIX format [38] with resolution 4 (corresponding to $N_{side} = 16$) and has 3072 pixels, of which 2482 are left after the mask. HEALPIX maps describe modes reliably up to $l_{max} \sim 2N_{side}$, so we restrict the sums (3.20) and (3.30) to $l_{max} = 30$. We also exclude $l = 1$ terms since the dipole has already been removed from the data.

3.3 Results

We calculate χ^2 in the space of our new 5 parameters (keeping the standard cosmological parameters fixed to their best fit values) and compare it to the best fit χ^2_{st} for standard cosmology

$$\Delta\chi^2(a_0, b, l, p_1, p_2) = \chi^2(a_0, b, l, p_1, p_2) - \chi^2_{st} \tag{3.32}$$

where b and l are the galactic latitude and longitude of the direction ($\hat{k}_0$ or $\hat{r}_0$), $(p_1, p_2) = (\lambda, \alpha)$ for the fluctuation in one Fourier mode and (r, w) for the gaussian bump,

$$\chi^2_{st} = 2475.3$$

$\Delta\chi^2$ is a quadratic function of a_0

$$\Delta\chi^2 = A(b, l, p_1, p_2)a_0^2 + B(b, l, p_1, p_2)a_0 \tag{3.33}$$

We calculate A and B in the space of the remaining 4 parameters then calculate $\Delta\chi^2$ as a function of the amplitude as well. We use both Pearson's χ^2 test and the maximum likelihood method to put limits on our new parameters.

3.3.1 Semiclassical Fluctuation in One Fourier Mode

As mentioned before, we are assuming that λ is of the order of the size of the observable universe, so we will give λ in terms of the distance to the last scattering surface $L_0 = 14.4Gpc$. In these units we vary λ in the range $[0.7, 2.6]$ with step 0.1. In order to have a uniform distribution of directions $\hat{k}_0$ we vary it on a HEALPIX grid [38] with the same resolution 4 as the sky map, which means that we consider 3072 different directions. We vary the phase α in its full range $[0, 2\pi]$ with step $\pi/10$, and a_0 in the range $[0, 7 \times 10^{-4}]$.

We obtain a best fit value of $\Delta\chi^2 = -12.7$ corresponding to $a_0 = 4.21 \times 10^{-5}$, $\lambda = 1.0$, $b = -66°$, $l = 186°$, $\alpha = 4.71$. Since we have 5 extra parameters, this means that the standard cosmology is compatible with the data at 2.8σ.

We first use a goodness-of-fit test to put an upper bound on the magnitude of perturbation a_0. This test is sensitive to the overall value of χ^2 rather than the

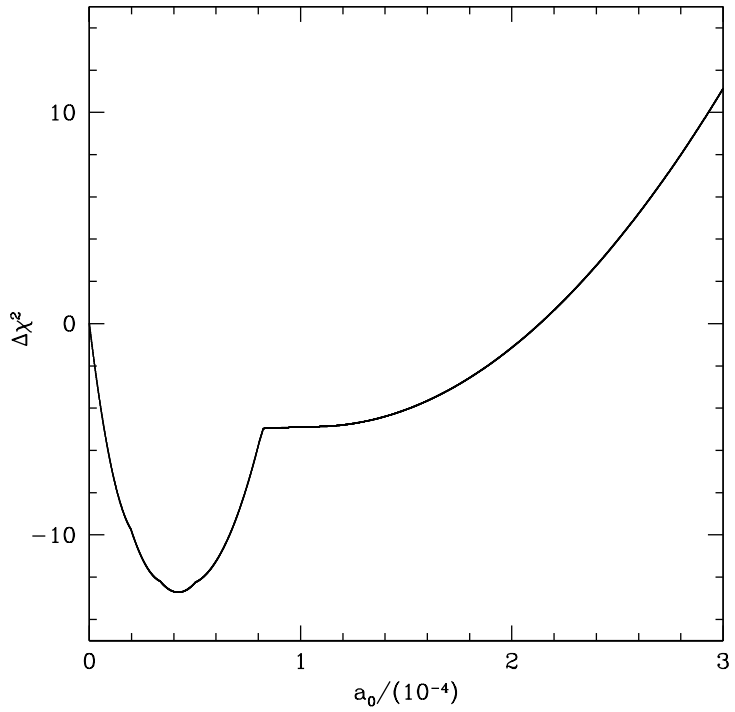

Figure 3.1: Plot of $\Delta\chi^2$ against a_0 for a fluctuation in one Fourier mode, minimized with respect to the other parameters.

Table 3.1: Upper limits on the magnitude a_0 of the fluctuation in one Fourier mode from Pearson's χ^2 test.

C.L.	$a_{0,max}/10^{-4}$
68%	4.07
90%	5.85
95%	6.45

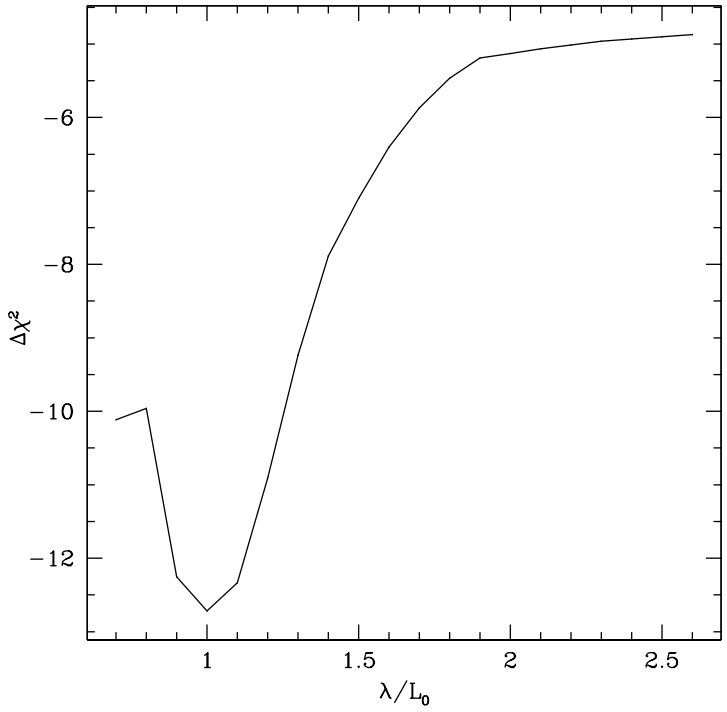

Figure 3.2: Plot of $\Delta\chi^2$ against λ, minimized with respect to the other parameters.

difference. We use Pearson's χ^2 test with 2477 degrees of freedom (2482 pixels, 5 free parameters). $\Delta\chi^2$ as a function of a_0 is shown in Fig. 3.1, where we have minimized with respect to the other 4 parameters. It is smooth, except around the point $a_0 = 7.4 \times 10^{-5}$ where there is a sharp jump from one parabola (3.33) to another, with different values of the other 4 parameters. The bounds obtained from this test are shown in Table 3.1.

Next we use the maximum likelihood method to find confidence regions for all of our newly introduced parameters. This method is sensitive to likelihood ratios only (see [39, §33], and [40, 41] for detailed discussions of the method). Since in this case the covariance matrix is fixed, the likelihood ratio only depends on $\Delta\chi^2$. $\Delta\chi^2$ as a function of λ, minimized with respect to all the other parameters, is shown in Fig. 3.2. The analogous plot for α is shown in Fig. 3.3. The confidence regions for a_0, λ, and α are summarized in Table 3.2.

The dependence of $\Delta\chi^2$ on the direction $\hat{k}_0$ is shown in Fig. 3.4, and the

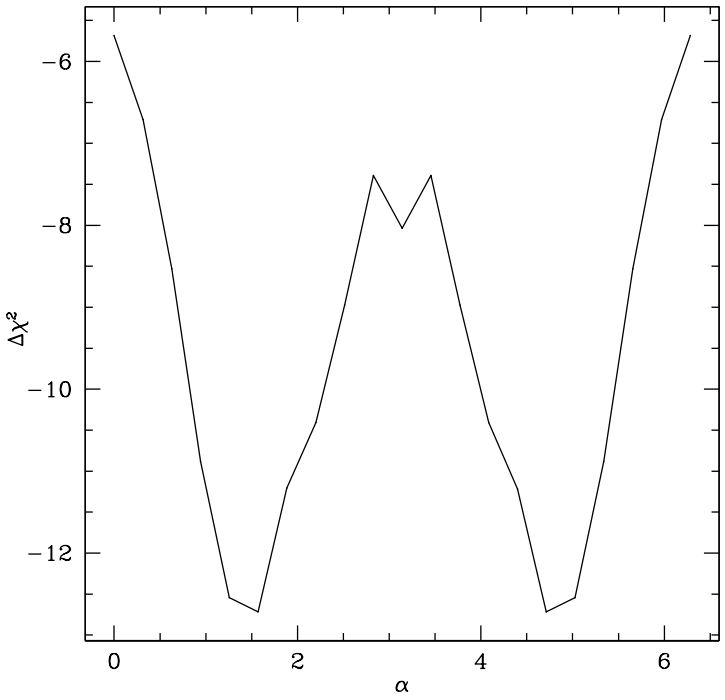

Figure 3.3: Plot of $\Delta\chi^2$ against α, minimized with respect to the other parameters.

Table 3.2: Confidence regions for parameters a_0, λ, and α from the maximum likelihood method.

C.L.	$a_0/10^{-5}$	λ/L_0	α
68.3%	$[2.8, 5.7]$	$[0.9, 1.1]$	$[1.1, 1.8] \cup [4.5, 5.2]$
95.5%	$[1.5, 7.1]$	≤ 1.3	$[0.7, 2.6] \cup [3.7, 5.6]$
99.7%	$[0.5, 15.9]$		$[0, 2\pi]$

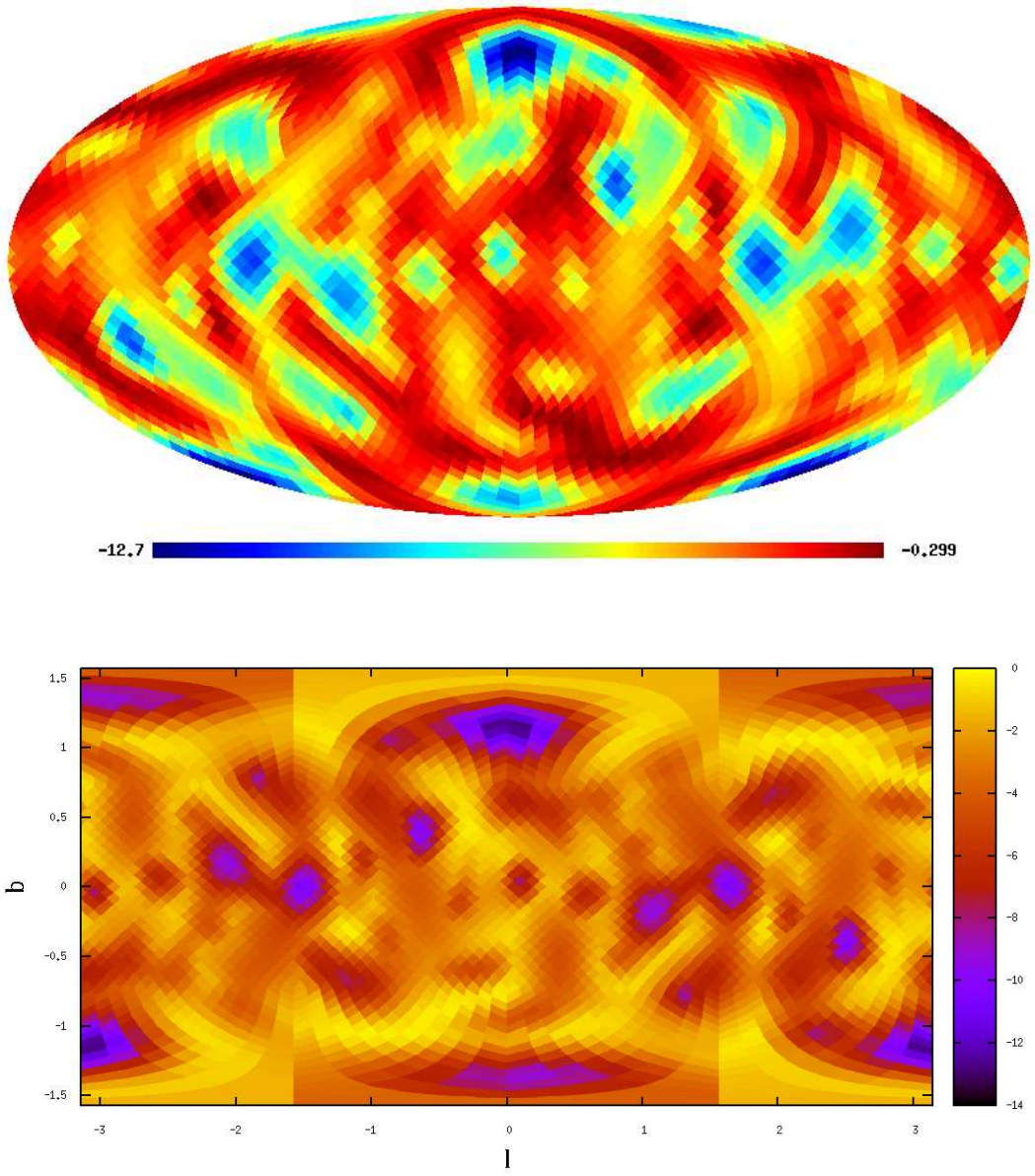

Figure 3.4: Plot of $\Delta\chi^2$ against $\hat{k}^0$, minimized with respect to the other parameters.

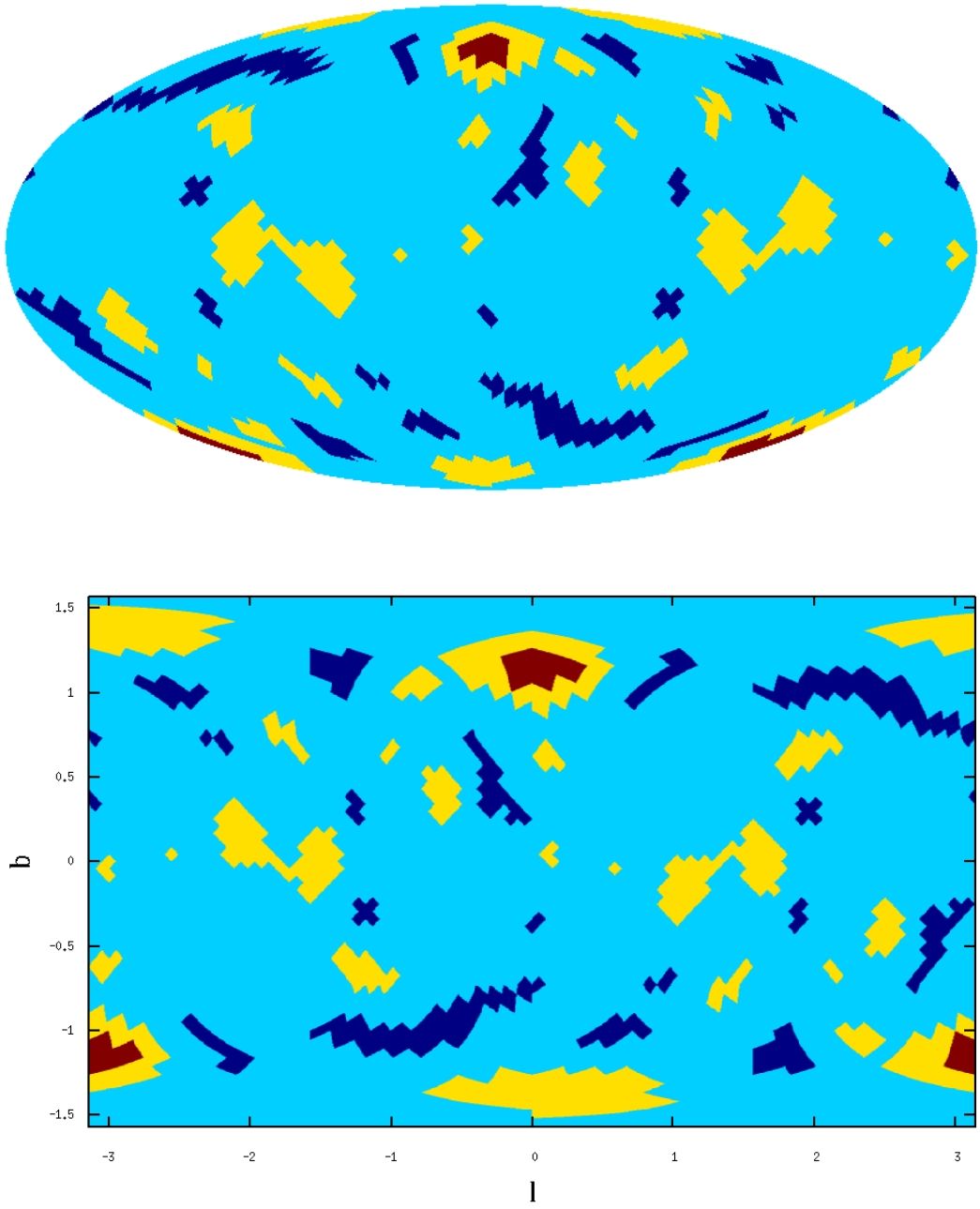

Figure 3.5: 68.3% (red), 95.5% (yellow), and 99.7% (light blue) confidence regions for $\hat{k}_0$.

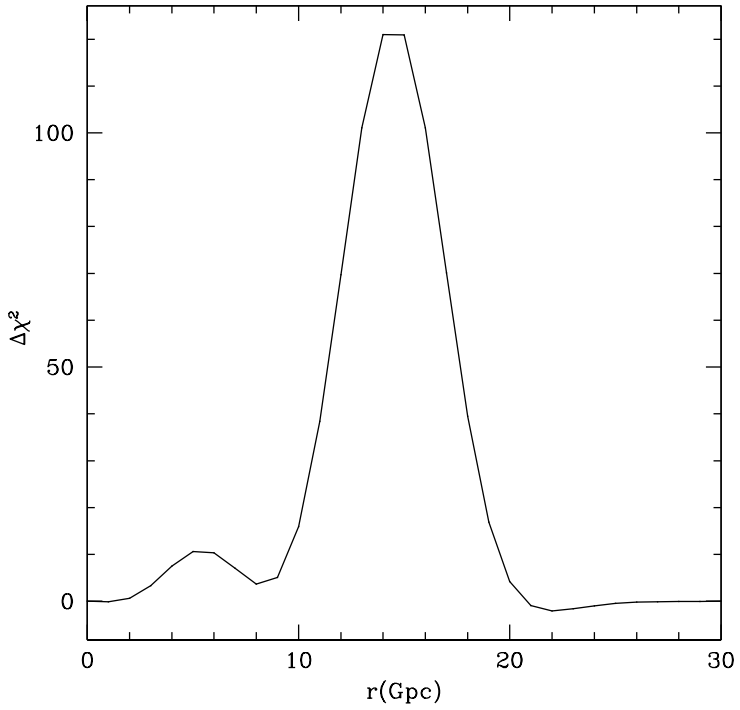

Figure 3.6: Plot of $\Delta\chi^2$ against r for a gaussian fluctuation, with all the other parameters fixed ($w = 5Gpc$, $a_0 = 10^{-3}$).

68.3%, 95.5%, and 99.7% confidence regions in Fig. 3.5. We get $\Delta\chi^2 = -2.58$ for the axis of evil direction $b = 60°$, $l = -100°$. For the best fit direction $b = 34°$, $l = 63°$ found by [43] we get $\Delta\chi^2 = -3.08$. Finally, we consider the best fit direction for a torus topology found in chapter 2, $b = 37°$, $l = 291°$, to get $\Delta\chi^2 = -4.29$. All of these special directions are outside the 95.5% region, which means that a semiclassical fluctuation in one Fourier mode can not mimic these effects.

3.3.2 Semiclassical Gaussian Fluctuation in Space

We again restrict our analysis to fluctuations on large scales, which means that the parameter w needs to be not much smaller than the distance to the last scattering surface $L_0 = 14.4Gpc$. We also need to make sure that the fluctuation has a significant causal contact with the last scattering surface, otherwise it will not have an observable effect on the temperature fluctuations. The other issue to

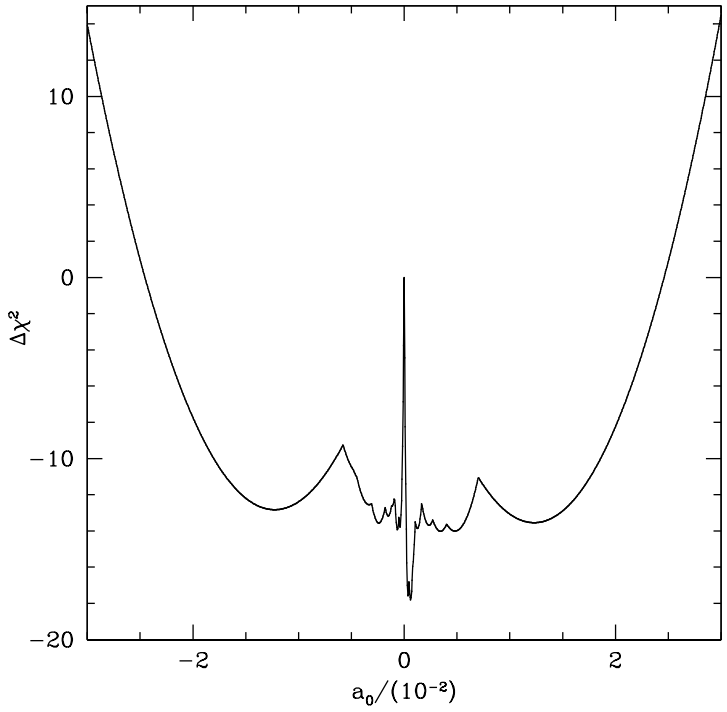

Figure 3.7: Plot of $\Delta\chi^2$ against a_0 for a gaussian fluctuation, minimized with respect to the other parameters.

keep in mind is that if the center of the bump is very close to our position then the corrections to the temperature fluctuations will be nearly constant and will be absorbed into the constant background temperature. The same thing is true if the center is not very close to us but w is very large. As an example, we plot the dependence of $\Delta\chi^2$ on r with all the other parameters fixed in Fig. 3.6. In particular we choose $w = 5\ Gpc$ and $a_0 = 10^{-3}$. As we can see, it is peaked near L_0 and the dependence becomes very week for r outside the range $[9, 20]\ Gpc$, which roughly corresponds to $[L_0 - w, L_0 + w]$. So we will not consider the values of r that are outside that range. This is equivalent to the requirement that the 1σ surface of the gaussian fluctuation must intersect the last scattering surface. We check for four different values of w: 2 Gpc, 3 Gpc, 4 Gpc and 5 Gpc. We vary r with a step of 1 Gpc in the range $[L_0 - w, L_0 + w]$. As in the previous scenario, we vary the direction $\hat{r}$ on a HEALPIX grid with resolution 4, i.e. we consider 3072 different directions. In this case negative amplitudes are not equivalent to positive

Table 3.3: Limits on the magnitude a_0 of the gaussian fluctuation from Pearson's χ^2 test.

C.L.	$a_{0,min}/10^{-2}$	$a_{0,max}/10^{-2}$
68%	−3.56	3.53
90%	−4.75	4.68
95%	−5.16	5.07

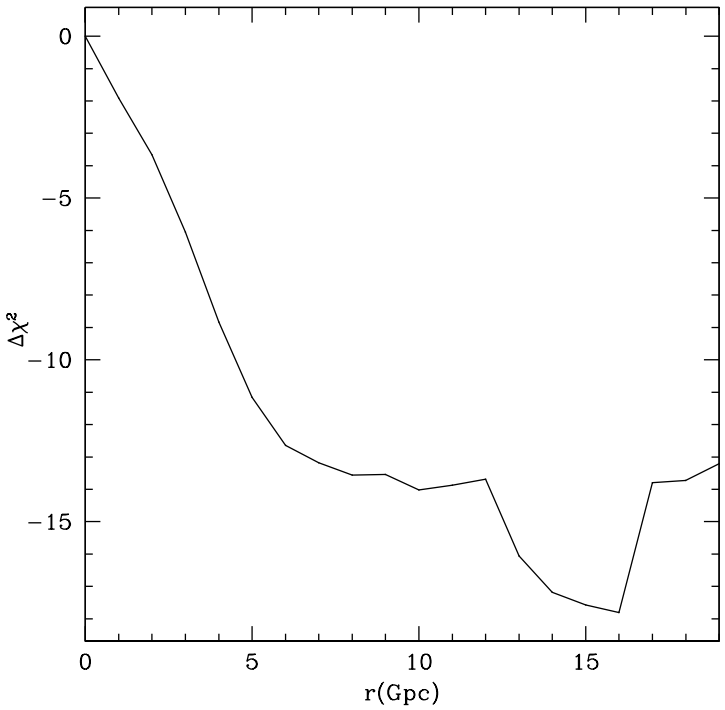

Figure 3.8: Plot of $\Delta\chi^2$ against r, minimized with respect to the other parameters.

Table 3.4: Confidence regions for parameters a_0 and r from the maximum likelihood method.

C.L.	$a_0/10^{-3}$	r (Gpc)
68.3%	$[0.3, 0.7]$	$[13.7, 16.3]$
95.5%	$[-0.7, -0.6] \cup [0.2, 1.3] \cup [3.0, 5.4]$	$[9.5, 17.0]$
99.7%	$[-19.1, -0.1] \cup [0.1, 19.6]$	≥ 4.0

amplitudes, so we vary a_0 in the range $[-6 \times 10^{-2}, 6 \times 10^{-2}]$ (as we will see below, the dependence on the amplitude is weaker in this case).

The best fit value we get in this case is $\Delta\chi^2 = -17.8$ for $a_0 = 6 \times 10^{-4}$, $r = 16Gpc$, $w = 2Gpc$, $b = 57°$, $l = -61°$. We have 5 new parameters, so the standard cosmology is compatible with the data at 3.6σ.

We first impose upper and lower bounds on the amplitude a_0 from a goodness-of-fit test. As for the fluctuation in one Fourier mode, we use Pearson's χ^2 test with 2477 degrees of freedom since there are 2482 pixels and 5 free parameters. The dependence of $\Delta\chi^2$ on a_0 is shown in Fig. 3.7, where $\Delta\chi^2$ is minimized with respect to all the other parameters. The results of this test are summarized in Table 3.3.

Finally, we use the maximum likelihood method to put bounds on all of the new parameters. The dependence of $\Delta\chi^2$ on r is shown in Fig. 3.8, where we have minimized with respect to all the other parameters. The confidence regions for a_0 and r are shown in Table 3.4.

The dependence of $\Delta\chi^2$ on the direction $\hat{r}$ is shown in Fig. 3.9, and the 68.3%, 95.5%, and 99.7% confidence regions in Fig. 3.10. For the axis of evil direction $b = 60°$, $l = -100°$ we get $\Delta\chi^2 = -8.40$. This is within the 99.7% region but outside the 95.5% region. For the best fit direction $b = 34°$, $l = 63°$ for a linearly modulated power spectrum [43] we get $\Delta\chi^2 = -3.99$. This is outside the 99.7% region. There is a slight indication that the axis of evil might be a result

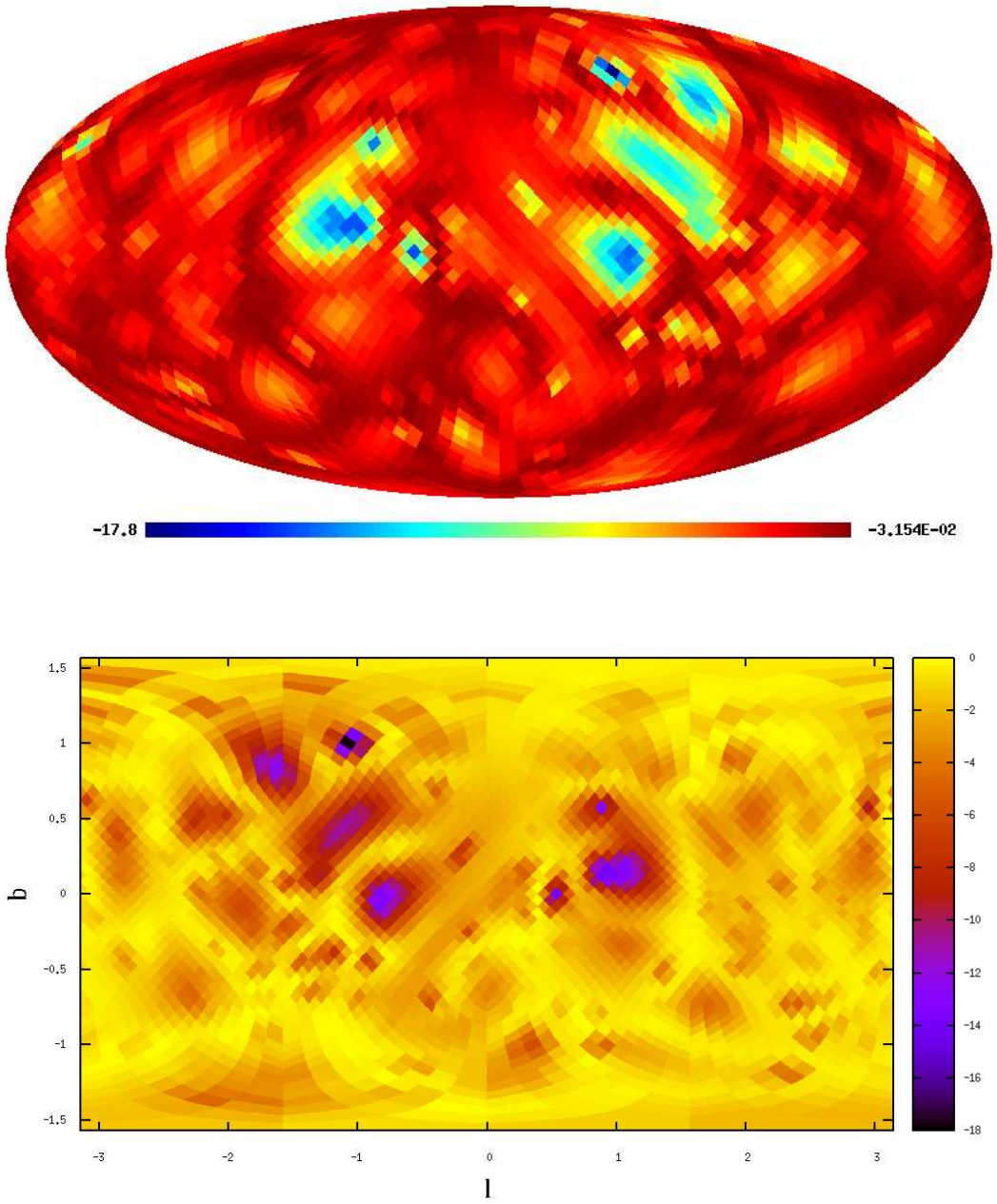

Figure 3.9: Plot of $\Delta\chi^2$ against $\hat{r}$, minimized with respect to the other parameters.

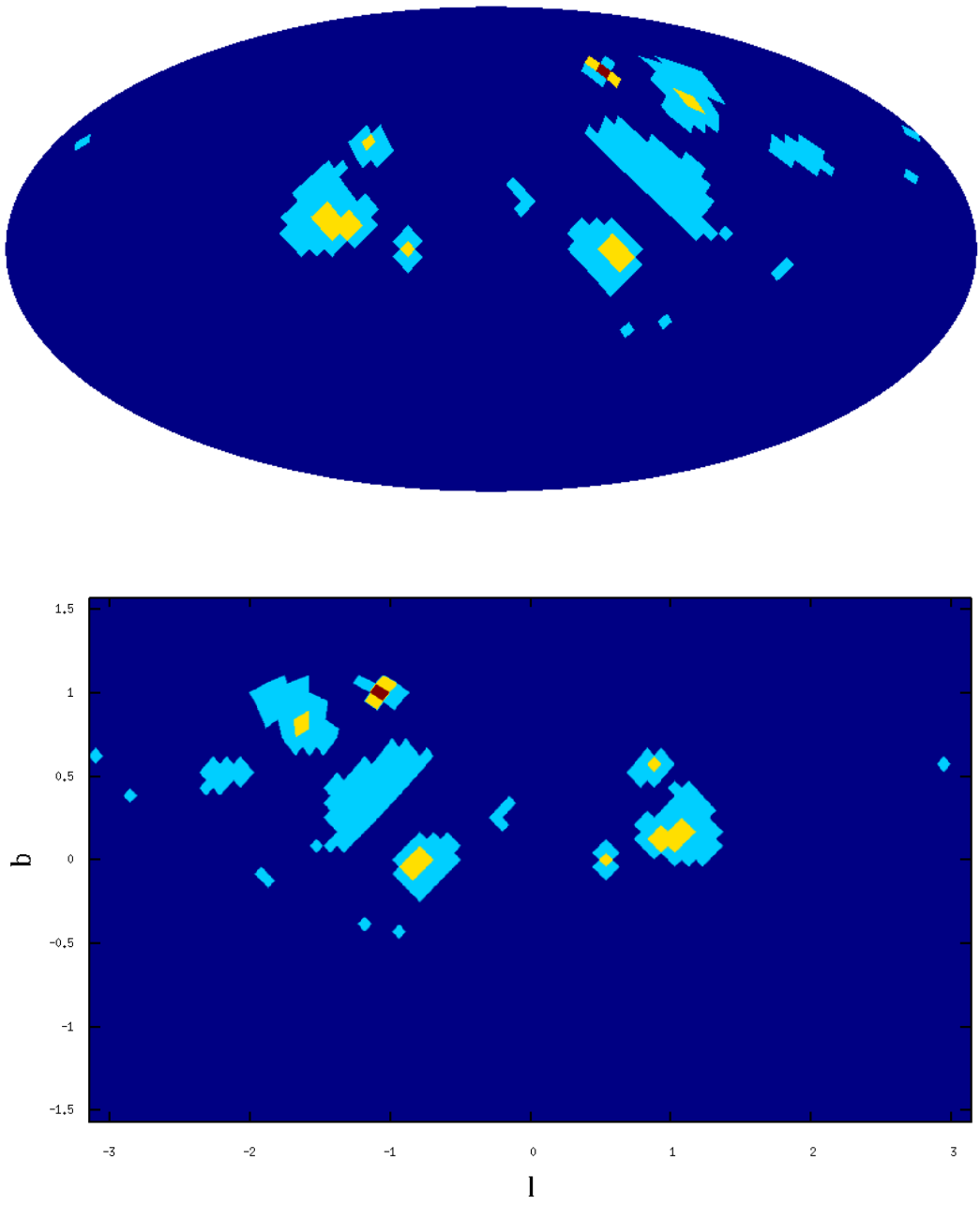

Figure 3.10: 68.3% (red), 95.5% (yellow), and 99.7% (light blue) confidence regions for $\hat{r}$.

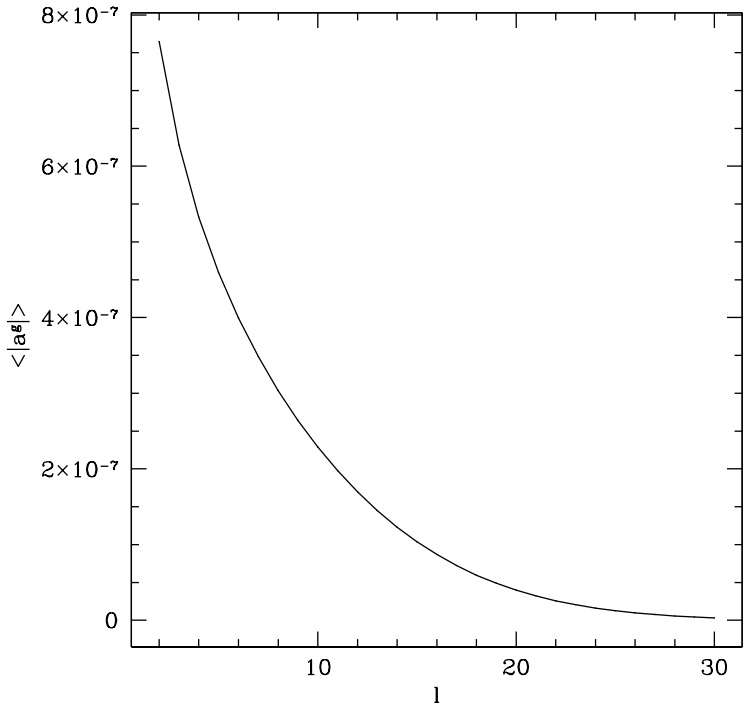

Figure 3.11: Plot of $\langle|a^g|\rangle$ against l for a gaussian fluctuation in units of the CMB temperature $2.73K$.

of a semiclassical gaussian fluctuation in space. However, the signal we see is far from the 5σ criterion to be claimed as a detection.

3.4 Checks

We first want to check that cutting off at $l_{max} = 30$ does not have a significant effect on our results for the scales we consider. For the fluctuation in one Fourier mode the $l = 15$ terms in (3.18) are already 3 orders of magnitude smaller than the $l = 2$ terms for the wavelengths λ under consideration. This means that the effect of the cutoff can be completely neglected. For the gaussian bump the decay with l is not as fast. In Fig. 3.11 we plot the dependence of

$$\langle|a^g|\rangle \equiv \frac{1}{2l+1}\sum_{m=-l}^{l}|a^g_{lm}| \tag{3.34}$$

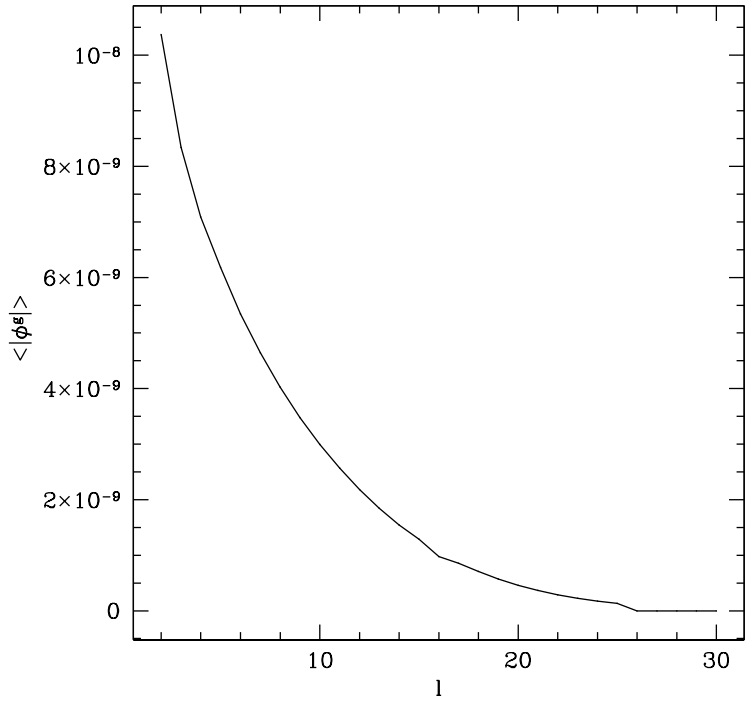

Figure 3.12: Plot of $\langle|\phi^g|\rangle$ against l for a gaussian fluctuation.

on l for the smallest scale $w = 2\ Gpc$ we consider with a typical amplitude of $a_0 = 10^{-3}$ (all the other parameters are also fixed). The $l = 30$ term is 2 orders of magnitude smaller than the $l = 2$ term, therefore the cutoff cannot have a significant effect in this case either.

The cosmic microwave background radiation gets lensed by the large scale structure before we observe it. Any semiclassical fluctuation in primordial perturbations translates to a fluctuation in large scale structure as well, therefore it contributes to the lensing of photons. We discuss the effects of lensing in Appendix B. Lensing is described by the lensing potential ϕ. The correction in temperature anisotropies from lensing in harmonic space is given by (B.6)

$$\delta a_{lm} = \sum_{LM} \sum_{l'm'} \phi_{LM} \tilde{a}_{l'm'} I_{l\ L\ l'}^{m\ M\ m'} \tag{3.35}$$

where $\tilde{a}_{lm}$ denotes the unlensed anisotropies. The lensing potential itself from the semiclassical fluctuations is proportional to the amplitude a_0, so is $\tilde{a}_{l'm'}$, which

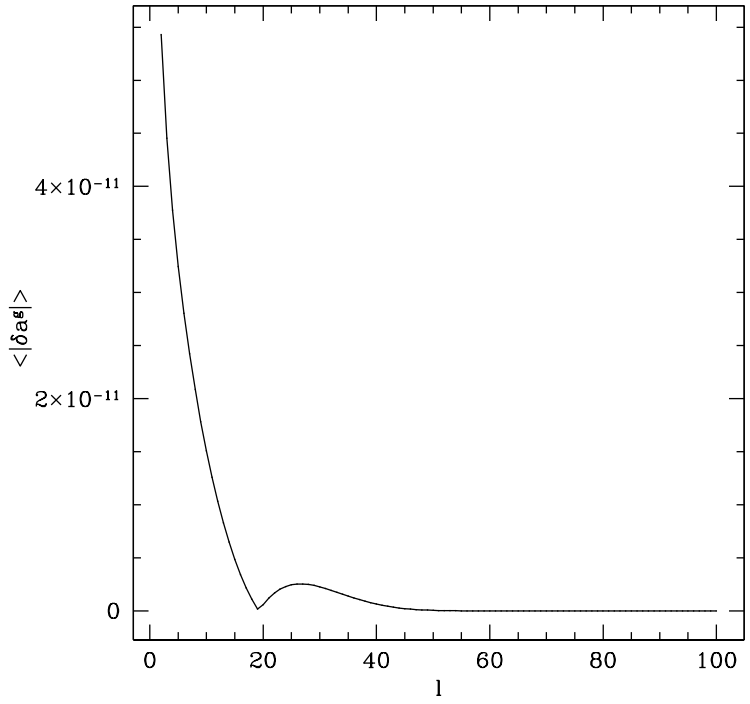

Figure 3.13: Plot of $\langle|\delta a^g|\rangle$ against l for a gaussian fluctuation in units of the CMB temperature $2.73K$.

means that the correction from lensing is proportional to a_0^2. Since the highest bounds we obtain for a_0 are of the order of 10^{-2} the lensing effects can be completely neglected, as is done in our analysis. As an example we calculate the lensing potential for a typical case $a_0 = 10^{-3}$ (the same as in Fig. 3.11) and plot it in Fig. 3.12 (here again we plot the average of $|\phi_{lm}|$ as in equation (3.34)). The correction to temperature fluctuations from lensing effects is shown in Fig. 3.13. As we can see, the correction from lensing is 4 orders of magnitude smaller than the semiclassical fluctuations (compare with Fig. 3.11), meaning that the lensing effect can be safely ignored.

3.5 Conclusions

For a semiclassical fluctuation in one Fourier mode we get an improvement in χ^2 of 12.7 for 5 extra parameters, corresponding to 2.8σ. The best fit direction

that we find does not coincide with any known special direction. In particular, the axis of evil can not be explained by a semiclassical fluctuation in one mode with large wavelength. Also, we find no indication of a fluctuation in a mode in the direction of the torus axis obtained in chapter 2, so it is unlikely that the torus signal is an artifact of a semiclassical fluctuation in one mode.

A semiclassical gaussian fluctuation in space gives a better fit to the data. The improvement in χ^2 is 17.8 for 5 extra parameters, corresponding to 3.6σ. The best fit direction towards the center of the fluctuation does not coincide with the axis of evil. For the axis of evil direction we find an improvement of 8.4 in χ^2, which gives a slight indication that the axis of evil can be due to a semiclassical gaussian bump in space. However, the improvement is not big enough to claim a detection.

Overall, our results show that it is unlikely that the scenarios we consider for breaking the isotropy of space can explain the previously suggested possible deviations from isotropy. Note, however, that a torus topology implies periodicity in all the directions, not just the axes of the torus. And we have considered a fluctuation in one single mode only and found an improvement corresponding to 2.8σ. Further investigation with more than one mode, perhaps an infinite spectrum of modes, would be of interest and could possibly give an alternative explanation to the torus topology signal. One scenario discussed in literature that modifies the primordial power spectrum of fluctuations is modifications of Bunch-Davies vacuum (see, e.g. [44, 45]). Our results imply that considering a non-isotropic vacuum state for inflation could be of interest. Multi-field inflationary models may also generate non-isotropic perturbations [46].

Chapter 3, in part is currently being prepared for submission for publication of the material. Aslanyan, Grigor; Manohar, Aneesh, V. The dissertation author was the primary investigator and author of this material.

Chapter 4

Summary

Firstly, we considered the possibility that the universe is not infinite. We studied flat topologies compactified in three, two, or one dimensions. The experimental data fits the model with two compactified dimensions the best. Infinite universe is compatible with the data only at 4.3σ level. Although we did not obtain the standard 5σ criterion to claim a discovery, we found a surprisingly high signal for a finite topology. The maximum likelihood 95% intervals for the size L of the compactified dimensions are $1.7 \leq L/L_0 \leq 2.1$, $1.8 \leq L/L_0 \leq 2.0$, $1.2 \leq L/L_0 \leq 2.1$ for the three cases, respectively, in terms of the distance to the last scattering surface $L_0 = 14.4\ Gpc$. The 95% bounds obtained from Pearson's χ^2 test are $L/L_0 \geq 1.27, 0.97, 0.57$ for the three cases, respectively.

Next, we considered semiclassical fluctuations of primordial perturbations on large scales. We analyzed two possibilities - a fluctuation in one Fourier mode and a gaussian fluctuation in space. Both of these possibilities fit the data better than the standard primordial perturbations, but we find no strong evidence. The 95% confidence intervals for the amplitude a_0 of these fluctuations from the maximum likelihood method are $|a_0| \in [1.5 \times 10^{-5}, 7.1 \times 10^{-5}]$ and $a_0 \in [-0.7 \times 10^{-3}, -0.6 \times 10^{-3}] \cup [0.2 \times 10^{-3}, 1.3 \times 10^{-3}] \cup [3.0 \times 10^{-3}, 5.4 \times 10^{-3}]$ for the two cases, respectively. Pearson's χ^2 test gives the bounds $|a_0| \leq 6.45 \times 10^{-4}$ and $-5.16 \times 10^{-2} \leq a_0 \leq 5.07 \times 10^{-2}$ for the two cases, respectively, at 95% confidence level.

All of the models we discussed break the isotropy of space, but none of

them gives an explanation to the axis of evil.

We have performed multiple checks to make sure that the better fits we obtain are not artifacts of some other effects. Although we find no such evidence, further checks of the data are important.

Our results indicate that it is of interest to further study the scenarios we consider. It is very important to verify our findings about the finite topology of space with some independent data. The polarization data from the Planck satellite to be released soon is a good candidate. The simple semiclassical modifications of primordial perturbations we considered fit the data better, which means that studies of more complex scenarios are in order. In particular, fluctuations in more than one Fourier mode can be generated, in multi-field models of inflation for example, and their analysis can be of interest.

Appendix A

The Standard Cosmological Model and Inflation

The standard big-bang cosmology is extremely successful in describing the evolution of the universe from at least the epoch of the synthesis of light elements until now. Observational data has strongly confirmed the predictions of this model, and we have seen no disagreements between the theory and the observations so far. However, there is a number of fundamental cosmological problems for which the model has no explanations. Inflationary theory, which is an extension to the standard cosmology, has been proposed to address these difficulties of the model. While being remarkably successful in solving the fundamental problems of standard cosmology, it also provides a natural way of explaining the anisotropies of the cosmic microwave background and the large-scale structure (stars, galaxies, clusters of galaxies, etc.) of the universe. In this appendix we briefly discuss the standard model of cosmology and the basics of the theory of inflation.

We will use the "God-given" units $\hbar = c = 1$. It is also convenient to use the reduced Planck mass $M_{pl} = (8\pi G)^{-1/2} \approx 2.436 \times 10^{18} GeV \approx 4.342 \times 10^{-6} g$ instead of the gravitational constant G.

A.1 The Standard Model of Cosmology

In this section we will give a very brief introduction to the standard big-bang cosmology (for extensive discussion of the model see e.g., [50] [51]).

On large scales the observable universe is homogeneous and isotropic (cosmological principle). Even when considering the small-scale highly inhomogeneous structure of the universe (such as stars and galaxies) it is convenient to assume a homogeneous and isotropic background metric and impose the small-scale inhomogeneities as small perturbations. The background is described by the maximally-symmetric **Friedmann-Robertson-Walker** metric:

$$ds^2 = -dt^2 + a^2(t)\left(\frac{dr^2}{1-Kr^2} + r^2\left(d\theta^2 + \sin^2\theta d\phi^2\right)\right) \tag{A.1}$$

where (t, r, θ, ϕ) are the **comoving coordinates** (t being the **cosmic time**), K is the **spatial curvature**, $a(t)$ is the **cosmic scale factor**. It is convenient to rewrite the metric in the form:

$$ds^2 = -dt^2 + a^2(t)\left(d\chi^2 + F^2(\chi)\left(d\theta^2 + \sin^2\theta d\phi^2\right)\right) \tag{A.2}$$

where

$$F(\chi) \equiv \begin{cases} \sinh\chi & K = -1 \\ \chi & K = 0 \\ \sin\chi & K = +1 \end{cases} \tag{A.3}$$

The energy-momentum-stress tensor is that of a homogeneous and isotropic fluid in the rest frame. It is diagonal with equal spatial components:

$$T^\mu_\nu = \begin{pmatrix} -\rho & & & \\ & p & & \\ & & p & \\ & & & p \end{pmatrix} \tag{A.4}$$

where ρ is the density and p is the pressure of the fluid, which depend only on time. To find the time dependence of the scale factor and the energy-momentum-stress tensor, we must solve the Einstein field equations in General Relativity (see e.g., [52]):

$$G_{\mu\nu} \equiv R_{\mu\nu} - \frac{1}{2}g_{\mu\nu}R = \frac{T_{\mu\nu}}{M_{pl}^2} \tag{A.5}$$

The $0-0$ component of (A.5) gives the **Friedmann equation**:

$$H^2 = \frac{\rho}{3M_{pl}^2} - \frac{KM_{pl}^2}{a^2} \tag{A.6}$$

while the conservation of the energy-momentum-stress tensor ${T^{\mu\nu}}_{;\nu} = 0$ gives the **continuity equation**:

$$\dot{\rho} + 3H(\rho + p) = 0 \tag{A.7}$$

Here $H \equiv \dot{a}/a$ is the **Hubble parameter**. Combining (A.6) and (A.7) we can get an equation for the acceleration $\ddot{a}$:

$$\frac{\ddot{a}}{a} = -\frac{\rho + 3p}{6M_{pl}^2} \tag{A.8}$$

which may also be obtained from the $i-i$ component of (A.5).

To solve the equations (A.6), (A.7) we need the relation between ρ and p (the equation of state). Of interest are the following cases:

1. Particles at rest (called **matter** hereafter):

$$p = 0 \tag{A.9}$$

2. Radiation and ultra-relativistic particles (called **radiation** hereafter):

$$p = \frac{1}{3}\rho \tag{A.10}$$

3. Vacuum energy (also referred to as the **cosmological constant**):

$$p = -\rho \tag{A.11}$$

We can easily solve (A.7) for these cases to get for matter:

$$\rho \propto a^{-3} \tag{A.12}$$

For radiation:

$$\rho \propto a^{-4} \tag{A.13}$$

And for vacuum energy:

$$\rho = const \tag{A.14}$$

The universe contains all the three types of energy mentioned above. It is convenient to introduce unitless **density parameters** as follows:

$$\Omega_i = \rho_i/\rho_c \tag{A.15}$$

where

$$\rho_c = 3H^2 M_{pl}^2 \tag{A.16}$$

is the so-called **critical density** (the density of the universe with 0 spatial curvature) and the index i may denote matter (M), radiation (R), or vacuum energy (Λ). We also introduce a "curvature density parameter":

$$\Omega_K = -\frac{K M_{pl}^2}{a^2 H^2} \tag{A.17}$$

Then the Friedmann equation (A.6) may be written in the form:

$$\Omega_\Lambda + \Omega_M + \Omega_R + \Omega_K = 1 \tag{A.18}$$

Using (A.12), (A.13), (A.14), we can rewrite the Friedmann equation (A.6) in the form:

$$\left(\frac{H}{H_0}\right)^2 = \Omega_{\Lambda,0} + \Omega_{M,0}\left(\frac{a_0}{a}\right)^3 + \Omega_{R,0}\left(\frac{a_0}{a}\right)^4 + \Omega_{K,0}\left(\frac{a_0}{a}\right)^2 \tag{A.19}$$

where the subscript 0 denotes the values at the present epoch. From (A.19) it is clear that at an earlier epoch, when a is sufficiently small, matter density dominates (**matter domination epoch**), and all the other terms can be neglected. In this case the solution can be simply written:

$$a \propto t^{2/3} \tag{A.20}$$

Although the radiation density is negligibly small at the present time, because of a^{-4} dependence it is dominant at even earlier times than the matter domination (**radiation domination epoch**), and in this case the solution becomes:

$$a \propto t^{1/2} \tag{A.21}$$

As we will see below, of crucial importance to the inflationary theory is the case when vacuum energy dominates the universe, with the solution:

$$a \propto e^{Ht} \tag{A.22}$$

where $H = const.$

Often it is convenient to use the **conformal time** η instead of the cosmic time t, defined by:

$$dt = a(\eta)d\eta \tag{A.23}$$

in terms of which the metric (A.2) can be written in the form:

$$ds^2 = a^2(\eta)\left(-d\eta^2 + d\chi^2 + F^2(\chi)\left(d\theta^2 + \sin^2\theta d\phi^2\right)\right) \tag{A.24}$$

The solutions (A.20)-(A.22) can be rewritten in terms of the conformal time as follows. For matter domination epoch we get:

$$a \propto \eta^2 \tag{A.25}$$

For radiation domination:

$$a \propto \eta \tag{A.26}$$

And finally, for vacuum energy domination:

$$a \propto -\eta^{-1} \tag{A.27}$$

Note that for matter and radiation domination we chose $\eta \to 0$ when $a \to 0$ and $\eta \to \infty$ when $a \to \infty$, but for vacuum energy domination we have $\eta \to -\infty$ when $a \to 0$ and $\eta \to 0$ when $a \to \infty$.

Let us now introduce the concepts of **particle** and **event horizons**. The horizons are defined for a given time η and a given **comoving observer**, i.e. a point with fixed comoving spatial coordinates, which we will choose to be the origin for convenience. The particle horizon is defined for a given initial time η_i (which is usually chosen to be 0 for the standard cosmology since that is the point of singularity) to be the set of comoving points from which a light signal could reach

the given point from time η_i (or later) until time η. Since for light signals we have $ds = 0$, from (A.24) we immediately get the radius of the particle horizon:

$$\chi_p(\eta) = \eta - \eta_i \tag{A.28}$$

The event horizon is defined in a similar way, but now it is for a given final time η_f (usually chosen to be infinity for standard cosmology) and is the set of comoving points to which a light signal can travel from time η until time η_f (or earlier). The radius of the event horizon is:

$$\chi_e(\eta) = \eta_f - \eta \tag{A.29}$$

Note that for matter and radiation domination there is a finite particle horizon but an infinite event horizon, however for vacuum energy domination there is an infinite particle horizon but a finite event horizon.

Another useful way of characterizing time is the **redshift** of light that has been emitted at the given time and is being observed today. Because of the expansion of the universe the wavelength of light also changes in the same way as all the other physical distances, and the redshift z is defined by the relation:

$$1 + z = \frac{\lambda_{obs}}{\lambda_{emit}} = \frac{a(t_0)}{a(t)} \tag{A.30}$$

For some of the measurements it is convenient to deal with some other notions of distance. Suppose we are observing a star of known intrinsic luminosity L and we want to determine the distance to that star by the measured flux f. The **luminosity distance** d_L is defined by the relation:

$$f = \frac{L}{4\pi d_L^2} \tag{A.31}$$

To find the relation between d_L and the comoving distance let us assume that the star is at the origin of coordinates and we are a comoving distance χ away. Assuming that the current value of the cosmic scale factor is 1 we can calculate the surface area of a sphere centered at the star and passing through our position χ from the metric (A.2) to be

$$A = 4\pi F^2(\chi)$$

Then the total energy of photons that passes through that sphere in time dt is

$$E = fAdt$$

But that energy is not the energy emitted by the star in time dt since the rate at which the photons arrive is lower than the rate at which they were emitted by the redshift factor $(1+z)$. Also, the energy of each photon is redshifted by the same factor, so the energy E is related to the luminosity L by

$$E = \frac{Ldt}{(1+z)^2}$$

Collecting everything together, we get

$$d_L = (1+z)F(\chi) \tag{A.32}$$

Now suppose we are looking at a star of known physical size l and we measure the small angle subtended by it to be θ. We define the **angular diameter distance** d_A by the relation:

$$\theta = \frac{l}{d_A} \tag{A.33}$$

From the metric (A.2) we can calculate the physical circumference of a circle around our position (assumed to be the origin of coordinates) at the time of emission. Assuming that the comoving distance to the star is χ we get:

$$L = 2\pi a(t)F(\chi) = \frac{2\pi F(\chi)}{(1+z)}$$

Then the angle subtended by an object of physical size l is given by:

$$\theta = 2\pi\frac{l}{L} = \frac{(1+z)l}{f(\chi)}$$

So the angular diameter distance is

$$d_A = \frac{F(\chi)}{(1+z)} = \frac{d_L}{(1+z)^2} \tag{A.34}$$

Let us now turn to the currently observed values of cosmological parameters. The matter part of the universe consists of **baryons** and **cold dark matter**, we will define their density parameters to be Ω_B and Ω_C respectively, so that

$\Omega_M = \Omega_B + \Omega_C$. The radiation part of the universe at the epoch of matter-radiation equality (i.e. when $\Omega_M = \Omega_R$) consisted of photons and relativistic neutrinos (at later times the neutrinos might have become non-relativistic, but it is of not much importance since their contribution to the energy density of the universe becomes negligible shortly after matter-radiation equality). The observed values of the parameters by combining WMAP7+BAO+H_0 [30] are as follows

$$\begin{aligned} \Omega_{B,0} &= 0.0456 \pm 0.00163 \\ \Omega_{C,0} &= 0.227 \pm 0.014 \\ \Omega_\Lambda &= 0.728^{+0.015}_{-0.016} \\ H_0 &= 70.4^{+1.3}_{-1.4} km/s/Mpc \\ T_{cmb} &= 2.725K \\ z_{eq} &= 3209^{+85}_{-89} \end{aligned} \tag{A.35}$$

where T_{cmb} is the temperature of the cosmic microwave background radiation, i.e. photons measured today, and z_{eq} is the redshift of matter-radiation equality.

A.2 Shortcomings of the Standard Big-Bang Cosmology

A.2.1 Horizon Problem

The cosmic microwave background radiation was emitted at about redshift of 1100 [1] and has been traveling to us freely since then, so it effectively gives a snapshot of the universe at that time. One important feature of the CMB is that it is extremely homogeneous all across the sky (the anisotropies are about 5 orders of magnitude smaller than the background)! However, as we saw earlier, the particle horizon grows with time during radiation and matter domination epochs, so it was smaller at the time CMB was emitted. The conformal time (which is equal to the comoving size of the particle horizon) corresponding to the emission of CMB (which is called the **last scattering surface** or **LSS** since after that time

photons undergo no scatterings) is given by:

$$\eta_{LSS} = \int_0^{t_{LSS}} \frac{dt}{a(t)} \tag{A.36}$$

while the comoving distance to LSS is given by:

$$\chi_{LSS} = \int_{t_{LSS}}^{t_0} \frac{dt}{a(t)} \tag{A.37}$$

The scale factor a(t) can be found by integrating eq. (A.19). If we use the values of the parameters in (A.35) we find the current age of the universe, $t_0 = 13.75Gyr$, and the time of last scattering, $t_{LSS} = 371000yr$. Assuming flat universe, which is in good agreement with (A.35) we can find the angle that the particle horizon at the time of CMB emission currently subtends on the sky:

$$\theta_{LSS} = \frac{\eta_{LSS}}{\chi_{LSS}} = 1.15^\circ \tag{A.38}$$

meaning that cmb photons coming from wider separation of angles have never been in causal contact before. The question then naturally arises, how did the CMB become so homogeneous?

A.2.2 Flatness Problem

Consider

$$\Omega = \Omega_M + \Omega_\Lambda + \Omega_R \tag{A.39}$$

We can rewrite the Friedmann equation (A.18) in the form:

$$\Omega - 1 = \frac{KM_{pl}^2}{a^2H^2} \tag{A.40}$$

Now, if $a(t) \propto t^n$ with $n < 1$ (which is the case for both matter and radiation domination epochs) $a^2H^2 \equiv \dot{a}^2 \propto t^{2(n-1)}$ decreases, hence Ω shifts away from 1 with time. However, the present value of Ω is very close to 1, $|\Omega_0 - 1| \lesssim 10^{-2}$, which means that Ω has to be extremely close to 1 at earlier epochs. For example, at the time of **big bang nucleosynthesis** (or **BBN**), which was about 3 minutes after big bang, we must have $|\Omega_{BBN} - 1| \lesssim 10^{-16}$ (BBN is the earliest epoch that has been very well tested observationally), at the GUT scale the accuracy becomes

$|\Omega_{GUT} - 1| \lesssim 10^{-54}$, while at the Planck scale (the scale at which quantum effects of gravity become important) we get $|\Omega_{pl} - 1| \lesssim 10^{-60}$. In differential geometry a flat manifold is just one point in the continuum of different curvatures, i.e. there is nothing special about it, so that extreme fine tuning of the density parameter requires explanation.

A.3 Inflation

A.3.1 Inflation in the Abstract, the Solution of the Cosmological Problems

By definition, **inflation** is an epoch during which the universe expands with acceleration:

$$\ddot{a} > 0 \tag{A.41}$$

which is, of course, equivalent to increasing a^2H^2. If inflation happens at some earlier time and lasts sufficiently long then it can solve the above mentioned problems of standard cosmology. Since BBN has been tested observationally, inflation must have happened (if at all) before that time. Furthermore, the energy scale of BBN is of the order of $0.1MeV$, while accelerators have tested physics to the energy scale of about $1TeV$, so inflation must have happened before that energy scale. The typical models suggest that inflation happened at around GUT scale.

Let us analyze the problems quantitatively.

1. Horizon problem

   Let us assume exponential expansion during inflation (the expansion must be very close to exponential to be in agreement with the observed CMB anisotropies) and that immediately after the end of inflation the universe enters radiation domination. Let inflation start at t_{beg} and end at t_{end}, and during that time $a(t) = a_1 e^{HT}$. Since the hubble parameter is related to the energy density of the universe by Friedmann equation and the energy density changes continuously, the hubble parameter during inflation (constant during that time) must be the same after entering radiation domination. To solve

the horizon problem we need the comoving particle horizon at the time of CMB (t_{LSS}) since the beginning of inflation to be at least the comoving size of the current observable universe (or, more precisely, the radius of LSS, but it is very close to the size of the universe as we saw above). So we need

$$\chi_{LSS} \leq \int_{t_{beg}}^{t_{end}} \frac{dt}{a(t)} + \int_{t_{end}}^{t_{LSS}} \frac{dt}{a(t)} \tag{A.42}$$

However,

$$\int_{t_{end}}^{t_{LSS}} \frac{dt}{a(t)} \leq \int_{0}^{t_{LSS}} \frac{dt}{a(t)} = \eta_{LSS}$$

which is much less than χ_{LSS}, as we saw above. So we can neglect the second tem in (A.42) to get:

$$\chi_{LSS} \leq \int_{t_{beg}}^{t_{end}} \frac{dt}{a_1 e^{Ht}} = \frac{1}{H}\left(\frac{1}{a_{beg}} - \frac{1}{a_{end}}\right)$$

But $a_{end} \gg a_{beg}$ (as we will see shortly), so we can neglect the second term to get:

$$\chi_{LSS} \leq \frac{1}{H a_{beg}} = \frac{1}{H a_{end}} \frac{a_{end}}{a_{beg}}$$

We define the number of e-folds during inflation to be:

$$N = \ln(a_{end}/a_{beg}) \tag{A.43}$$

and we get from above:

$$N \geq \ln(H a_{end} \chi_{LSS}) \tag{A.44}$$

Assuming that inflation happens at GUT scale we get $N \geq 60$. Even if we assumed that inflation happened at TeV scale we would get $N \geq 30$. The unrealistic assumption that inflation happened right before BBN would give $N \geq 16$. So even under very strict conditions on inflation, we need many orders of magnitude of expansion during inflation to explain the horizon problem. That is why a close to exponential expansion is needed with vacuum energy domination.

2. Flatness problem

   Assuming that at the beginning of inflation $|\Omega-1| \sim 1$ and using the numbers from subsection A.2.2 we get for inflation happening at GUT scale $N \geq 62$, while for inflation ending right before BBN $N \geq 18$. So again, a similar number of e-folds is necessary to explain the flatness problem.

As we saw above, a large number of e-folds is needed to solve the problems of the standard cosmology. So during inflation the universe must be very close to vacuum energy domination and should change slowly to make sure that inflation lasts long enough. To quantitatively describe the "slowness" of inflation we introduce the dimensionless **slow-roll parameters** ϵ and η (not to be confused with the conformal time!):

$$\epsilon \equiv -\frac{\dot{H}}{H^2} \tag{A.45}$$

$$\eta \equiv \frac{d\epsilon}{dN} = \frac{\dot{\epsilon}}{H\epsilon} \tag{A.46}$$

where

$$dN \equiv Hdt$$

By definition of inflation, it will end as soon as ϵ equals to 1. In order to get long enough slow-roll inflation we need $\epsilon \ll 1$ and we also need it to change slowly so that it does not become 1 very early, that is the reason why we introduced the second parameter η which we also need to stay much smaller than 1. These parameters play an important role in the calculation of CMB anisotropies, and in order to be in agreement with observations we do need these parameters to be very small!

A.3.2 The Simplest Model of Inflation

The simplest way to physically realize the conditions needed for inflation is through a single scalar field. The action of such a field, minimally coupled to gravity is

$$S = S_{EH} + S_\phi = \int d^4x\sqrt{-g}\left[\frac{M_{pl}^2}{2}R - \frac{1}{2}g^{\mu\nu}\partial_\mu\phi\partial_\nu\phi - V(\phi)\right] \tag{A.47}$$

The energy-momentum tensor of the scalar field is[1]

$$T_{\mu\nu} \equiv -\frac{2}{\sqrt{-g}}\frac{\delta S_\phi}{\delta g^{\mu\nu}} = \partial_\mu\phi\partial_\nu\phi - g_{\mu\nu}\left(\frac{1}{2}\partial^\sigma\phi\partial_\sigma\phi + V(\phi)\right) \tag{A.48}$$

Even if the universe is not flat, it will get very close to being flat after a few e-folds during inflation, as we saw above, so for simplicity we will assume that the universe is flat from now on. Using the FRW metric (A.1) in Cartesian coordinates, and assuming homogeneous field $\phi(t, \vec{x}) = \phi(t)$, the energy-momentum tensor takes the form (A.4) with

$$\rho_\phi = \frac{1}{2}\dot{\phi}^2 + V(\phi) \tag{A.49}$$

$$p_\phi = \frac{1}{2}\dot{\phi}^2 - V(\phi) \tag{A.50}$$

so the condition $p = -\rho$ for exponential expansion can be approximately satisfied if the kinetic term $\dot{\phi}^2/2$ is much smaller than the potential term $V(\phi)$.

The Friedmann equation (A.6) takes the form:

$$H^2 = \frac{1}{3M_{pl}^2}\left(\frac{1}{2}\dot{\phi}^2 + V(\phi)\right) \tag{A.51}$$

And the continuity equation (A.7) becomes (after dividing by $\dot{\phi}$):

$$\ddot{\phi} + 3H\dot{\phi} + V_{,\phi} = 0 \tag{A.52}$$

Taking the time derivative of (A.52) and using (A.51) we get

$$\dot{H} = -\frac{\dot{\phi}^2}{2M_{pl}^2} \tag{A.53}$$

and the slow-roll parameter (A.45) takes the form

$$\epsilon = \frac{1}{2M_{pl}^2}\frac{\dot{\phi}^2}{H^2} \tag{A.54}$$

Using (A.49), (A.50), and (A.51) the acceleration equation (A.8) can be written as

$$\frac{\ddot{a}}{a} = H^2(1 - \epsilon) \tag{A.55}$$

Once again, we see that inflation ends as soon as ϵ becomes 1.

[1] $\delta g = -g g_{\mu\nu}\delta g^{\mu\nu}$

The second slow-roll parameter (A.46) takes the form

$$\eta = -\frac{\ddot{\phi}}{H\dot{\phi}} \tag{A.56}$$

As we noted earlier, inflation will last long enough to solve the problems of standard cosmology if $\epsilon \ll 1$ and $\eta \ll 1$, which implies

$$\dot{\phi}^2 \ll V(\phi) \tag{A.57}$$

$$|\ddot{\phi}| \ll |3H\dot{\phi}|,\ |V_{,\phi}| \tag{A.58}$$

We can also introduce the **potential slow-roll parameters** which depend only on the shape of the potential $V(\phi)$

$$\epsilon_v \equiv \frac{M_{pl}^2}{2}\left(\frac{V_{,\phi}}{V}\right)^2 \tag{A.59}$$

$$\eta_v \equiv M_{pl}^2 \frac{V_{,\phi\phi}}{V} \tag{A.60}$$

It is not hard to show that in slow-roll regime the two sets of parameters are related as follows

$$\epsilon \simeq \epsilon_v, \quad \eta \simeq \eta_v - \epsilon_v \tag{A.61}$$

and

$$H^2 \simeq \frac{V(\phi)}{3M_{pl}^2} \simeq const \tag{A.62}$$

$$\dot{\phi} \simeq -\frac{V_{,\phi}}{3H} \tag{A.63}$$

implying

$$a(t) \propto e^{Ht} \tag{A.64}$$

Finally, we can calculate the total number of e-folds $N(\phi)$ starting with some value of the field ϕ until the end ϕ_{end}

$$N(\phi) = \int_t^{t_{end}} H\,\mathrm{d}t = \int_\phi^{\phi_{end}} \frac{H}{\dot{\phi}}\mathrm{d}\phi$$

which, using (A.62) and (A.63), takes the form

$$N(\phi) \simeq \frac{1}{M_{pl}^2}\int_{\phi_{end}}^{\phi} \frac{V}{V_{,\phi}}\mathrm{d}\phi$$

$$N(\phi) \simeq \frac{1}{M_{pl}}\int_{\phi_{end}}^{\phi} \frac{\mathrm{d}\phi}{\sqrt{2\epsilon_v}} \simeq \frac{1}{M_{pl}}\int_{\phi_{end}}^{\phi} \frac{\mathrm{d}\phi}{\sqrt{2\epsilon}} \tag{A.65}$$

Appendix B

CMB Lensing

As the CMB photons travel through the universe after recombination without scattering off charged particles, they are affected only by gravity, under which they get redshifted but also deflected. Lensing refers to the deflection of photons. In a homogeneous universe there is no lensing, lensing results only from anisotropies. Since only large scales contribute to lensing significantly, and these large scales have stayed in the linear regime up to now, we calculate the deflection angle only up to first order in anisotropies. CMB lensing is discussed in some standard textbooks, such as [36], as well as in [47, 48, 49]. In this appendix we will briefly summarize the main results.

The scalar metric can be written in the Newtonian gauge in the form (vector and tensor modes do not contribute to lensing)

$$ds^2 = -(1+2\Psi)dt^2 + a^2(t)(1+2\Phi)\delta_{ij}dx^i dx^j \tag{B.1}$$

There is no anisotropic stress in the late universe (after recombination), which implies

$$\Phi = -\Psi \tag{B.2}$$

The geodesic equation for photons from this metric takes the form

$$\frac{d^2}{d\chi^2}(\chi\theta^i) = -2\Psi_{,i} \tag{B.3}$$

where χ is the conformal distance to the photon, θ is the direction.

Integrating, we get

$$\frac{d}{d\chi}(\chi\theta^i)\Big|_0^\chi = -2\int_0^\chi d\chi' \Psi_{,i}(x(\chi'))$$

$$\frac{d}{d\chi}(\chi\theta^i) = -2\int_0^\chi d\chi' \Psi_{,i}(x(\chi')) + \theta^i(0)$$

$$\chi\theta^i\big|_0^\chi = -2\int_0^\chi d\chi'' \int_0^{\chi''} d\chi' \Psi_{,i}(x(\chi')) + \chi\theta^i(0)$$

$$\theta^i(\chi) = -\frac{2}{\chi}\int_0^\chi d\chi'' \int_0^{\chi''} d\chi' \Psi_{,i}(x(\chi')) + \theta^i(0)$$

Changing the order of integration, we get

$$\theta^i(\chi) = \theta^i(0) - \frac{2}{\chi}\int_0^\chi d\chi' \Psi_{,i}(x(\chi'))(\chi - \chi')$$

Let χ^* be the conformal distance to the last scattering surface. Then $\theta(\chi^*) \equiv \tilde{\theta}$ is the original (unlensed) angle, $\theta(0) \equiv \theta$ is the observed angle:

$$\tilde{\theta}^i = \theta^i - \frac{2}{\chi^*}\int_0^{\chi^*} d\chi \Psi_{,i}(x(\chi))(\chi^* - \chi)$$

Since $x^i = \chi\theta^i$

$$\Psi_{,i} = \frac{1}{\chi}\frac{d}{d\theta^i}\Psi$$

We denote

$$\phi(\hat{n}) \equiv -2\int_0^{\chi^*} d\chi \Psi(\chi\hat{n}, \eta_0 - \chi)\frac{\chi^* - \chi}{\chi^*\chi} \tag{B.4}$$

and call the **lensing potential**, where η_0 is the current conformal time. Denoting the lensed and unlensed temperature anisotropies (or any other scalar function) by Θ and $\tilde{\Theta}$ respectively, we can write

$$\Theta(\theta) = \tilde{\Theta}(\tilde{\theta})$$

which gives

$$\Theta(\hat{n}) = \tilde{\Theta}(\hat{n} + \nabla\phi(\hat{n})) \tag{B.5}$$

where ∇ is the covariant derivative on the sphere. To first order

$$\Theta(\hat{n}) = \tilde{\Theta}(\hat{n}) + \nabla_i \phi(\hat{n}) \nabla^i \tilde{\Theta}(\hat{n})$$

In harmonic space this takes the form

$$\delta\Theta_{lm} = \sum_{LM} \sum_{l'm'} \phi_{LM} \tilde{\Theta}_{l'm'} I_{l\ L\ l'}^{m M m'} \tag{B.6}$$

where

$$I_{l\ L\ l'}^{m M m'} = \int d\hat{n} Y_{lm}^* \nabla_i Y_{LM} \nabla^i Y_{l'm'} \tag{B.7}$$

$$I_{l\ L\ l'}^{m M m'} = (-1)^m \begin{pmatrix} l & L & l' \\ -m & M & m' \end{pmatrix} {}_0F_{lLl'} \tag{B.8}$$

$${}_sF_{lLl'} = [L(L+1) + l'(l'+1) - l(l+1)] \sqrt{\frac{(2L+1)(2l+1)(2l'+1)}{16\pi}} \begin{pmatrix} l & L & l' \\ s & 0 & -s \end{pmatrix} \tag{B.9}$$

Let us now obtain the relationship between the lensing potential and primordial perturbations. Since we consider only linear order, the calculation is done in Fourier space

$$\Psi(\vec{x}, \eta) = \int \frac{d^3k}{(2\pi)^3} \Psi(\vec{k}, \eta) e^{i\vec{k}\cdot\vec{x}}$$

The gravitational potential is related to primordial curvature perturbation by the transfer function

$$\Psi(\vec{k}, \eta) = T_\Psi(k, \eta) \mathscr{R}(\vec{k}) \tag{B.10}$$

Note that the transfer function does not depend on the direction of $\vec{k}$. The lensing potential takes the form

$$\phi(\hat{n}) = \int \frac{d^3k}{(2\pi)^3} \mathscr{R}(\vec{k}) \int_0^{\chi^*} d\chi (-2) \frac{\chi^* - \chi}{\chi^* \chi} e^{i(\vec{k}\cdot\hat{n})\chi} T_\Psi(k, \eta_0 - \chi)$$

Denoting[1]

$$R_\Psi(k, \hat{k}\cdot\hat{n}) \equiv \int_0^{\chi^*} d\chi (-2) \frac{\chi^* - \chi}{\chi^* \chi} e^{ik\chi(\hat{k}\cdot\hat{n})\chi} T_\Psi(k, \eta_0 - \chi) \tag{B.11}$$

[1] T_Ψ, as well as R_Ψ can be calculated numerically, for example using the publicly available code CAMB.

we get

$$\phi(\hat{n}) = \int \frac{d^3k}{(2\pi)^3}\mathscr{R}(\vec{k})R_\Psi(k, \hat{k}\cdot\hat{n}) \tag{B.12}$$

In harmonic space

$$\phi_{lm} = \int d\Omega Y^*_{lm}(\hat{n})\phi(\hat{n})$$

$$\phi_{lm} = \int \frac{d^3k}{(2\pi)^3}\mathscr{R}(\vec{k}) \int d\Omega Y^*_{lm}(\hat{n})R_\Psi(k, \hat{k}\cdot\hat{n})$$

Decomposing R_Ψ into Legendre polynomials

$$R_\Psi(k, \hat{k}\cdot\hat{n}) = \sum_l (-i)^l(2l+1)P_l(\hat{k}\cdot\hat{n})R^l_\Psi(k)$$

we get

$$\int d\Omega Y^*_{lm}(\hat{n})R_\Psi(k, \hat{k}\cdot\hat{n}) = 4\pi(-i)^l Y^*_{lm}(\hat{k})R^l_\Psi(k)$$

$$\phi_{lm} = 4\pi(-i)^l \int \frac{d^3k}{(2\pi)^3}\mathscr{R}(\vec{k})Y^*_{lm}(\hat{k})R^l_\Psi(k) \tag{B.13}$$

Assuming the standard correlation

$$\left\langle \mathscr{R}(\vec{k})\mathscr{R}^*(\vec{k'}) \right\rangle = (2\pi)^3 P_{\mathscr{R}}(k)\delta^3(\vec{k} - \vec{k'}) \tag{B.14}$$

with

$$P_{\mathscr{R}}(k) \equiv \frac{2\pi^2}{k^3}\Delta^2_{\mathscr{R}}(k) \tag{B.15}$$

where $\Delta^2_{\mathscr{R}}(k)$ is the unitless power spectrum, the correlation between ϕ_{lm}'s takes the form

$$\langle \phi_{lm}\phi^*_{l'm'} \rangle = \delta_{ll'}\delta_{mm'}C^\phi_l \tag{B.16}$$

$$C^\phi_l = 4\pi \int \frac{dk}{k}\Delta^2_{\mathscr{R}}(k)|R^l_\Psi(k)|^2 \tag{B.17}$$

R^l_Ψ can be calculated in terms of spherical Bessel functions

$$R^l_\Psi(k) = 2(-1)^l \int_o^{\chi^*} d\chi \frac{\chi^* - \chi}{\chi^*\chi} j_l(k\chi)T_\Psi(k, \eta_0 - \chi) \tag{B.18}$$

Bibliography

[1] D. Baumann, *TASI Lectures on Inflation*, arXiv:0907.5424.

[2] J. D. Barrow and H. Kodama, *All Universes Great and Small*, *Int. J. Mod. Phys.* **D10** (2001) 785–790, [gr-qc/0105049].

[3] A. D. Linde, *Creation of a compact topologically nontrivial inflationary universe*, *JCAP* **0410** (2004) 004, [hep-th/0408164].

[4] B. F. Roukema and V. Blanloeil, *A measure on the set of compact Friedmann-Lemaitre- Robertson-Walker models*, *Class. Quant. Grav.* **27** (2010) 245001, [arXiv:0912.2300].

[5] B. F. Roukema, *Which FLRW comoving 3-manifold is preferred observationally and theoretically?*, arXiv:1002.3528.

[6] J. P. Luminet, J. Weeks, A. Riazuelo, R. Lehoucq, and J. P. Uzan, *Dodecahedral space topology as an explanation for weak wide-angle temperature correlations in the cosmic microwave background*, *Nature.* **425** (2003) 593, [astro-ph/0310253].

[7] S. Caillerie *et. al.*, *A new analysis of Poincaré dodecahedral space model*, *Astron. Astrophys.* **476** (2007), no. 2 691–696, [arXiv:0705.0217].

[8] B. S. Lew and B. F. Roukema, *A test of the Poincare dodecahedral space topology hypothesis with the WMAP CMB data*, *Astron. Astrophys.* **482** (2008), no. 3 747–753, [arXiv:0801.1358].

[9] R. Aurich, S. Lustig, and F. Steiner, *CMB Anisotropy of the Poincare Dodecahedron*, *Class. Quant. Grav.* **22** (2005) 2061–2083, [astro-ph/0412569].

[10] J. Weeks, J.-P. Luminet, A. Riazuelo, and R. Lehoucq, *Well-proportioned universes suppress CMB quadrupole*, *Mon. Not. Roy. Astron. Soc.* **352** (2004) 258, [astro-ph/0312312].

[11] N. J. Cornish, D. N. Spergel, and G. D. Starkman, *Circles in the Sky: Finding Topology with the Microwave Background Radiation*, *Class. Quant. Grav.* **15** (1998) 2657–2670, [astro-ph/9801212].

[12] B. Mota, M. J. Reboucas, and R. Tavakol, *Circles-in-the-sky searches and observable cosmic topology in a flat Universe*, *Phys. Rev.* **D81** (2010) 103516, [arXiv:1002.0834].

[13] J. Levin, *Lorentz-boosted circles-in-the-sky and cosmic topology*, *Phys. Rev. D* **70** (Oct, 2004) 083001.

[14] N. J. Cornish, D. N. Spergel, G. D. Starkman, and E. Komatsu, *Constraining the Topology of the Universe*, *Phys. Rev. Lett.* **92** (2004) 201302, [astro-ph/0310233].

[15] J. Shapiro Key, N. J. Cornish, D. N. Spergel, and G. D. Starkman, *Extending the WMAP Bound on the Size of the Universe*, *Phys. Rev.* **D75** (2007) 084034, [astro-ph/0604616].

[16] P. Bielewicz and A. J. Banday, *Constraints on the topology of the Universe derived from the 7-yr WMAP data*, *MNRAS* **412** (2011) 2104, [arXiv:1012.3549].

[17] N. G. Phillips and A. Kogut, *Constraints On The Topology Of The Universe From The WMAP First-Year Sky Maps*, *Astrophys. J.* **645** (2006) 820–825, [astro-ph/0404400].

[18] A. de Oliviera Costa and G. F. Smoot, *Constraints on the topology of the universe from the 2- year COBE data*, *Astrophys. J.* **448** (1995) 477, [astro-ph/9412003].

[19] A. de Oliveira-Costa, G. F. Smoot, and A. A. Starobinsky, *Can the lack of symmetry in the COBE/DMR maps constrain the topology of the universe?*, *Astrophys. J.* **468** (1996) 457, [astro-ph/9510109].

[20] M. Kunz *et. al.*, *Constraining topology in harmonic space*, *Phys. Rev.* **D73** (2006) 023511, [astro-ph/0510164].

[21] R. Aurich, H. S. Janzer, S. Lustig, and F. Steiner, *Do we Live in a 'Small Universe'?*, *Class. Quant. Grav.* **25** (2008) 125006, [arXiv:0708.1420].

[22] R. Aurich and S. Lustig, *Cosmic microwave anisotropies in an inhomogeneous compact flat universe*, arXiv:1009.5880.

[23] A. A. Starobinsky, *New restrictions on spatial topology of the universe from microwave background temperature fluctuations*, *JETP Lett.* **57** (1993) 622–625, [gr-qc/9305019].

[24] I. Y. Sokolov, *Topologically nontrivial nature of the universe in connection with the anisotropy of the background radiation*, *JETP Lett.* **57** (1993) 617–621.

[25] D. Stevens, D. Scott, and J. Silk, *Microwave background anisotropy in a toroidal universe*, *Phys. Rev. Lett.* **71** (1993) 20–23.

[26] **Planck** Collaboration, Planck Collaboration, *Planck: The scientific programme*, astro-ph/0604069.

[27] A. Lewis, A. Challinor, and A. Lasenby, *Efficient computation of CMB anisotropies in closed FRW models*, *Astrophys. J.* **538** (2000) 473–476, [astro-ph/9911177].

[28] N. Jarosik *et. al.*, *Seven-Year Wilkinson Microwave Anisotropy Probe (WMAP) Observations: Sky Maps, Systematic Errors, and Basic Results*, *Astrophys. J. Suppl.* **192** (2011) 14, [arXiv:1001.4744].

[29] D. Larson *et. al.*, *Seven-Year Wilkinson Microwave Anisotropy Probe (WMAP) Observations: Power Spectra and WMAP-Derived Parameters*, *Astrophys. J. Suppl.* **192** (2011) 16, [arXiv:1001.4635].

[30] E. Komatsu *et. al.*, *Seven-Year Wilkinson Microwave Anisotropy Probe (WMAP) Observations: Cosmological Interpretation*, *Astrophys. J. Suppl.* **192** (2011) 18, [arXiv:1001.4538].

[31] K. Land and J. Magueijo, *The axis of evil*, *Phys. Rev. Lett.* **95** (2005) 071301, [astro-ph/0502237].

[32] K. Land and J. Magueijo, *The Axis of Evil revisited*, *Mon. Not. Roy. Astron. Soc.* **378** (2007) 153–158, [astro-ph/0611518].

[33] A. Rakic and D. J. Schwarz, *Correlating anomalies of the microwave sky: The Good, the Evil and the Axis*, *Phys. Rev.* **D75** (2007) 103002, [astro-ph/0703266].

[34] J. G. Cresswell, A. R. Liddle, P. Mukherjee, and A. Riazuelo, *Cosmic microwave background multipole alignments in slab topologies*, *Phys. Rev.* **D73** (2006) 041302, [astro-ph/0512017].

[35] R. L. Arnowitt, S. Deser, and C. W. Misner, *Republication of: The dynamics of general relativity*, *General Relativity and Gravitation* **40** (2008) 1997–2027, [gr-qc/0405109].

[36] S. Dodelson, *Modern Cosmology*. Academic Press, 2003.

[37] U. Seljak and M. Zaldarriaga, *A line of sight approach to cosmic microwave background anisotropies*, *Astrophys. J.* **469** (1996) 437–444, [astro-ph/9603033].

[38] K. Gorski, E. Hivon, A. Banday, B. Wandelt, F. Hansen, *et. al.*, *HEALPix - A Framework for high resolution discretization, and fast analysis of data distributed on the sphere*, *Astrophys.J.* **622** (2005) 759–771, [astro-ph/0409513].

[39] **Particle Data Group** Collaboration, K. Nakamura *et. al.*, *Review of particle physics*, *J.Phys.G* **G37** (2010) 075021.

[40] W. Cash, *Parameter estimation in astronomy through application of the likelihood ratio*, *Astrophys. J.* **228** (1979) 939–947.

[41] W. Eadie, D. Drijard, F. James, M. Roos, and B. Sadoulet, *Statistical Methods in Experimental Physics*. North Holland, Amsterdam, 1971.

[42] C. H. Lineweaver, *The CMB Dipole: The Most Recent Measurement And Some History*, astro-ph/9609034.

[43] C. Gordon, *Broken Isotropy from a Linear Modulation of the Primordial Perturbations*, *Astrophys.J.* **656** (2007) 636–640, [astro-ph/0607423].

[44] U. H. Danielsson, *A note on inflation and transplanckian physics*, *Phys. Rev.* **D66** (2002) 023511, [hep-th/0203198].

[45] R. Easther, W. H. Kinney, and H. Peiris, *Boundary effective field theory and trans-Planckian perturbations: Astrophysical implications*, *JCAP* **0508** (2005) 001, [astro-ph/0505426].

[46] A. D. Linde and V. F. Mukhanov, *Nongaussian isocurvature perturbations from inflation*, *Phys.Rev.* **D56** (1997) 535–539, [astro-ph/9610219].

[47] A. Challinor and A. Lewis, *Lensed CMB power spectra from all-sky correlation functions*, *Phys.Rev.* **D71** (2005) 103010, [astro-ph/0502425]. 16 pages, 4 figures. Changes to match PRD version including new section on non-linear corrections. CAMB code available at http://camb.info/.

[48] U. Seljak, *Gravitational lensing effect on cosmic microwave background anisotropies: A Power spectrum approach*, *Astrophys.J.* **463** (1996) 1, [astro-ph/9505109].

[49] T. Okamoto and W. Hu, *CMB lensing reconstruction on the full sky*, *Phys.Rev.* **D67** (2003) 083002, [astro-ph/0301031].

[50] E. W. Kolb and M. S. Turner, *The Early Universe*. Westview Press, 1994.

[51] S. Weinberg, *Cosmology*. Oxford University Press, USA, 2008.

[52] C. W. Misner, K. S. Thorne, and J. A. Wheeler, *Gravitation*. W.H. Freeman and Company, New York, 1973.